Numerical simulation of fatigue crack propagation in real polycrystals imaged by X ray tomography

Jia Li

▶ **To cite this version:**

HAL Id: tel-01321257
https://pastel.hal.science/tel-01321257

Submitted on 25 May 2016

École doctorale n° 432 : Sciences des Métiers de l'Ingénieur

Doctorat ParisTech

T H È S E

pour obtenir le grade de docteur délivré par

l'École nationale supérieure des mines de Paris

Spécialité Sciences et génie des matériaux

Présentée et soutenue publiquement par

Jia LI

le 15 décembre 2015

Simulation par éléments finis de la propagation de fissures de fatigue dans les matériaux polycristallins imagés par tomographie aux rayons X

Numerical simulation of fatigue crack propagation in real polycrystals imaged by X ray tomography

Directeurs de thèse : **Samuel FOREST et Henry PROUDHON**
Co-encadrement de la thèse : **Arjen ROOS**

Jury

M. Jean-Yves BUFFIÈRE, Professeur, INSA de Lyon	Président
M. Ulrich KRUPP, Professeur, Osnabrück University of Applied Sciences	Rapporteur
M. Julien RÉTHORÉ, Chargé de Recherche CNRS, INSA de Lyon	Rapporteur
M. Nicolas SAINTIER, Professeur, Arts et Métiers ParisTech	Examinateur
M. Wolfgang LUDWIG, Directeur de Recherche CNRS, INSA de Lyon	Examinateur
M. Henry PROUDHON, Chargé de Recherche CNRS, Mines ParisTech	Examinateur
M. Samuel FOREST, Directeur de Recherche CNRS, Mines ParisTech	Examinateur
M. Arjen ROOS, Ingénieur – chercheur, HDR, Safran CRT	Examinateur

T
H
È
S
E

MINES ParisTech
Centre des matériaux
CNRS UMR 7633
10 rue Henry DESBRUERES, BP87, F-91003 Evry cedex, FRANCE

Acknowledgements

I have many fond memories of my three years during which I did the present research work for my PhD at Centre des Matériaux and I shall cherish for the rest of my life. For these, I would like to thank my people.

First and foremost, I would like to express my sincere gratitude to my supervisors: Prof. Samuel Forest, Dr. Henry Proudhon and Dr. Arjen Roos for their support, guidance and constant encouragement during the course of this research. It has been a great pleasure to work with them.

I would like to thank the members of my PhD defence committee for the acceptance of the positions of reviewers and examiners of my dissertation. I would like to offer special thanks to Prof. Ulrich Krupp and Dr. Julien Réthoré for being my reviewers. Their efforts in reviewing the manuscript have allowed me to improve the contents of my thesis.

I would like to acknowledge the financial support of the French National Research Agency (ANR) within project CRYSTAL. I am thankful to the project members : Vincent Chiaruttini, Wolfgant Ludwig and Jen-Yves Buffière for their excellent scientific collaboration.

I am grateful to Djamel and Nicolay from the VAL team who helped me enormously in implementing the developed model in Zebulon.

I would like to thand my office colleagues Victor, David, Nicolas, Erembert and Arina who have made a pleasant working environment and for the all the discussions during the three years.

Finally, I would like to express my gratitude to my parents for their constant support and endless love. Without their support, I would never have pursued a PhD.

Houilles, 07 february 2016

Abstract

In order to understand the mechanisms of short fatigue crack propagation, an in-situ characterisation by X-ray tomography was carried out at ESRF, using two techniques of tomography. Diffraction Contrast Tomography (DCT) that is a non-destructive method can be used to obtain 3D morphology and grain orientations in an undeformed state of polycrystal materials. Couple with Phase Contrast Tomography (PCT), it allows to characterise the short fatigue crack propagation at different loading stages. Access to this information, it is possible to simulate the short fatigue crack propagation using a 3D reel microstructural mesh reconstructed from the tomographic images.

In this work, the elastic anisotropic behaviour in a 3D microstructural mesh is performed. The elastic strain tensors averaged in grains are also compared to the experimental measurements. Then, a new numerical approach is proposed to simulate crack propagation. From a crystal plasticity FE simulation, the crack growth direction is determined by a post processing. Next, the crack is propagated through remeshing to a selected distance. This approach is firstly applied to the single crystals and bi-crystals. The crack growth rate is also analysed. Finally, this approach is applied to the polycrystal mesh reconstructed from the tomographic images. By comparing between simulation and experimental crack, the damage indicator is discussed at the end.

Ce n'est pas parce que les choses sont difficiles que nous n'osons pas, c'est parce que nous n'osons pas qu'elles sont difficiles.

Sénèque

Contents

Notations

D	damage variable	
d	inter-lattice spacing	m
G	energy release rate	J/m^2
h	degradation factor	
I_0	intensity of incident radiation	KeV
I_x	intensity of transmitted radiation	KeV
l	minimum element size	mm
n	integer	
x	sample thickness	m
R_0	crack growth distance	mm
U	displacement	mm
λ	incident wavelength	m
θ	diffraction angle	degree
μ	attenuation coefficient	cm^2/g
γ_{pl}	plastic slip amplitude	
τ_R^s	resolved shear stress	MPa
β	tilt angle	degree
α	twist angle	degree

Introduction

In industrial applications, the components in service are subjected to repeated loading and unloading. This application of cyclic stress or strain lead to local accumulation of micro plastic events depending on the material properties. This may further provoke crack initiation and ultimately can lead to component failure. Ever since the serious rail transportation accidents occurred in the 19th century, fatigue of materials has been investigated intensively to achieve life prediction of industrial components. It has been found that in many cases the major part of the lifetime is spent on nucleation and growth of small fatigue cracks.

A small fatigue crack has a typical length that is of the same order as one of the characteristic length scales of the microstructure, such as the grain size. The details of the microstructure around the small fatigue crack front, such as misorientation between adjacent grains and grain boundaries, strongly influence its propagation behaviour. Therefore, the prediction of small fatigue crack growth paths in 3D and the rate of crack propagation remains a real challenge.

In order to understand the physical mechanisms by observation and simulation of short crack propagation in a Ti-alloy, a French National Research Agency (ANR) project CRYSTAL was carried out at *Mines ParisTech*, *INSA Lyon* and *ONERA*. The project is composed of two parts: the X-ray tomographic characterisation conducted mainly by *INSA Lyon* and the numerical simulation in collaboration with *Mines ParisTech* and *ONERA*. This PhD work is integrated in the simulation part of the project CRYSTAL.

The in-situ experiments were carried out at the European Synchrotron Radiation Facility (ESRF) to characterise the 3D microstructural features of the polycrystalline materials and the effects of grain boundaries on short crack growth. The Diffraction Contrast Tomography (DCT) provides the 3D morphology and microstructure of a polycrystalline sample with up to 1000 grains in its undeformed

state. Combined with Phase Contrast Tomography (PCT) and interrupted in-situ fatigue experiments, the 3D geometry of short cracks can be determined at different stages [Ludwig *et al.*, 2010], see Figure 1 (a). With access to this information, the simulation of the growth of small fatigue cracks using the real polycrystalline microstructures by the Crystal Plasticity Finite Element (CPFE) method now becomes possible.

Since the first implementation by [Asaro, 1983], CPFE has been widely developed to simulate the anisotropic behaviour and the crystal orientation dependency in polycrystalline materials. Coupled with realistic polycrystalline grain meshes, CPFE can be used to investigate the physical origins of plasticity and damage of materials. Recently, CPFE simulations have been carried out [Ludwig *et al.*, 2009, Proudhon *et al.*, 2015] using a 3D realistic microstructural mesh reconstructed from tomographic images, as shown in Figure 1 (b). With these simulations the effects of microstructure on local behaviour in grains can be studied and compared with the experimental strain measurements. However, the simulation of 3D short fatigue crack growth using the realistic mesh is still impossible.

Objectives

The aim of this work is to develop a numerical approach to simulate short fatigue crack propagation using the 3D realistic microstructural mesh reconstructed from X-ray tomography. For this, two in-situ experiments are carried out at the ESRF.

The first test is dedicated to validate the mesh reconstruction process and the experimental measurement of the elastic strain tensors. A compression test of a pure titanium sample is simulated using the realistic FE mesh with the measured grain orientations. For each grain, the average elastic strain tensors are compared.

The second experiment is performed with a pre-notched sample of VST55531 titanium alloy to investigate fatigue crack propagation. A computational approach is developed in order to simulate the complex shapes and the rate of small fatigue crack propagation. A phenomenological crystal plasticity model is selected [Méric *et al.*, 1991]. This model can reproduce both the global mechanical behaviour of the material and the local crack tip strain fields in elastic-ideally plastic crystals as analysed by [Rice, 1987]. The material parameters are determined by a series of tensile and tension-compression experiments. The methodology is tested

(a)

(b)
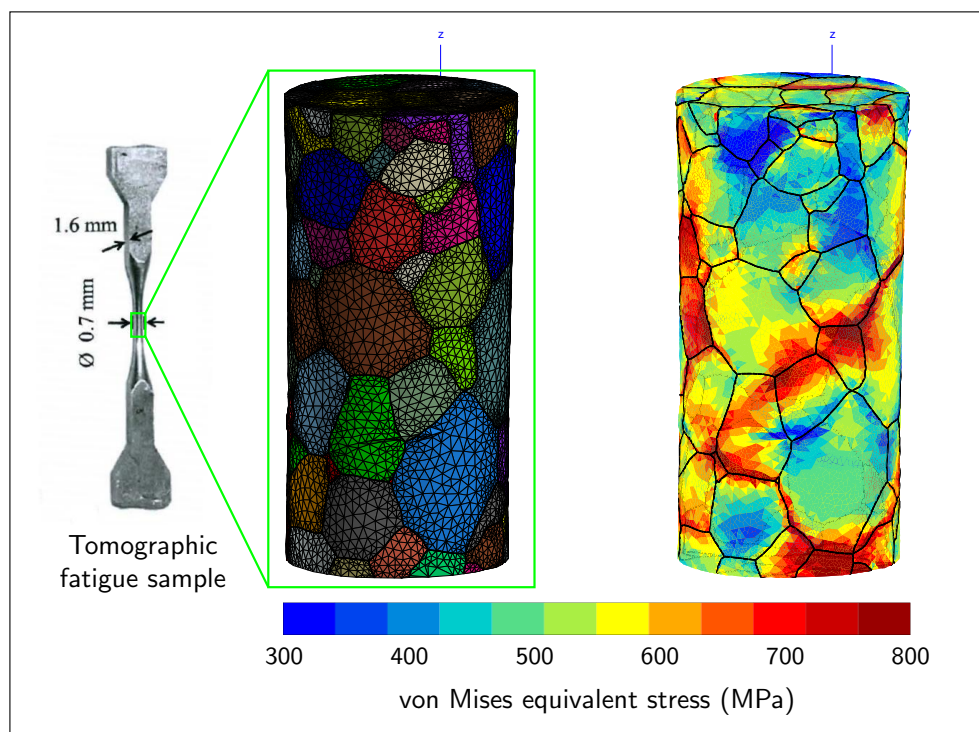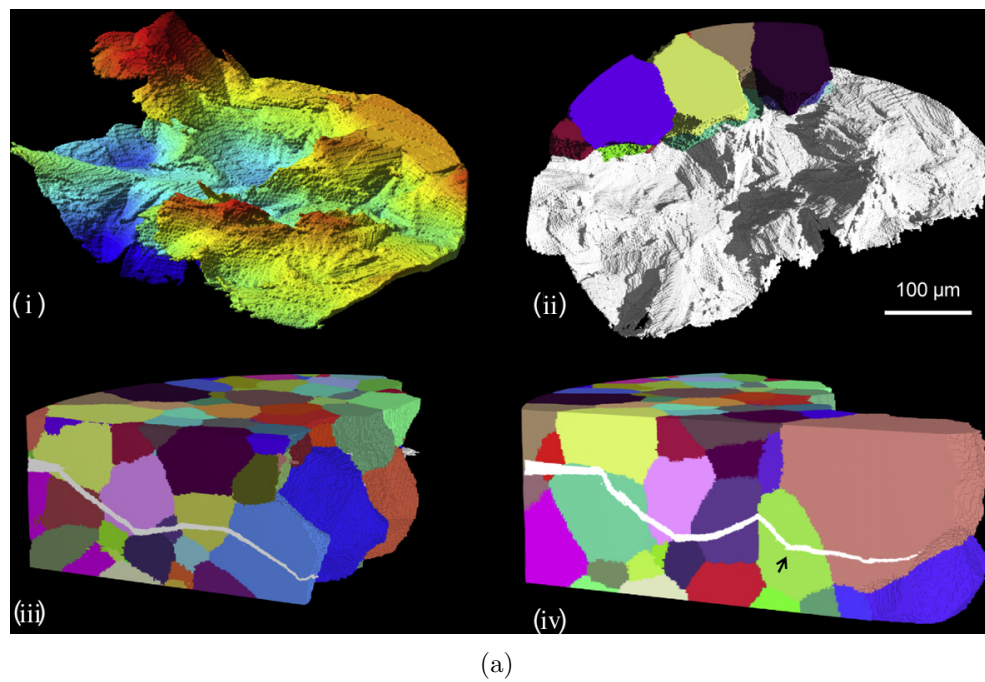
FIGURE 1: (a) 3D short fatigue crack after 75.5k cycles in Beta21S [Herbig *et al.*, 2011]. (b) Von Mises stress obtained by the CPFE simulation using a FE mesh reconstructed from tomographic images [Ludwig *et al.*, 2009].

in several single crystals and bicristals before being applied to the polycrystalline case. Finally, the crack path and the proagation rate are compared between the simulation and the experimental fatigue crack.

Outline

In chapter 1, a literature review surveys the characterisation techniques at the grain scale. Then, an investigation of fatigue crack growth models and numerical approaches for crack propagation simulation is given. Chapter 2 is devoted to the numerical tools developed for this work. Microstructural mesh reconstruction from tomographic images, the crack propagation remeshing method, the parallel computation and the integration fields transfer technique are summarised. The elastic behaviour of pure titanium is studied in chapter 3. The crack propagation methodology in single crystals is presented in chapter 4. This method is applied to bicrystals and polycrystals in chapter 5. Finally, conclusions and outlook about future work are given in chapter 6.

Introduction

Les composants industriels subissent des chargements cycliques qui sont à l'origine de l'apparition et de la propagation de fissures. Depuis les accidents ferroviaires du 19ème siècle, la résistance en fatigue des matériaux a été beaucoup étudiée afin de pouvoir prédire la durée de vie de pièces. Il s'avère que, dans de nombreux de cas, la période d'amorçage et de propagation de fissures courtes peut représenter en grande partie de la durée de vie totale d'une pièce.

Les fissures courtes ont une taille comparable à la dimension caractéristique de la microstructure, généralement la taille de grain dans un polycristal. La propagation de ces fissures courtes est fortement influencée par l'hétérogénéité de la microstructure autour du front de fissure tels que désorientation des grains adjacents et joint des grains. Par conséquent, la prédiction du chemin et la vitesse de propagation de fissure courte est un défi particulièrement important.

Afin de comprendre les mécanismes physiques de propagation de fissure courte dans un alliage titane par les biais d'expérience et de simulation, un projet CRYSTAL financé par l'Agence National de la Recherche (ANR) s'est établi entre *Mines ParisTech*, *INSA Lyon* et *ONERA*. Le projet comprend deux partie: la caractérisation par tomographie aux rayons X est menée principalement par *INSA Lyon*, la simulation numérique est réalisée en collaboration par *Mines ParisTech* et *ONERA*. Ces travaux de thèse sont intégrés à la partie simulation numérique du projet CRYSTAL.

Les essais in-situ sont réalisés à l'ESRF (European Synchrotron Radiation Facility) pour caractériser en 3D les microstructures et la propagation de fissure courte dans un matériau polycristallin. La Tomographie par Contrast de Diffraction (DCT) permet d'obtenir en 3D la morphologie et la microstructure d'un polycristal ayant jusqu'à 1000 grains dans un état non déformé. Avec la Tomographie par Contrast de Phase (PCT) et les essais in-situ de fatigue interrompus, les fissures à

5

différents états de chargement peuvent être reconstuites [Ludwig *et al.*, 2010], voir Figure 1 (a). L'accès à ces information permettrait de simuler la propagation de fissures courtes par l'Eléments Finis en Plasticité Cristalline (CPFE) en utilisant une microstructure réel d'un polycristal.

CPFE a été largement développé depuis sa première implémentation par [Asaro, 1983] pour simuler le comportement anisotrope à l'échelle de grain dans un matériau polycristallin. A l'aide d'un maillage réaliste avec des grains, il est désormais possible d'étudier l'origine physique de plasticité et d'endommagement par la simulation CPFE. Récemment, les calculs CPFE ont été effectués dans [Ludwig *et al.*, 2009, Proudhon *et al.*, 2015] en utilisant un maillage 3D réel reconstruit par des images tomographiques, voir Figure 1 (b). Ce nouveau type de calcul permet d'étudier l'effet microstructural sur le comportement local dans un grain et de comparer avec des mesures expérimentales. Toutefois, la simulation de la propagation de fissure courte en 3D en utilisant le maillage réel polycristallin restait toujours impossible.

Objectif

L'objectif de la thèse est de développer une méthode numérique pour simuler la propagation de fissure courte dans un maillage 3D microstructural réel reconstruit par les images de tomographie aux rayons X. Pour cela, deux expériences in-situ ont été effectués à l'ESRF.

Le premier essai consiste à valider la méthode de reconstruction de maillage et de mesure expérimentale des tenseurs de déformation élastique. Il s'agit d'une compression sur une éprouvette en titane pur. En utilisant le maillage réel reconstruit par les images tomographiques et l'orientation de grains mesurée, la simulation CPFE de cette compression prédit les tenseurs de déformation élastique. Les valeurs moyennées en charque grain sont comparées avec les tenseurs mesurés expérimentalement.

La seconde expérience est effectuée avec une éprouvette pré-fissurée de l'alliage titane VST55531 pour étudier la propagation de fissure courte. Afin de simuler la complexe forme 3D et la vitesse de propagation de cette fissure, une approche numérique est proposée dans ce travail. Un modèle phénoménologique de plasticité cristalline a été sélectionné [Méric *et al.*, 1991], qui est capable de reproduire à la

fois le comportement mécanique global et le champs local de glissement au front fissure dans les cristaux élastique parfaitement plastique [Rice, 1987]. Les paramètres de matériau sont identifiés par les essais de traction et traction-compression. Cette méthode de simulation est appliquée aux monocristaux et bicristaux anisi que le polycristal. Enfin, le chemin et la vitesse de propagation de fissure sont comparés entre la simulation et l'expérience.

Plan

Chapitre 1 présente une revue de la littérature sur les techniques de caractérisation à l'échelle de grain et les modèles de propagation de fissure courte. Chapitre 2 est dédié aux outils numériques développés dans le cadre de la thèse. La reconstruction de maillage microstructural à partir des images tomographiques, la méthode de remaillage pour la propagation de fissure, le calcul en parallèle et la technique de transfert de champs sont décrits. Le comportement élastique de l'éprouvette en titane pur est étudié dans le chapitre 3. La simulation de propagation de fissure dans les monocristaux est effectué dans le chapitre 4. Ensuite, cette méthode de simulation est appliquée au bicristaux et le polycristal dans le chapitre 5. Enfin, la conclusion et les perspectives du travail sont présentées dans le chapitre 6.

Chapter 1

Bibliography

In order to simulate short fatigue crack propagation, a 3D Finite Element mesh is required. This mesh will be constructed from X-ray tomographic images. Thus, the principle of X-ray tomography and grain reconstruction method are presented in Section 1.1. In this section, the experimental fatigue test that is carried out in the CRYSTAL project and that will be used through this dissertation is also summarised. Then, a literature review of (FE) simulations using crystal plasticity models in polycrystalline materials is given. The mechanisms of fatigue deformation, short fatigue crack propagation and damage evolution laws are introduced in the last two sections.

Résumé

Afin de simuler la propagation de fissure courte dans un maillage réel 3D obtenu par la tomographie aux rayons X, le principe de la tomographie aux rayons X et la méthode de reconstruction de grain sont d'abord présentés dans la Section 1.1. L'expérience in-situ de fatigue effectuée dans le cadre du projet CRYSTAL qui est cité tout au long de la thèse est également résumée dans cette section. Ensuite, une revue de la littérature est menée sur la simulation par éléments finis en plasticité cristalline dans un matériau polycristallin. Les mécanismes de la déformation par fatigue, la propagation de fissure courte et les lois d'endommagement sont résumés dans les deux dernières sections.
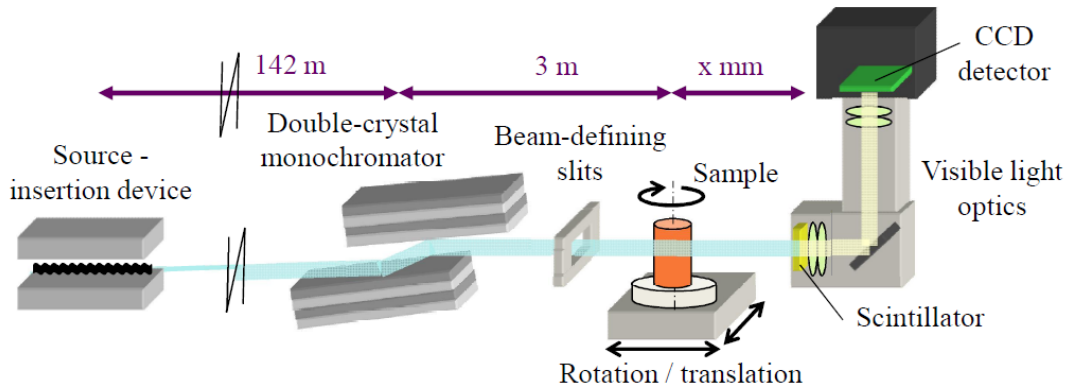
FIGURE 1.1: Beamline ID19 setup at the ESRF [Herbig, 2011].

1.1   X-ray Tomography

The mechanical properties of polycrystalline materials are governed by their microstructure. Hence, a quantitative description of microstructure is important in materials science. X-ray tomography, which first appeared in the 1970's [Hounsfield, 1973] has rapidly evolved since then, and allows characterising materials nondestructively, by sections in 3D.

The *in situ* experiments simulated in this work were performed at the Europeen Synchrotron Radiation Facility (ESRF) in Grenoble (France) with the beamline ID19, mainly by the team at *INSA LYON*. A synchrotron is a particle accelerator in which the charged particles are accelerated using a synchronised magnetic field. Compared to laboratory sources, the radiation is much brighter. Thus, the mesurements are more accurate and require shorter aquisition times.

The setup of the beamline ID19 at the ESRF is shown in Figure 1.1. In order to reduce artefacts in the image reconstruction, the incoming beam is monochromatised by a double-crystal monochromator according to Bragg's law

$$n\lambda = 2d\sin\theta, \tag{1.1}$$

with n an integer, λ the incident wavelength, d the inter-lattice spacing and θ the diffraction angle. Thanks to Bragg law, the selection of photon energy is very precise, typically $\Delta\lambda/\lambda = 10^{-4}$ Then, the beam arrives at the sample, which is mounted on a rotational and translational stage. The intensity of the transmitted

radiation I_x is described by the Beer-Lambert law

$$I_x = I_0 \exp(-\mu x), \tag{1.2}$$

with I_0 the intensity of the incident radiation, μ the attenuation coefficient and x the sample thickness. Afterwards, the transmitted beam arrives at the scintillator [Martin and Koch, 2006] that transforms X-rays into visible light. Finally, the image is captured on a Charge-Coupled Device detector (CCD) [Labiche *et al.*, 2007] from where the charge is transformed into a digital value.

Two types of tomography techniques are used in this work: Diffraction Contrast Tomography (DCT) and Absorption/Phase Contrast Tomography (PCT). Both experiments were carried out using a setup similar to that in Figure 1.1.

1.1.1 Diffraction Contrast Tomography (DCT)

X-ray Diffraction Contrast Tomography (DCT) is a nondestructive technique that allows to determine the microstructure of a polycrystalline sample in the undeformed state. This technique provides the information about grain shapes and crystallographic orientations that will be used in the FE model. It allows also to determine the average elastic strain tensor for each grain during elastic deformation, which can then be compared to the simulated ones.

The principle of DCT is shown in Figure 1.2 [Ludwig *et al.*, 2010]. During acquisition, the sample is rotated through 360° around the rotation axis, indicated by ω in the figure. The X-ray energy was 36 keV. According to Bragg's diffraction law, the parallel monochromatic incident beam is diffracted at a certain angle for each grain. The related transmitted beam forms an extinction spot. On the detector placed closely behind the sample, the corresponding diffraction spots and the extinction spots are displayed in bright and dark gray, respectively. In this experiment, the distance between the detector and the sample was 6 mm. The spots are recorded in a large number of images (7200 images in this work). From the shape and the intensity of the diffraction spots, the shape of grains can be reconstructed using an Algebraic Reconstruction Technique [Gordon *et al.*, 1970].

The grain reconstruction consists of three main steps: segmentation, pair matching and indexing. As a result, a 3D stack of labeled images is obtained. Figure 1.2 (b)
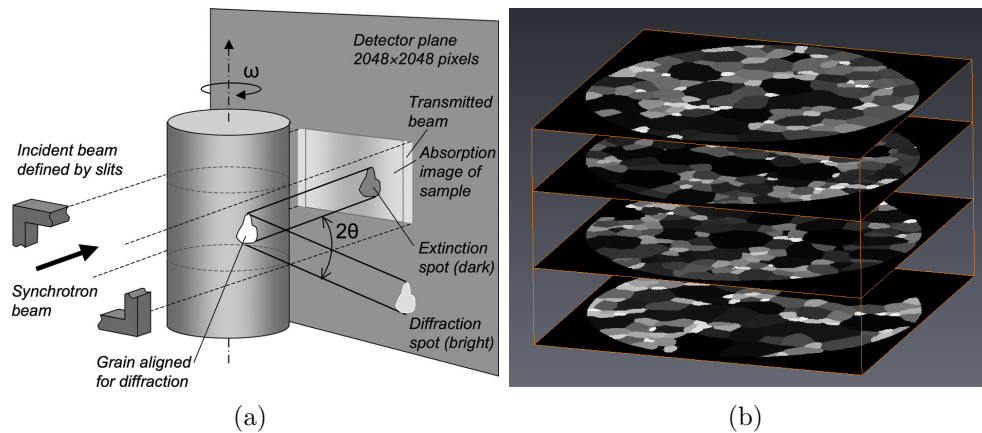
FIGURE 1.2: (a) Schematic representation of the principle of X-ray Diffraction Contrast Tomography (DCT) [Ludwig *et al.*, 2010]. (b) Selected slices of the geometry of the microstructure determined from DCT.

shows an example of the microstructure reconstructed from DCT. Using this type of microstructure, 3D FE meshes will be created in Chapter 2. Then, the Crystal Plasticity FE simulations will be carried out in Chapter 3.

1.1.2   Phase Contrast Tomography (PCT)

When incident beam passes through a cracked sample, the difference in material density will cause a phase shift of the transmitted beam. This produces interface fringes at the boundary between the crack and the sample. Phase Contrast Tomography (PCT) makes the boundary visible, so that crack shapes can be observed in the micrometer range at each stage of *in situ* experiments [Cloetens *et al.*, 1997]. Combined with the grain shapes and orientations provided by DCT, crack growth rates and crystallographic orientations can be analysed [Herbig *et al.*, 2011].

For the PCT experiment, the energy was 50 keV. The pixel size was 1.4 μm. The bone-shaped fatigue specimen is shown in Figure 1.3 (a) and the *in situ* fatigue machine in Figure 1.3 (b). A 25×140 μm rectangular notch was machined by Focused-Ion Beam Machining at the middle of the sample in order to localise stress, crack initiation and subsequent propagation during the *in situ* experiment. The maximum load was 35 N and the load ratio was 0.1. PCTs were carried out at the maximum load at every 1000 cycles before crack initiation and at every 500 cycles during crack growth. The initiation of a crack was observed after 28k
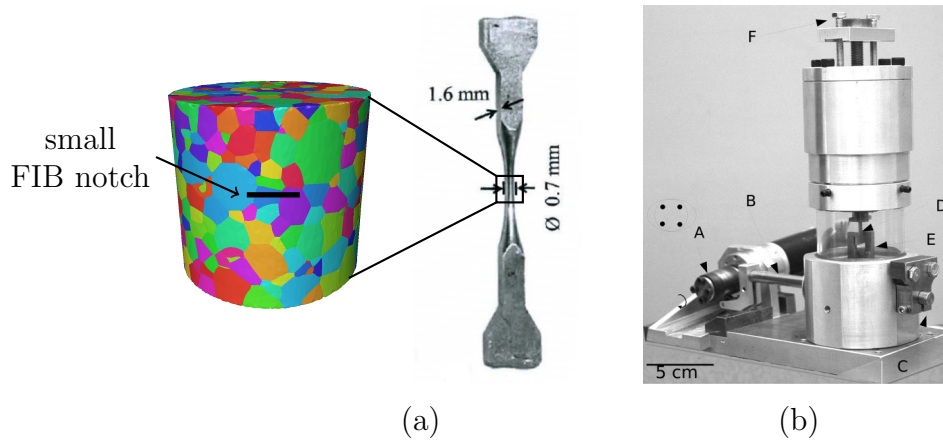
FIGURE 1.3: (a) Small specimen compatible with DCT acquisition and in-situ fatigue testing, (b) In-situ fatigue machine [Buffière *et al.*, 2006].

cycles. Figure 1.4 shows the crack at 129.5k cycles. From Figure 1.4 (b) it can be observed that the crack propagates mainly along {112} and {110} planes.

The simulation method of crack growth will be introduced in Chapter 4, and the crack propagation in this sample will be simulated in Chapter 5. By analysing and comparing the microstructural features and the crack paths between the experimental crack and the simulated one, different crack parameters of in the crack growth criterion will be discussed.

1.2 Crystal plasticity computation in polycrystalline materials

At the grain scale, plastic deformation in metallic crystalline materials is heterogeneous. This heterogeneity results from slip system activation, often described by Schmid's law, which depends on the cristallographic orientation of each individual grain, as well as plastic accommodation with inclusions, porosities or neighbouring grains in the case of polycrystals. In order to take into account the physics of deformation process in polycrystalline materials and effects of cristallographic orientations, the first crystal plasticity models were introduced by [Asaro and Rice, 1977, Hill, 1965, Mandel, 1972]. Then, the models have been extended to rate-dependent polycrystals under large strains. The first practical implementation was presented by [Asaro, 1983]. A phenomenological crystal plasticity model based on slip was proposed by [Méric *et al.*, 1991] in order to analyse activation
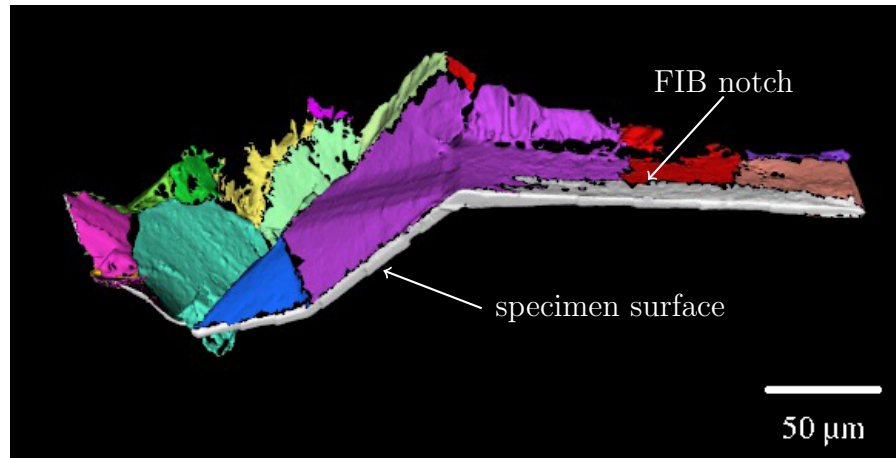
(a)
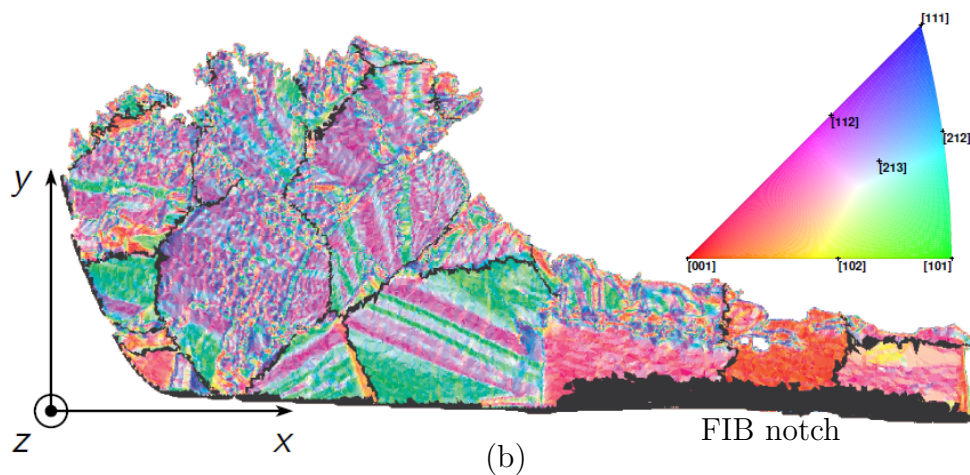
(b)

FIGURE 1.4: Fatigue crack at 129,500 cycles colored by grain numbers (a) and by crack surface normals (b).

of slip systems and plastic strain concentrations in polycrystalline materials under torsion and tension–compression loading. This model, among many others, is implemented in the Z-Set software suite, developed at *Mines ParisTech* and *ONERA* [Besson and Foerch, 1997].

In order to simulate the strain and stress fields in an aggregate polycrystal, a new approach was proposed [Barbe *et al.*, 2001] by coupling the phenomenological model and a 3D Voronoi tesselation, where the grain centers and the crystal orientations are distributed randomly, see Figure 1.5 (a). Several types of boundary conditions were applied to simulate a uniaxial tensile test along *z*-direction. They are the Homogeneous Strain Boundary (HSB) conditions, a Mixed type of
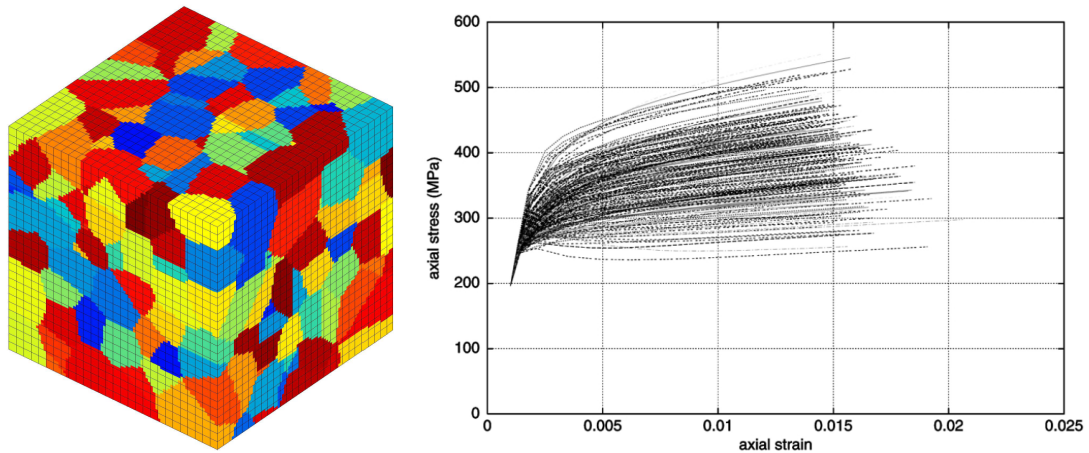
FIGURE 1.5: (a) Voronoi tesselation with 200 grains, (b) The stress-strain (σ_{zz}, ε_{33}) behaviour of each grain under HSB conditions [Barbe *et al.*, 2001].

Boundary (MB) conditions, one lateral Free Face (1FF) and four lateral Free Faces (4FF). HSB conditions imposed all components (U_x, U_y and U_z of displacement vector of the outer faces of the cube. MB conditions set the components U_x and U_y to zero. Whereas, 1FF conditions imposed U_z on the top and bottom face and U_x or U_y on the three lateral faces. 4FF imposed only U_z at the top and bottom faces.

Figure 1.5 (b) shows the stress-strain behaviour of individual grains under HSB conditions. The heterogeneity between grains depends on the crystallographic orientation, the number of neighboring grains and their size, morphology, position and orientation. The effect of different boundary conditions on the number of active slip systems and the amount of plastic slip was also investigated. It was proved that HSB conditions produce the highest amount of plastic slip, which can be explained by the effect of a softened free surface. For a free surface, the plastic deformations develop more freely. Thus, low number of plastic systems are activated and low amount of plastic slip is produced. The biggest grain in the aggregate was analysed. By comparing with a single crystal with the same crystal orientations, it was found that the effect of surrounding grains is more important than that of free surface to the number of slip systems activated.

Instead of using the Voronoi synthetic aggregates, with the development of the microstructural characterisation techniques, realistic mesh reconstructed from the

characterised grain shapes has emerged. A new methodology by coupling the crystal plasticity simulations using the realistic 2D FE mesh and plain-strain compression experiments is proposed by [Raabe *et al.*, 2001] to investigate the influence of microstructural parameters and macroscopic boundary conditions. After each step of plastic deformation, grain orientation is determined by Electron Back Scattering Diffraction (EBSD). The displacement field and the plastic strain distribution are calculated by a photogrametric method. After the total macroscopic strain of the sample of 8%, the measured von Mises strain at some grid points reaches to 1%, whereas others show much higher strains, particularly close to grain boundaries. The deviation of the stain reaches to 87.5% from the average value.

Then, both crystal plasticity and continuum simulations (without considering the crystal orientations) are carried out using the same FE mesh and the boundary conditions that are the experimentally measured 3D displacement field. With a qualitative comparison of the crystal plasticity and the continuum FE simulations, it was shown that the strain gradients in each grain are influenced by the boundary conditions and the sample geometry, whereas strain localisation at grain boundaries is affected by crystal orientation and misorientation. Moreover, by an analysis of the experimental plastic strain distribution and the micromechanical Taylor factor calculated from the crystal plasticity simulations, it was shown that strain localisations occured at most grain boundaries at triple points. However, this comparison of strain field between the simulations and the experiments remains qualitative.

A quantitative study is carried out by [Héripré *et al.*, 2007] for optimisation of parameters of the crystal plasticity model, using a 3D FE mesh obtained from an extrusion in the third direction of the 2D EBSD surface mesh, see Figure 1.6. According to a study of the influence of mesh thickness, it is chosen as equal to the average grain size. In order to study the influence of neighbouring grains, two different boundary conditions are applied: homogeneous strain and experimental displacements as measured by an image correlation technique. The comparison between these boundary conditions shows that the axial strain (ε_{xx}) localisation is lower with the homogeneous strain boundary conditions, espacially near the mesh boundary. Therefore, the experimental boundary conditions are more realistic for small aggregates which do not form a Representative Volume Element (RVE). Then, the simulation results are compared to the experimental axial strain field.
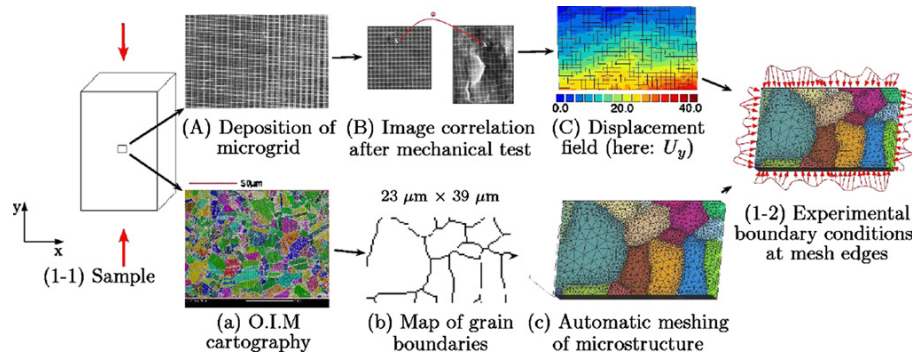
FIGURE 1.6: Methodology of coupled experimental tests and FE simulations [Héripré *et al.*, 2007]

As a result, higher strain heterogeneity is found for the experimental measurements. The FE mesh size and the element type effects are also studied. There are no significant influences on the strain pattern, except for its intensity. Thus, in order to minimise the differences between the experimental results and the simulated ones, an optimisation method of the parameters of the crystal plasticity model is proposed, because the parameters corresponding to the same macroscopic behaviour may produce very different local deformation mechanisms.

The previous studies of polycrystalline materials show the behaviour of individual grains is very sensitive to their neighbouring grains numbers, shapes and orientations, as well as the applied boundary conditions. A literature review of recent experimental and modeling advances in microstructure sensitive approaches is given in [Castelluccio *et al.*, 2014]. In order to consider the effect of all the neighbouring grains, and to conduct a quantitative grain-to-grain comparison of strains, it is necessary to use a 3D realistic mesh in crystal plasticity FE simulations, as shown in Figure 1. This type of simulation is also relevant to predict plastic strain localisation that affects significantly the nucleation and propagation of short fatigue cracks, which is one of the objective of this work. After reviewing the mechanisms of cyclic deformation and short fatigue crack propagation in the following two sections, the mesh reconstruction technique is described in chapter 2. A comparison of average elastic strain in each grain between experimental measurements and FE simulation is explained in chapter 3.

1.3 Mechanisms of cyclic deformation

Plasticity is considered as the origin of fatigue crack initiation. In this section, the mechanisms of plastic deformation under fatigue loading are reviewed in single crystals and in polycrystals. Although the detail of the mechanisms will not be simulated in CPFE calculations, they are important to analyse crack initiation and propagation.

1.3.1 Single crystals

Cyclic hardening and saturation behaviour over a wide range of plastic strain amplitudes in copper single crystals was investigated by [Mughrabi, 1978]. Connecting the extrema of the stable hysteresis loops, as shown in Figure 1.7 (a), a fatigue limit is observed for the formation of a Persistent Slip Band (PSB) structure. Observed by [Thompson *et al.*, 1956], the name *persistent* originates from the fact that if the test is interrupted and the slip traces are removed by polishing, these bands appear again at the same locations on subsequent loading. They are considered as preferential sites for the initiation of fatigue cracks. The cyclic stress-strain curve is divided into three regimes, see Figure 1.7 (b). The corresponding observations of the dislocation arrangements are described as following [Ackermann *et al.*, 1984, Winter, 1974]:

- Regime A corresponds to low amplitudes of plastic slip γ_{pl}:

  Fully reversed cyclic strain produces approximately equal amounts of positive and negative edge dislocations on the primary slip planes. Two edge dislocations with opposite sign are attracted over small distances to form primary edge dislocation dipoles. The clusters of primary edge dislocation dipoles constitute vein (or bundle) structures, see Figure 1.8 (a). The veins are separated by channels, in which screw dislocations ply back and forth during cyclic deformation. When dislocation dipoles move to the surface, extrusions and intrusions surface relief can be observed. The work hardening observed in Figure 1.7 (b) is due to the accumulation of primary dislocations.

(a)

(b)
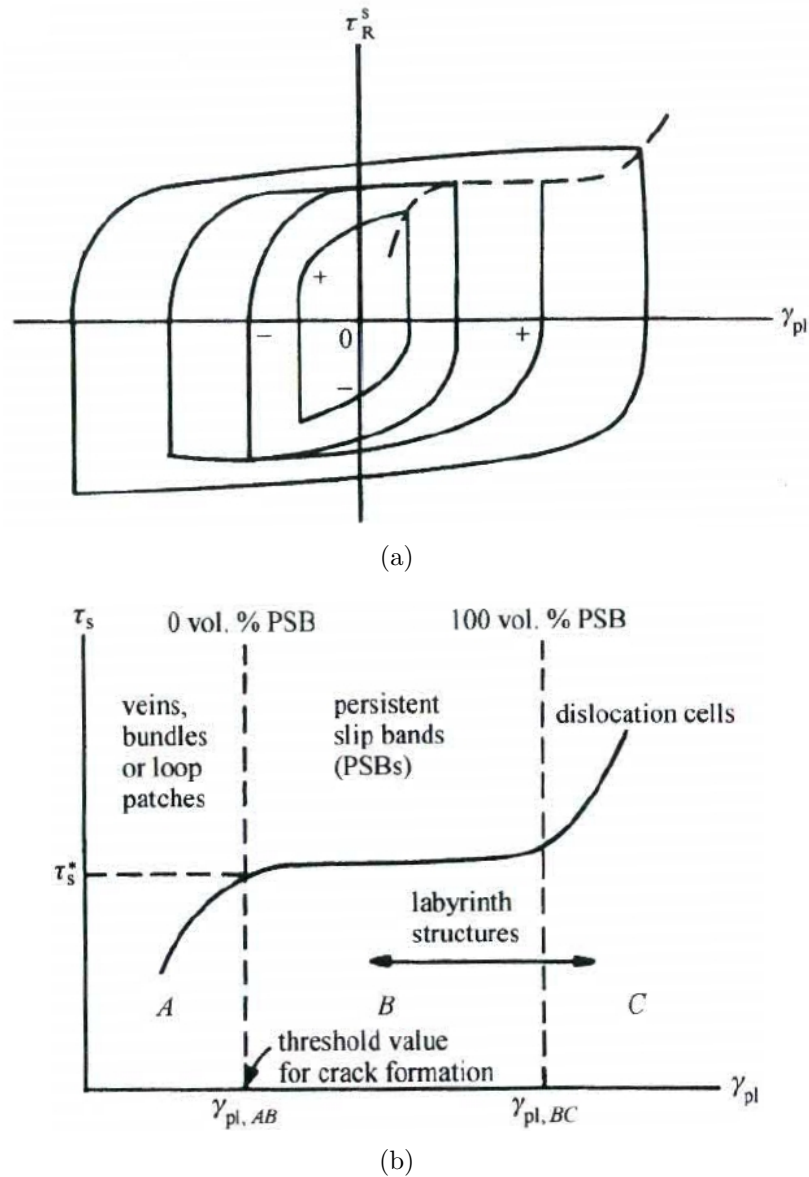
FIGURE 1.7: (a) Hysteresis loops with the resolved shear stress τ_R^s at saturation varies with the plastic slip amplitude γ_{pl} of copper (b) Different regimes of the saturation stress τ_s – plastic strain amplitude γ_{pl} curve [Suresh, 1998].

- Regime B corresponds to intermediate amplitudes of plastic slip γ_{pl}:

In region B, the saturation stress is independent of the plastic strain. With increasing γ_{pl}, the vein density increases and the structure becomes unstable. Therefore, the veins break down locally. They are converted into a softer PSB with the wall structure, see Figure 1.8 (b), perpendicular to the primary Burgers vector. A periodic arrangement of walls divides the PSB into channels containing mainly screw dislocations. Once PSBs form, plastic
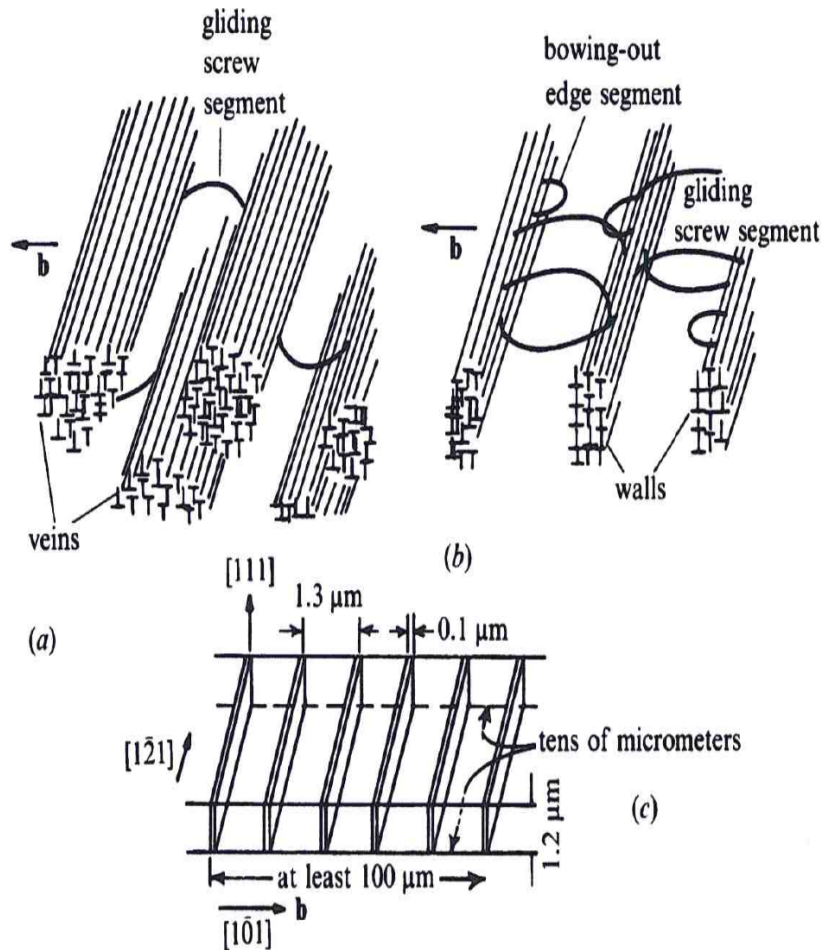
FIGURE 1.8: Dislocation arrangements in F.C.C. metals [Suresh, 1998].

strain concentrates increasingly in them. The independence of τ_s from γ_{pl} in Figure 1.7 (b) is due to an equilibrium between dislocation multiplication and annihilation of dislocations in the channels and in the walls. The volume fraction of the PSBs increases up to 100% when γ_{pl} reaches $\gamma_{pl,BC}$, see Figure 1.7(b).

- Regime C corresponds to high slip amplitudes γ_{pl}:

The density of PSBs of the primary slip system cannot increase anymore and the crystal rotates with respect to the loading axis in order to accommodate the imposed deformation. The secondary slip systems are activated with an increased amplitude of γ_{pl}. Then, the vein matrix transforms to labyrinth structure containing secondary dislocations. The increase in dislocation density facilitates the formation of dislocation cell structure which

fills the PSBs. The interactions among different slip systems in the labyrinth and cell structure make the corresponding shear stresses higher.

However, the BCC single crystals behave significantly differently with respect to the FCC single crystals. [Mughrabi *et al.*, 1981] have investigated the fatigue behaviour of BCC α-iron. It was found that, due to the particular sessile core structure of the screw dislocations, the dislocation glide behaviour of BCC metals was strongly dependent on temperature, strain rate as well as on the interstitial impurity content. Different slip planes are observed in tension and compression of cyclic deformation tests due to non equivalence of forward and reverse glide of the screw dislocations.
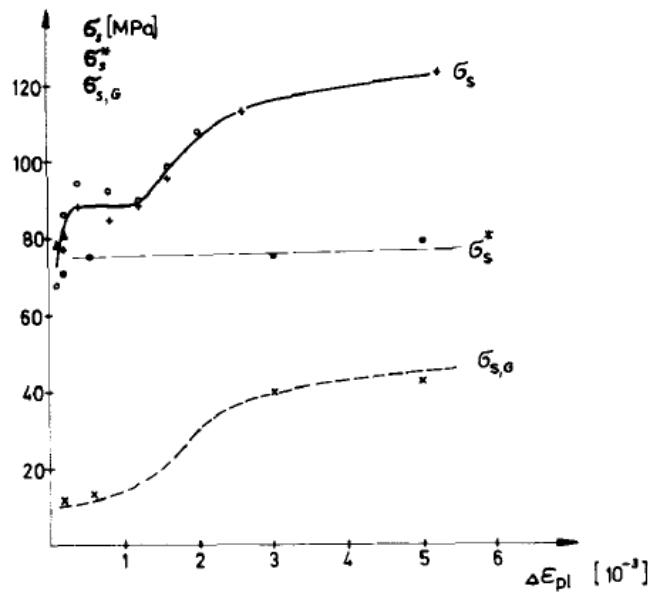
FIGURE 1.9: Cyclic stress strain curves of decarburized α-iron BCC single crystal at room temperature with high strain rate. $\Delta\varepsilon_{pl}$ is the plastic strain amplitude. σ_s is the cyclic saturation stress. $\sigma_{s,G}$ denotes the athermal component that is related to the dislocation density, and σ_s^* denotes the effective stress due to the lattice friction stress [Mughrabi *et al.*, 1981].

Figure 1.9 shows the cyclic stress strain curve of decarburized α-iron BCC single crystals at a strain rate of about 10^{-2}s^{-1} at room temperature. Compared with Figure 1.7 of FCC single crystals, some differences are noteworthy. First, in the region of low plastic strain amplitudes $\Delta\varepsilon_{pl}$, the cyclic saturation stress σ_s increases rapidly. However, this is not due to an increase of the dislocation density, because the athermal component $\sigma_{s,G}$ is still low, as shown in Figure 1.9, but to

the increase of the lattice friction stress σ_s^*. Contrary to the deformation mechanisms in FCC monocrystals, the veins do not form at low $\Delta\varepsilon_{pl}$. Second, in the small plateau region, the PSBs were not observed in the decarburized α-iron BCC single crystals. Finally, in the regime of high $\Delta\varepsilon_{pl}$, the dislocation cell structure was formed as a result of slip activities on primary and secondary slip systems. The cyclic hardening in this area can be explained by screw dislocation glide and effects of cell structure.

In this subsection, the mechanisms of plastic deformation in FCC and BCC single crystals are described at the micron scale. They are primordial to understand the plastic deformation at the cyclic hardening and softening in polycrystals in the next paragraph. The plastic slip will be used in the Crystal Plasticity models in Chapter 3. The primary and secondary slip system will be addressed to analyse small fatigue crack planes in Chapter 5.

1.3.2 Polycrystals

The presence of grain boundaries alters the fatigue behaviour of polycrystalline materials with respect to single crystals. They are considered as barriers to dislocation motion during the early stages of plastic deformation. The role of grain boundaries during deformation in a polycrystalline aluminium was investigated by [Dingley and Pond, 1979]. It has been observed that crystal dislocations can enter grain boundaries and then dissociate into component dislocations. According to the difficulty of dissociation and separation, grain boundaries can be classified into hard and soft boundaries. The interactions of crystal dislocations with grain boundary dislocations accommodate deformations between adjacent grains. The effect of grain size and texture on the cyclic behaviour of copper polycrystals have been investigated by [Llanes *et al.*, 1993]

The cyclic behaviour of polycrystalline materials is usually characterised by the cyclic stress-strain curves of stress-controlled or strain-controlled fatigue experiments. The cyclic hardening and softening of materials, followed by stable hysteresis loops are observed in the case of constant-amplitude fatigue loading. A survey of literature on the development of dislocation structures in FCC polycrystals is provided in [Suresh, 1998]. In general, cyclic hardening is observed in well-annealed polycrystalline metals due to dislocation multiplication, while cyclic softening is caused by the rearrangement of prestrain-induced dislocation

networks. The cyclic saturation stage is believed to result from the equilibrium between dislocation emission from cell walls and dislocation annihilation at adjacent walls.

In most polycrystalline materials, after the first plastic loading in tension or compression, the yield stress becomes lower when the direction of loading is reversed. This phenomenon is called the Bauschinger effect, Figure 1.10(a). It was observed by J. Bauschinger in 1886. The mechanisms of Bauschinger effect in aluminium polycrystals are studied by [Hasegawa *et al.*, 1986]. During forward deformation, dislocation walls (or subgrain-boundaries) form in order to minimize energy. However, they are metastable structures that will rearrange during unloading and reverse loading. The disintegration of the cell walls (or subgrain-boundaries) is responsible for the Bauschinger effect.
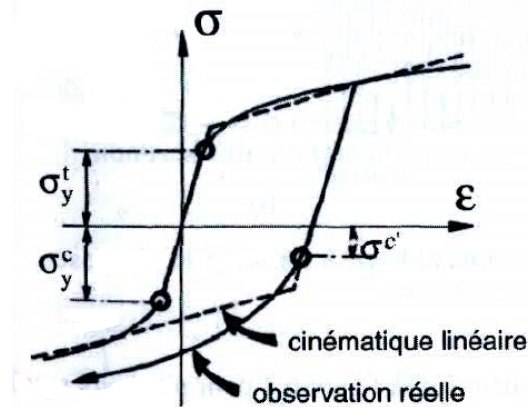
(a)
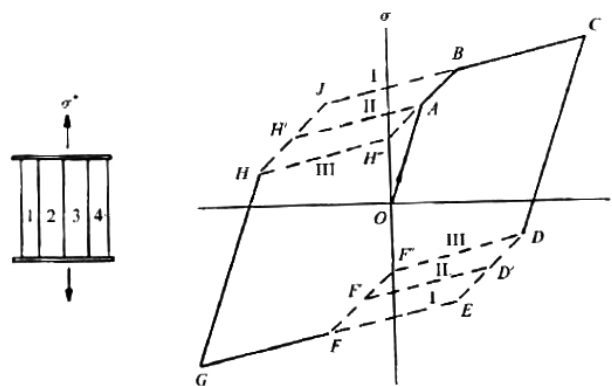
(b)

FIGURE 1.10: (a) Bauschinger effect [Lemaitre *et al.*, 2009]. Stress-strain curve under tension-compression loading, σ_y^t yield stress in tension, σ_y^c yield stress in compression, $\sigma_y^{c'}$ yield stress in compression after tension chargement. (b) Three types of kinematic hardening [Asaro, 1975].

The Bauschinger effect needs to be taken into account in the constitutive models for cyclic plastic deformation in polycrystalline materials. Figure 1.10(a) shows a particular curve representing the kinematic hardening. Asaro [1975] has considered three types of kinematic hardening, see Figure 1.10 (b), based on the theory of Masing that assumed n elastic plastic elements as shown in Figure 1.10 (b).

- Type I: first elements to deform will be the first to relax (OABCDEGHJB in Figure 1.10 (b))

  First in-first out type: if internal structures form in a sequence of α, β, γ, then the recovery has the sequence 2α, 2β, 2γ. This type of hardening can be interpreted microstructurally by the model of dislocation pile-ups in cell structures for polycrystalline materials and in wall structures for single crystals. During reverse loading, the opposite dislocations annihilate the existing dislocations first and then pile-up in such structures. The type I hardening can explain the Bauschinger effect in a number of alloys.

- Type II: first structures to form are the first to relax util they disappear (OABCDD'F'FGHH'AB in Figure 1.10 (b))

  The sequence of recovery of the internal structures is α, β, γ. This type of hardening can describe reversible twinning.

- Type III: last structures to form are the first to relax (OABCDF"FGHH"AB in Figure 1.10 (b))

  Last in-first out: the recovery sequence is γ, β, α. A microstructural model of this type of hardening is the nucleation and collapse of Orowan loops. During the loading stage, the Orowan loops are created by bowing around particles of mobile dislocations. The initial yield stress is related to the critical forces to begin the bowing process. Then, the dislocation loops accumulate on the slip planes. When the reverse loading occurs, the last loop formed is the first to collapse.

The cyclic behaviour of polycrystalline materials were reviewed in this subsection. The cyclic hardening, softening behaviour and Bauschinger effect will be simulated in Chapter 3.

1.4 Short fatigue crack growth

During fatigue loading, dislocations accumulate at grain boundaries, twin boundaries, inclusions, porosities and slip bands. The accumulation creates stress concentrations which can induce crack initiation. In the in-situ fatigue experiments, a notch was machined in the sample to control the crack initiation location. Therefore, the mechanism of crack initiation is not studied. In the following section, the mechanisms of short fatigue crack propagation and damage evolution laws will be presented.

1.4.1 Mechanisms of fatigue crack growth

After crack nucleation, cracks are said microstructurally short when they have a dimension comparable to a characteristic length of the microstructure, such as the grain size. A review of fatigue crack growth is given by [Newman, 1998]. Short fatigue cracks usually grow through two distinct stages: stage Ia in the direction of primary slip and stage Ib leading to striations by activation of complex slip [Forsyth, 1963], see Figure 1.11. When the crack length exceeds several grains, the plastic zone of the crack tip becomes large. The crack propagates along a plane oriented to the maximum normal tensile stress, no longer along a crystallographic plane.

A physical model of stage II ductile fatigue crack growth based on plastic blunting of the crack tip is proposed by [Laird and Smith, 1962], see Figure 1.12. During tensile loading, the crack of length a opens and the crack tip becomes rounded. The blunting process is related to an extension of the crack tip at about $\pm 60°$ to the crack plane. During compression, the crack closes and due to the irreversibility part of the plastic deformation, the crack tip grows by a distance of Δa and forms a striation. This model implies that each striation corresponds to one complete fatigue cycle. However, this result is not relevant for short fatigue crack propagation, which will be explained below.

A physical model for the activation of multiple slip systems in copper single crystals was suggested by [Neumann, 1969], see Figure 1.13. This model explains the stage Ib 'zig-zag' short fatigue crack growth path by the alternating change of the operating slip band due to work hardening along the slip bands. During the loading

phase, work hardening occurs in the first slip band because the free dislocations run on the first activated slip plane and form dislocation dipoles which are stable for a larger stress amplitude. If the tensile stress amplitude is high enough, a second slip system will be activated along slip plane 2. During unloading and reverse loading, dislocations move back leading to Figure 1.13 (c). Then, during reloading, the slip on the alternative plane is activated, which is still unhardened, as shown in Figure 1.13 (d).
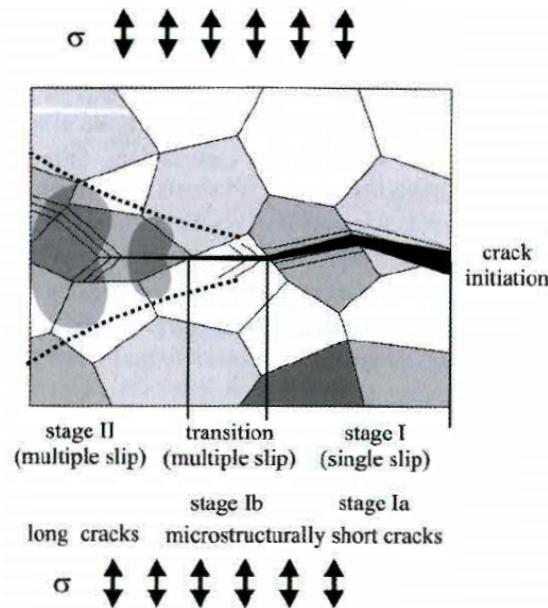
FIGURE 1.11: Stage I and stage II crack propagation in polycrystalline metals [Krupp, 2007]

The short crack propagation path and rate are strongly influenced by the interactions with microstructural features, such as grain boundaries, precipitates, etc. Twist and tilt angles of the crack plane are identified as a key factor for the short fatigue crack growth path through a grain boundary [Zhai *et al.*, 2000]. In Figure 1.14 (a), the twist α is defined as the angle between the traces (*ab* and *ac*) of the crack planes in the two neighboring grains on the grain boundary. The tilt angle β represents the angle between the intersections (*ae* and *af*) of the crack planes on the sample surface. A stage I fatigue crack growth model is proposed. In order to reduce the twist deflection, steps are generated on the fracture surface as shown in Figure 1.14 (b).

A quantitative analysis of the short fatigue crack growth path is carried out by [Zhai *et al.*, 2005]. They observed that the grain boundaries have a higher resistance to the growth of short fatigue cracks when the angle α is large. A crack can only cross the grain boundary with low α angle.
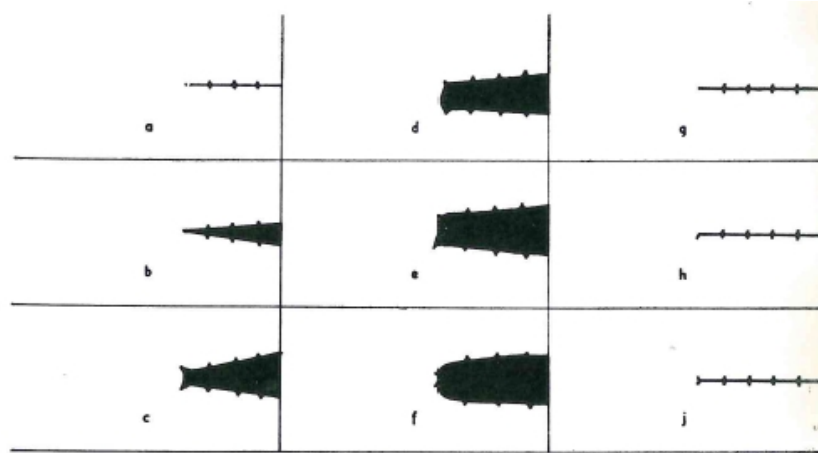
FIGURE 1.12: Schematic representation of Laird's model [Laird and Smith, 1962]. (a) Specimen in compression, crack closed. (b) Specimen pulled into Bauschinger range, crack opens. (c) Specimen strained further, initial marked plastic deformation at the crack tip. (d)(e)(f) Alternative contours developed at the full plastic strain. (g)(h)(j) Crack tip geometries which correspond to (d)(e) and (f) respectively, on compressing the specimen.
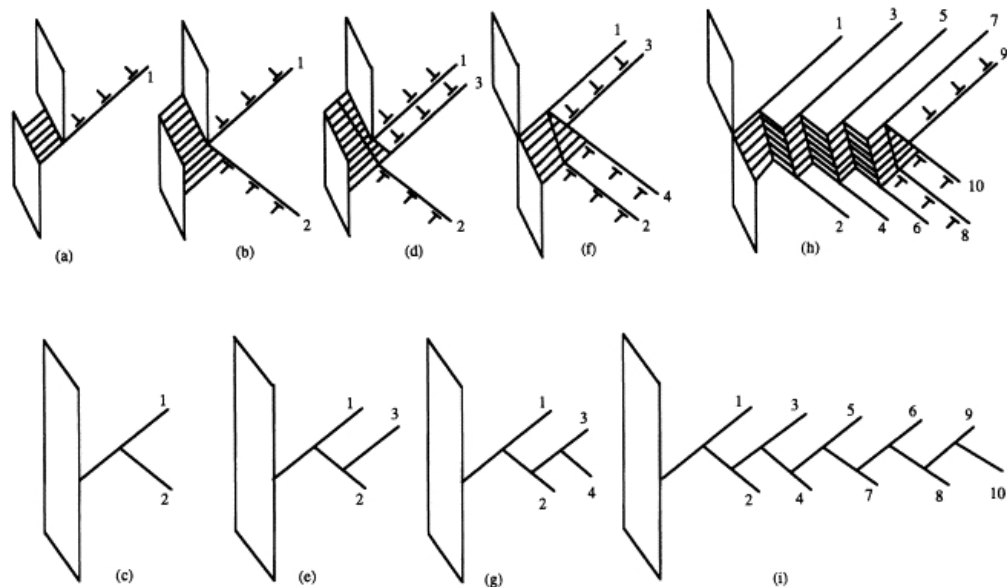
FIGURE 1.13: (a) Neumann's model of crack propagation (b) Influence of grain misorientation in short crack propagation.

A 3D investigation of the interaction between fatigue cracks and grain boundaries was performed by [Schaef and Marx, 2012, Schaef *et al.*, 2011] using Focused Ion Beam (FIB) tomography in a Ni-based superalloy. The grain orientations are characterised by Electron Back Scattered Diffraction (EBSD). The grain boundaries with compatible slip systems were selected. The pre-cracks in the selected grains were machined by FIB cutting on the slip planes with the highest Schmid factors. Pre-cracks with different distances to the same grain boundary were also produced.
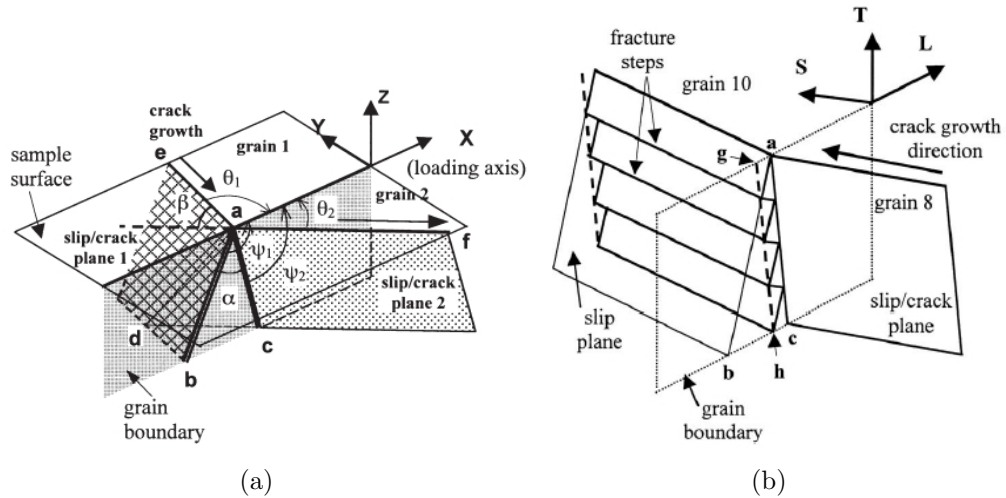
FIGURE 1.14: (a) Schematic representation of twist (α) and tilt (β) misorientation angles (b) Crystallographic model of Zhai [Zhai *et al.*, 2000] for grain boundary crossing
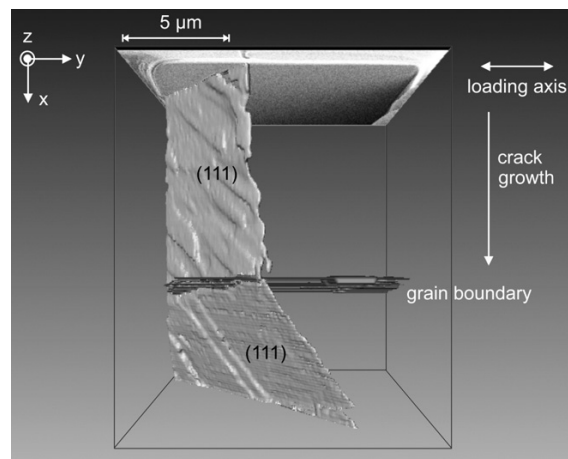
FIGURE 1.15: 3D crack growth path through the grain boundary obtained by FIB tomography [Schaef *et al.*, 2011].

After the fatigue tests, the crack growth rate was determined by Scanning Electron Microscopy (SEM). As a result, crack retardation was observed for all the cracks when the plastic zone reached the grain boundaries due to the reduced dislocation mobility at the grain boundaries. The small cracks that have a size smaller than 30 μm stopped in front of the grain boundaries. Figure 1.15 shows that the crack path changed at the grain boundary. However, in the second grain the crack does not necessarily propagate on the slip plane with the highest Schmid factor.

1.4.2 Damage evolution laws

Damage evolution laws that describe the evolution of damage from the undamaged state until nucleation of a fatigue crack have been developed extensively over the last few decades. Two types of approaches have developed: the global approach to fracture based on the concept of linear elastic fracture mechanics and the local approach to fracture based on the failure micromechanisms. The global approach is used to determine the propagation behaviour of large fatigue cracks (stage II). In order to simulate the short crack propagation that depends strongly on the microstructures, the local approach is discussed in the following. A continuous damage variable D is defined as: $D = 0$ when there is no damage, $D = 1$ when the material is totally damaged.

The classical models describe damage evolution with stress and strain parameters. In the 1860s, Wöhler observed an endurance limit representing the stress level below which the material exhibits an infinite fatigue life. [Basquin, 1910] proposed a exponential relation in a fully reversed, constant amplitude High Cycle Fatigue (HCF) ($N_f > 10^4$ cycles) test between the stress amplitude ($\Delta\sigma$) and the number of loading cycles to failure (N_f):

$$\frac{\delta D}{\delta N} = f(\Delta\sigma) = \left(\frac{\Delta\sigma}{2\sigma_c}\right)^b, \tag{1.3}$$

with N the number of cycles, σ_c and b material parameters. After integration, this yields

$$N_f = \left(\frac{\Delta\sigma}{2\sigma_c}\right)^{-b}. \tag{1.4}$$

This model was modified by [Morrow, 1968] in order to take into account mean stress effects (σ_m):

$$N_f = \left(\frac{\Delta\sigma}{\sigma_c - \sigma_m}\right)^{-b} \tag{1.5}$$

[Coffin, 1954, Manson, 1953] noticed that the strain amplitude effects become important when strain localisation occurs for the Low Cycle Fatigue (LCF) regime ($N_f \leq 10^4$ cycles). Instead of stress amplitude in Basquin's model, they introduced plastic strain amplitude ($\Delta\epsilon_p$) into the damage law:

$$\frac{\delta D}{\delta N} = f(\Delta\varepsilon) = \left(\frac{\Delta\varepsilon_p}{2\varepsilon_c}\right)^c, \tag{1.6}$$
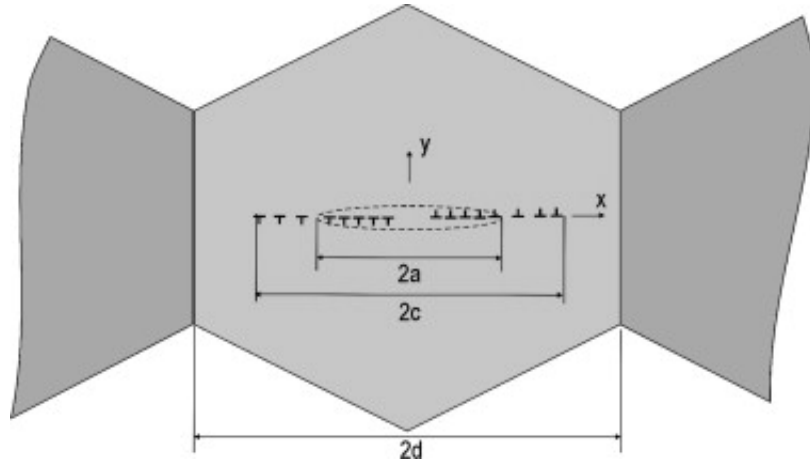
FIGURE 1.16: Schematic representation of BCS model in a single grain

with ε_c and c material parameters, so that

$$N_f = \left(\frac{\Delta\varepsilon_p}{2\varepsilon_c}\right)^{-c}. \tag{1.7}$$

[Bilby *et al.*, 1963] (BCS model) describe the crack tip sliding displacement $\Delta CTSD$ by integrating the number of dislocations emitted in the plastic zone as following:

$$\Delta CTSD = \left(\frac{4\tau^*a}{\pi^2 A}\ln\left(\frac{c}{a}\right)\right), \qquad A = \frac{G}{2\pi(1-\nu)} \tag{1.8}$$

where $2a$ is the crack length, $2c$ is the crack length with the plastic zones, see Figure 1.16, G and ν are the shear modulus and the Poisson ratio and τ^* is the resistance to motion of dislocations.

The crack growth rate in the BCS model in a single grain is :

$$\frac{\delta a}{\delta N} = C \cdot \Delta CTSD^n \tag{1.9}$$

with C and n material parameters.

In fact, the BCS model was proposed for a stage I brittle crack growth. However, it can also be used for fatigue crack propagation in single crystal without microstructural barriers. Based on this model, [Edwards and Zhang, 1994, Navarro and de Los Rios, 1988, Tanaka *et al.*, 1986] proposed models for small fatigue crack growth interacting with grain boundaries. The process of crack growth, deceleration, path through grain boundaries and acceleration are described. [Doquet, 1999] takes into account the effect of normal stress on the crack tip.

A phenomenological incremental damage evolution law was introduced by [Lemaitre *et al.*, 2009], that avoids the notion of cycles. This model can be applied to complex loading and anisotropic materials. For uniaxial tension

$$\dot{D} = \left(\frac{Y}{S}\right)^s \dot{p} \tag{1.10}$$

with S and s damage parameters, p the cumulated plastic strain and Y the strain energy density, defined as

$$Y = \frac{1}{2}\underset{\sim}{\varepsilon}^e : \underset{\approx}{E} : \underset{\sim}{\varepsilon}^e$$

with $\underset{\approx}{E}$ the elasticity tensor.

A 2D micromechanical approach based on crystal plasticity was used by [Bennett and McDowell, 2003] to determine grain orientation effects on crack initiation and stage I crack propagation in HCF regime. Each grain was represented by one element with random grain orientation, therefore, the effects of grain size and grain morphology were not studied. Only a planar double slip is considered. The distribution of three local Fatigue crack Initiation Parameters (FIPs) is calculated in the polycrystalline aggregate to understand the origin of crack initiation and assess fatigue limits.

In HCF regime, the stress amplitude is lower than the macroscopic yield stress. Thus, the microscopic slip localisation plays a key role in crack initiation and growth. The first FIP is as a function of the maximum cyclic plastic shear strain amplitude ($\Delta\gamma^\alpha_{max}$) on the slip system α, defined as

$$FIP_1 = \frac{\Delta\gamma^\alpha_{max}/2}{\Delta P/2}, \tag{1.11}$$

with ΔP the average plastic strain over all grains.

The second FIP takes into account the maximum normal stress (σ^{max}_n) to the slip plane [Fatemi and Socie, 1988], according to

$$FIP_2 = \frac{\Delta\gamma^p_{max}}{2}\left(1 + k\frac{\sigma^{max}_n}{\sigma_y}\right), \tag{1.12}$$

with σ_y the cyclic yield strength and $k = 0.5$ a material parameter obtained by fitting the uniaxial data versus the pure torsion data.

The third FIP involves the maximum resolved shear stress amplitude (τ^α_{max}) and the hydrostatic stress (P_{hyd}), as proposed by [Dang Van *et al.*, 1989] using the Mohr-Coulomb parameter (k) within individual grains:

$$FIP_3 = \frac{\Delta\tau^\alpha_{max}}{2} + kP_{hyd}, \tag{1.13}$$

with P_{hyd} the hydrostatic stress:

$$P_{hyd} = 1/3(\sigma_1 + \sigma_2 + \sigma_3),$$

with $\sigma_1, \sigma_2, \sigma_3$ the principal stresses.

A crack propagation law is introduced of the form

$$\frac{\delta a}{\delta N} = C(FIP^m - FIP^m_{th})a = C'(\Delta CTD - \Delta CTD_{th}) \tag{1.14}$$

with C and m material parameters, FIP_{th} the threshold of FIP, ΔCTD crack tip displacement. Comparing to the experimantal observations of crack length distribution, FIP_2 correlated better with the final crack length than the other two FIPs. The normal stress on the slip plane influences initiation and propagation of small fatigue cracks. Afterwards, [McDowell and Dunne, 2010] applied this approach to 2D realistic microstructural mesh determined by EBSD. The cumulative plastic strain p is considered as a FIP for crack initiation, defined as:

$$p = \int_0^t \sqrt{\dot{\varepsilon}^p_{ij}\dot{\varepsilon}^p_{ij}}dt. \tag{1.15}$$

The results and the comparisons with experimental observations of crack indicate that the localisation of p is important for fatigue crack initiaion and growth. There is no significant difference between the distributions of cumulative plastic strain and the energy dissipation criterion, as proposed by [Korsunsky *et al.*, 2007]:

$$W = \int_0^t \sum_{\alpha=1}^\alpha \tau_\alpha\dot{\gamma}_\alpha dt \tag{1.16}$$

The damage evolution laws are reviewed in this section. Some of the damage variables (or FIPs) will be investigated in Chapter 4 and Chapter 5 in the CPFE simulations.

1.4.3   Numerical approaches of crack growth simulation

In order to simulate 3D crack propagation, different advanced numerical methods have been developed during the last 20 years. A summary of these methods can be found in [Lemaitre *et al.*, 2009].

1. The Cohesive Zone Model (CZM)

The CZM is a general method for modeling ductile and brittle fracture in either cracked or uncracked structures. It was developed from [Barenblatt, 1962, Dugdale, 1960] models that separate a structure into a stress-free part and a plastic process zone. In Finite Element (FE) applications, interface elements of zero width are considered on the crack path. The behaviour of the cohesive zone elements is defined by a softening function that describes the relation between the crack opening and relative stress. A detailed review of CZM and its applications is given by [Chandra *et al.*, 2002, Elices *et al.*, 2002]. Recent application of CZM to simulation of the intergranular fracture in polycrystalline materials using 2D and 3D voronoi mesh is carried out by [Luther and Konke, 2009]. Coupled with remeshing techniques, [Chiaruttini *et al.*, 2012] proposed a method for modeling mixed-mode fatigue crack growth with complex path. However, there are several limitations for the prediction of arbitrary 3D crack paths, such as mesh dependence and determination of material parameters [Scheider and Brocks, 2003].

2. Extended Finite Element Methods (XFEM)

The Extended Finite Element Methods (XFEM) was developed by [Belytschko and Black, 1999] for modeling discontinuities, such as cracks, dislocations or grain boundaries, with minimal remeshing. The fundamental concept is introducing a local partition of unity for enriching finite element approximations. The advantage of the XFEM is the independence of the FE mesh to the evolution of these discontinuities. Therefore, no remeshing or very little remeshing is needed. The state of the art for this method is described in [Belytschko *et al.*, 2009]. The 3D applications are carried out by [Sukumar *et al.*, 2000]. This method can be extended to CZM to simulate complex crack path, such as in [Moës and Belytschko, 2002]. In order to deal with different scales between crack and structural mesh, a global multi-grid algorithm within the XFEM framework is presented by [Rannou *et al.*, 2009]. However, no 3D elastic-plastic application can be found in literature.

3. $G - \theta$ method

$G - \theta$ is a method proposed by [Destuynder *et al.*, 1983] for computing the energy release rate G. In linear elasticity, G verifies

$$\int_{\Gamma} G(s)\underline{\boldsymbol{\theta}}(s) \cdot \underline{\boldsymbol{n}}(s)ds = -\frac{\partial J(\boldsymbol{\theta})}{\partial \underline{\boldsymbol{\theta}}}, \forall \underline{\boldsymbol{\theta}} \in \Theta^{ad},$$ (1.17)

with s curvilinear coordinate along the crack front Γ, $\boldsymbol{\theta}$ the virtual crack extension velocity field for all kinematically admissible field Θ^{ad}, $\underline{\boldsymbol{n}}(s)$ the normal to the crack front Γ, and J the potential energy for all the structure. The fact of using J for all the structure rather than only around crack tip zone like in other methods allows to deal with numerical problems [Destuynder *et al.*, 1983]. For long crack propagation, the Paris crack growth law can then be expressed as follows:

$$\frac{\delta a}{\delta N} = C(G(a))^m,$$ (1.18)

with a the crack length, and C and m the material parameters.

4. Continuum damage mechanics

In the framework of continuum damage mechanics, [Rice, 1987] predicted the strain localisation in elastic-ideally plastic single crystals under tensile loading. In a FCC single crystal, the asymptotic solutions were determined for a (001)[110] crack orientation. The crack tip stress state was shown in Figure 1.17. The evolution of the strain localisation bands under cyclic loading was analysed by [Flouriot *et al.*, 2003]. In order to verify the results, a 2D FE simulation was carried out in this work for a CT single crystal under plain-strain conditions after 10 cycles, as shown in 1.18. At a given distance from the crack tip, along a circular arc, the FE results correspond to the asymptotic RICE solutions. The 2D fatigue crack propagation simulations using microdamage theory in single crystals is developed by [Aslan and Forest, 2009]. However, the applications in 3D may be very time consuming.

5. Adaptive meshing techniques

An adaptive mesh refinement is a mesh type in which the element sizes conform to specific requirements. The techniques to generate and remesh appropriate 3D
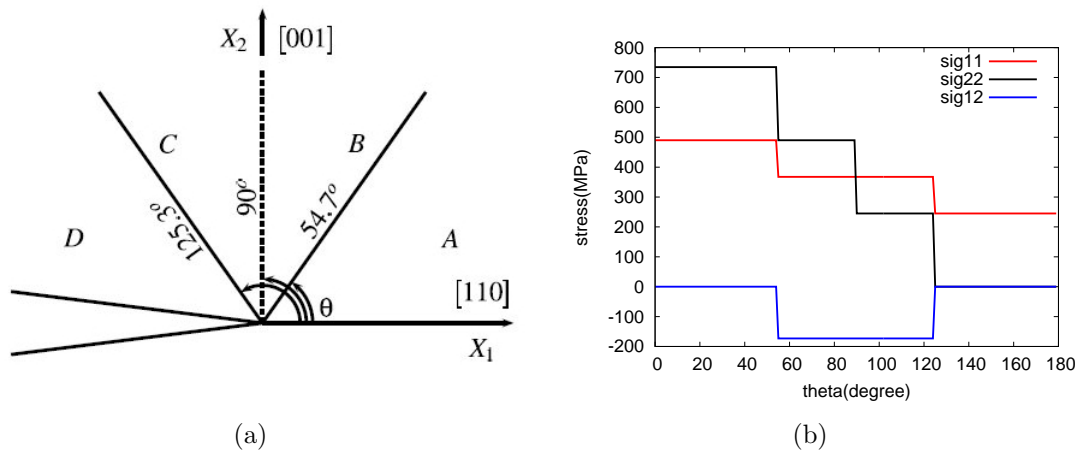
FIGURE 1.17: (a) Rice asymptotic solutions for a (001)[110] crack orientation in elastic-ideally plastic single crystals [Rice, 1987]. (b) Schematic representation of Rice asymptotic solutions for (001)[110] crack orientation, edited from [Flouriot *et al.*, 2003].

meshes is summarised in [George *et al.*, 2004]. A meshing algorithm is proposed by [Chiaruttini *et al.*, 2010] for inserting a crack surface in an uncracked mesh in 3D. This approach makes the FE simulation of crack propagation efficient and accurate with respect to the mesh with fixed element sizes. The detailed description of this method is presented in Chapter 3.

Conclusions

In this chapter, X-ray tomography characterisation techniques were presented. The mechanisms of fatigue in single and polycrystals were reviewed. Then, the different approaches of damage evolution laws were summarised. In particular, the Fatigue crack Initiation Parameters (FIPs) in a micromechanical approach were presented in detail. The recent developments in FE simulation of polycrystals and numerical techniques for crack propagation computation were also addressed. In order to simulate crack propagation in a 3D realistic polycrystal reconstructed from tomographic images, the adaptive meshing technique is selected in this work.

Conclusions

Les techniques de la caractérisation microstructure par la tomographie aux rayon X ont été rappelées dans ce chapitre. Ensuite, les mécanismes de déformation en fatigue dans les monocristaux et les polycristaux ont été revus. Les différentes
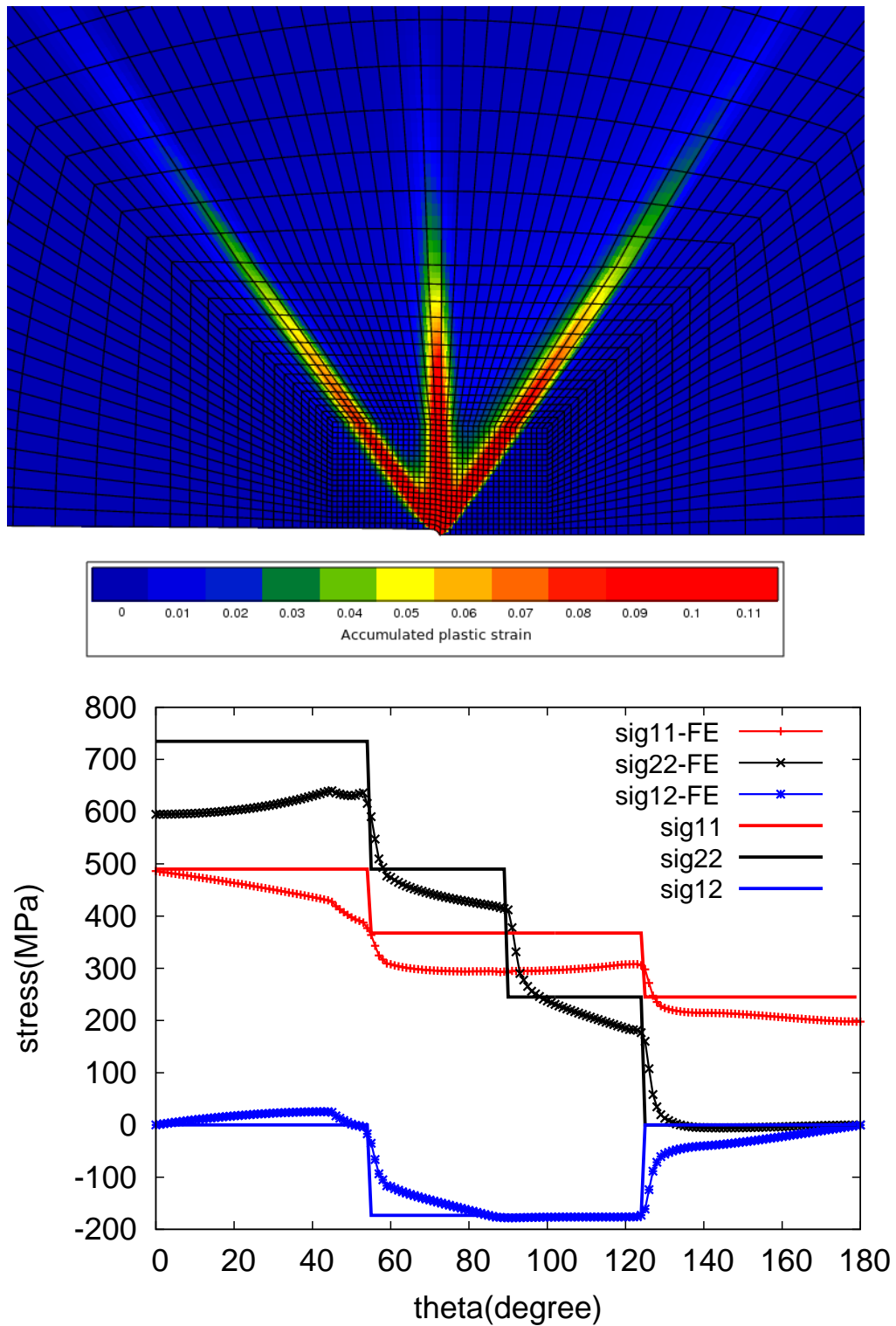
FIGURE 1.18: Simulation results of single crystal in a plain-strain field (FE) and the corresponding stress state in the near crack tip region.

approches de lois d'endommagement, en particulier les Parametres de Fissuration en Fatigue (FIPs) dans une approche micromécanique, ont été décrites en détail. Les récentes évolutions sur la simulation EF des polycristaux et les techniques numériques de propagation de fissure ont également été synthétisées. Finally, la technique de remaillage conforme a été sélectionnée dans ce travail afin de simuler la propagation de fissure en 3D dans un polycristal réalist reconstruit par les images tomographiques.

Chapter 2

Numerical Aspects of 3D CPFE Computation

In order to investigate the anisotropic elastic behaviour and to perform the FE simulation for crack propagation in the polycrystalline material imaged by DCT, a 3D microstructural FE mesh construction from the tomographic images and a crack insertion technique are introduced in this chapter. Two microstructural meshes corresponding to two different samples are created. The final cracked meshes contain millions of Degrees Of Freedom (DOF). Therefore, the parallel computation method is adapted for further elastic-plastic calculations.

Résumé

Afin d'étudier l'anisotropie de comportement élastique et la simulation de propagation de fissure courte dans un maillage polycristallin réalist, les techniques de reconstruction de maillage microstructural en 3D à partir des images tomographiques et d'insertion de fissure sont présentées dans ce chapitre. Deux maillages microstructuraux correspondants à deux éprouvettes différents sont créés. Le maillage pré-fissuré contient des millions de degrées de liberté. Le calcul en parallèle est donc nécessaire par la suite et qui est adapté aux calculs élasto-plastique.

2.1 3D mesh generation from tomographic images

The microstructure geometry determined from DCT is a 3D stack of labeled images, where each voxel label value corresponds to the number of the grain that it belongs to. These grain numbers are ordered according to decreasing grain volume. The construction of a FE mesh from the tomographic images is a crucial and non-trivial procedure in FE simulations. It consists of three main steps: surface mesh generation of the grain boundaries, simplification, and filling the surface mesh with tetrahedral volume elements. In the end a realistic 3D FE mesh of the polycrystalline sample based on tomographic images is obtained. A similar mesh reconstruction method is found in [Simonovski and Cizelj, 2011] but with different software. Recent progress with various 3D imaging techniques of polycrystalline microstructures triggered new software developments to handle these images. One can cite the open source DREAM3D software developed by [Groeber and Jackson, 2014] or commercial suite like Avizo [Avizo] or Simpleware [Simpleware].

The 3D grain boundary surface mesh is generated by the Avizo software in which the Multiple material Marching Cubes algorithm (MMC) [Wu and Sullivan, 2003] is applied to a segmented image to generate a triangulated surface mesh. The main steps of the MMC algorithm are as follows: first a regular grid of square pixels is overlaid to each layer of segmented tomographic images. Cubes are created from two adjacent slices, as shown in Figure 2.1(a). Therefore, the cube sizes are equal to 1 voxel. The label of the voxel of the tomographic image at which each vertex of the cube is located is assigned to that vertex. There can be up to eight different labels in each cube. For each edge connecting two vertices with different material labels, a boundary node is created at its midpoint. Then, boundary segments are created between these boundary nodes. Figure 2.1(b) shows an example with two different labels. If there are at least three different labels at one face of a cube, face center nodes and associated segments are created as shown in Figure 2.1(c). Next, the segments, whose sizes are smaller than 1 pixel, created previously are triangulated without introducing any other nodes or lines on the cube faces, see Figure 2.1(d), (e).

The surface mesh generated by MMC has stair-step shaped surfaces which do not represent the real surface curvature, see Figure 2.2(a). Surface smoothing is carried out by a Laplacian filter shifting the vertex of each element to the average
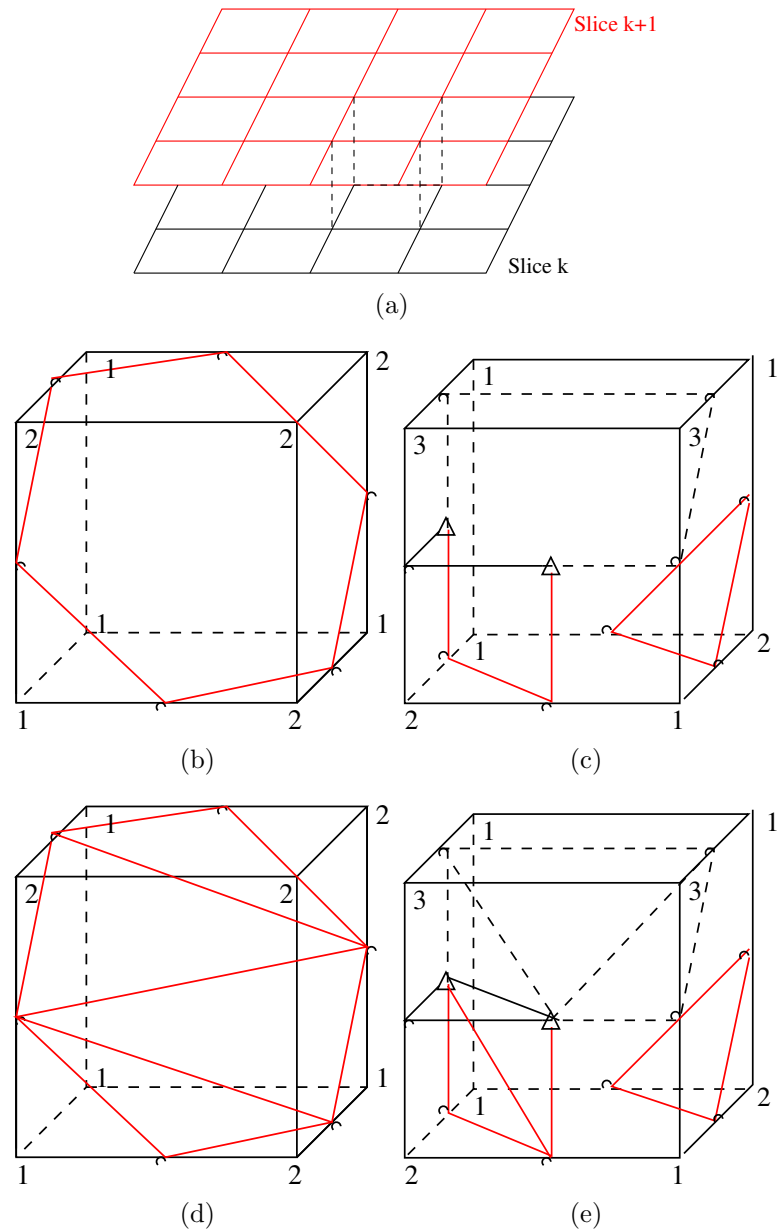
FIGURE 2.1: (a) Multiple material Marching cubes algorithm: regular grid overlays between slices k and $k+1$ of the tomographic image. Examples of boundary segments for two materials (b) and three materials (c). Red lines: interface between material 1 and 2, black lines: interface between material 2 and 3, dotted lines: interface between material 1 and 3. (d) Example of triangulation of segments for two materials. (e) Example of triangulation of segments for three materials.
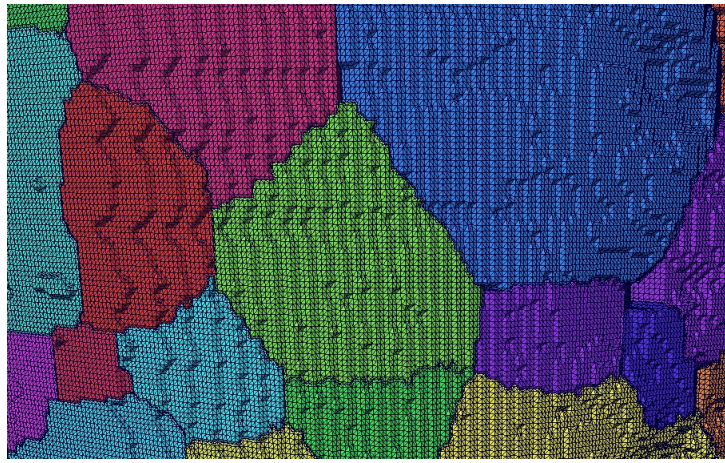
(a)
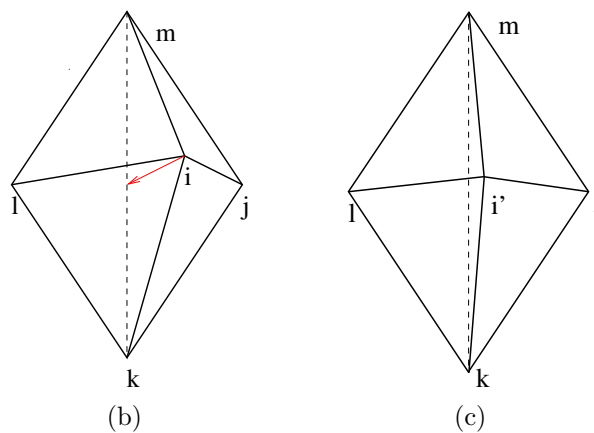
(b)   (c)

FIGURE 2.2: (a) Stair-step shaped surfaces generated by MMC, an example before surface smoothing (b) and after surface smoothing (c).

position of its neighbours. The new position of the vertex (x'_i) is described by

$$x'_i = x_i + \lambda(x_j + x_k + x_l + x_m + ...),\qquad(2.1)$$

with x_j, x_k, x_l, x_m the vertices nearby and λ a user-specified shifting coefficient. Figure 2.2 illustrates schematically an example before surface smoothing (b) and after surface smoothing (c). In Avizo, the quality of this step is controlled by the shifting coefficient λ. The surface smoothing procedure can be repeated several times successively to improve the surface smoothing.

The surface mesh created by this method contains millions of sub-voxel sized elements. From the point of view of FE computational time, a mesh simplification is required. Within the Avizo software, mesh coarsening is carried out using the decimation approach [Guéziec, 1997] by collapsing edges into vertices in a given
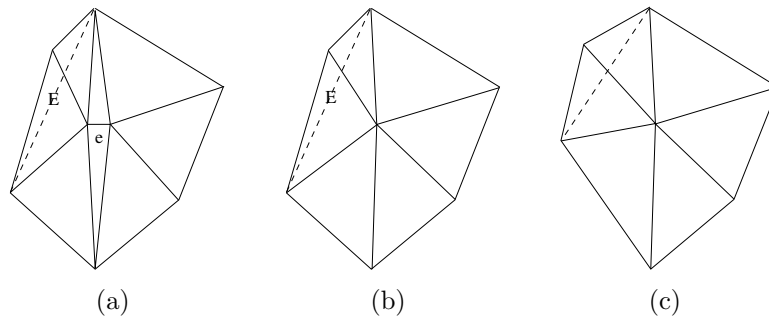
FIGURE 2.3: Example of surface mesh simplification: (a) initial surface mesh, (b) a small edge of length e is removed, (c) the edge length E is decreased.

range, which allows to preserve mesh topology, as shown in Figure 2.3. Minimum and maximum edge length can be specified. For instance, if the edge length e is lower than the given minimum edge length, this edge will be removed, see Figure 2.3(b). Also, if the edge length E exceeds the maximum allowed, then it will be reduced to the maximum edge length, see Figure 2.3(c). This process is performed until all edge lengths are inside the given range. An example of a grain boundary surface mesh generated from tomographic images after having removed 76% of the faces in this simplification step is shown in Figure 2.5, see also Table 2.1 for a comparison of the number of grains in the tomographic images and in the FE mesh after mesh simplification.

2.1.1 Volume mesh generation

Once the surface mesh of the grain boundaries is obtained, the volume mesh generator Ghs3d, developed by Inria and distributed by Distene [Ghs3d], was subsequently used to fill the surface. The volume mesh generation is of Delaunay type. A detailed introduction of this method is described in [George and Borouchaki, 1997]. In short, nodes, edges and faces are extracted from the triangular surface mesh. Based on the positions of these nodes, an enclosing box is created containing all the nodes of the surface mesh, as shown in Figure 2.4 (a). This box is meshed into five or six tetrahedrons, and some internal points are inserted in order to accelerate the following procedure. Then, each node of the surface mesh is inserted one by one into the box using the Delaunay kernel method and the edges and faces of the surface mesh are regenerated, see Figure 2.4 (b). After the elimination of external points, the tetrahedral grain boundaries mesh is created.

(a)   (b)   (c)
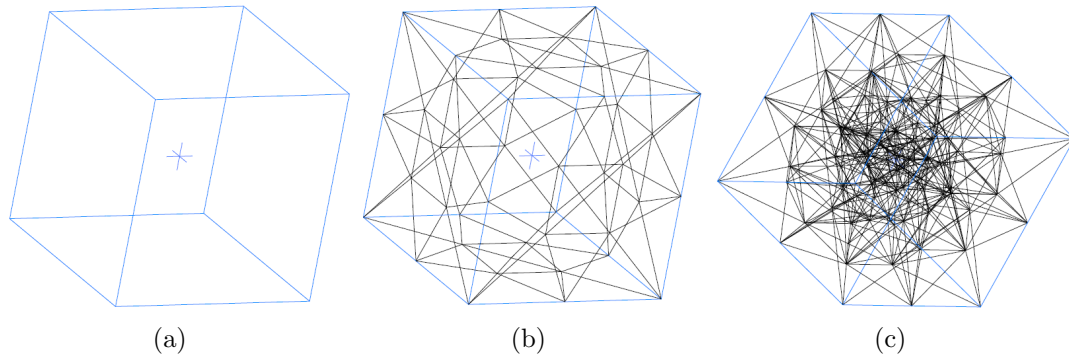
FIGURE 2.4: Volume mesh generation process from an enclosing box (a), regeneration of a tetrahedral surface mesh (b) and creation of a volume mesh (c) [Ghs3d].
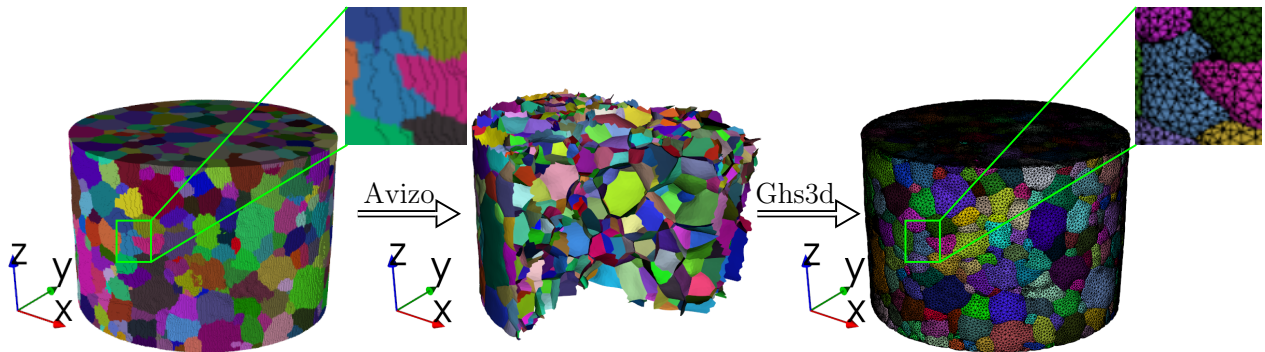
FIGURE 2.5: 3D mesh reconstruction procedure from tomographic images.

Afterwards, internal points are created by the barycenter method, see Figure 2.4 (c). Finally, a remeshing process is performed to improve the mesh quality.

The three stages of the meshing procedure are shown in Figure 2.5. The different colors were assigned randomly to different grains. In the zoomed region of Figure 2.5, it can be observed that the grain boundary of the blue grain is not convex. Furthermore, tiny grains were found inside big grains. These types of grain boundaries, which may influence the local mechanical response of polycrystals, cannot be produced by the Voronoi tesselation approach classically used to generate meshes of artificial polycrystalline aggregates.

The last step of mesh generation consists of relabelling the grains in order to have the same grain label as in the tomographic images, see Figure 2.6. This is necessary in order to assign the measured grain orientation to each grain of the FE mesh. This step is carried out as follows: the center of mass of each grain in

grains (tomographic images)	1397
grains (volume mesh)	1392
voxels (tomographic images)	36.5×10^6
triangles (surface mesh, after MMC)	10.5×10^6
triangles (surface mesh, after simplification)	2.50×10^6
tetrahedrons (volume mesh)	3.85×10^6

TABLE 2.1: Comparison of the number of grains in the tomographic images and in the mesh, as well as the number of triangles and tetrahedrons in the surface mesh and in the volume mesh.
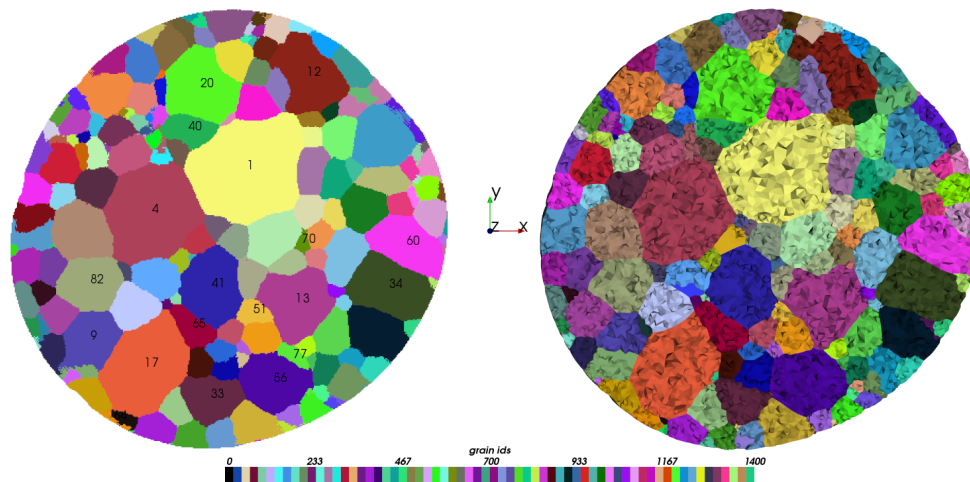
FIGURE 2.6: One horizontal slice of the tomographic images colored by grain number on the left and the corresponding slice of the FE mesh on the right.

the mesh $\overrightarrow{OG}$ is calculated from the centers of mass $\overrightarrow{OP_i}$ of its elements i:

$$\overrightarrow{OG} = \frac{1}{M} \sum^{i} m_i \overrightarrow{OP_i}, \tag{2.2}$$

with M: mass of the grain, $\overrightarrow{OG}$: position of the center of mass of the grain, m_i: mass of element i of the grain, $\overrightarrow{OP_i}$: position of the center of mass of element i of the grain. Then, for each $\overrightarrow{OG}$, the corresponding grain number is determined in the tomographic images and assigned to the FE mesh. This of course works only if the FE produced mesh is of high fidelity and if the grain shapes are not too tortuous, but it proved to work remarkably well for the materials investigated here.

Two volume meshes have been reconstructed, the first mesh with a cylindrical cross-section and the second mesh with a rather prismatic cross-section. The

cylinder mesh shown in Figure 2.5 contains 3.8 million tetrahedral elements, with the average element size of 10 μm. This mesh will be used to calculate the heterogeneous mechanical response under compression loading and to compare to the experimentally measured strain tensors using diffraction in Chapter 3. From the zoomed view of volume mesh in Figure 2.5, it can be observed that the non-convex grain boundary is reconstructed satisfactorily. The distributions of the grain diameter D, defined as

$$D = 2 \left(\frac{3V}{4\pi} \right)^{\frac{1}{3}} \tag{2.3}$$

with V the grain volume, were compared between the tomographic images and the reconstructed FE mesh, see Figure 2.7(a). The average grain size D is about 44 μm. The grain size distribution for the grains whose size is larger than 40 μm in the mesh is the same respect to the tomographic images. For several small grains, the differences of the distributions are less than 5 μm, due to the relative large element size in the mesh. The influence of these small differences to the FE computation of the elastic deformations will be smaller than the strain measurements precision, see Chapter 3.

The geometric precision in terms of grain boundary positions of the FE mesh reconstructed by this method is also analysed, as shown in Figure 2.9. In this figure, the white lines represent grain boundaries in the tomographic images. As for the grain boundaries in the mesh, a boundary zone of 1 μm thickness, which is the edge length of small elements, is analysed. The nodes on the grain boundaries in this volume are selected and projected on the slice of tomographic images. The distance in pixels between these two sets of grain boundaries is also calculated, see Figure 2.8. There are only a few points for which the difference is more than 3 pixels.

The prism mesh shown later in Figure 2.12 (a) contains 4.4 million tetrahedral elements and 384 grains. This mesh will be used to simulate crack propagation. The mean edge length is approximately 4 μm. A pre-notch will be inserted into this mesh in the next section. Figure 2.7 (b) shows only ten grains with diameters between 20 μm and 110 μm were distributed differently. The detailed analysis will be given in the next section.

Several limitations of this mesh construction process have appeared: i) the multi-material marching cubes algorithm generates many tiny triangles which need to be simplified, ii) it is difficult to control element size. Although the maximum and
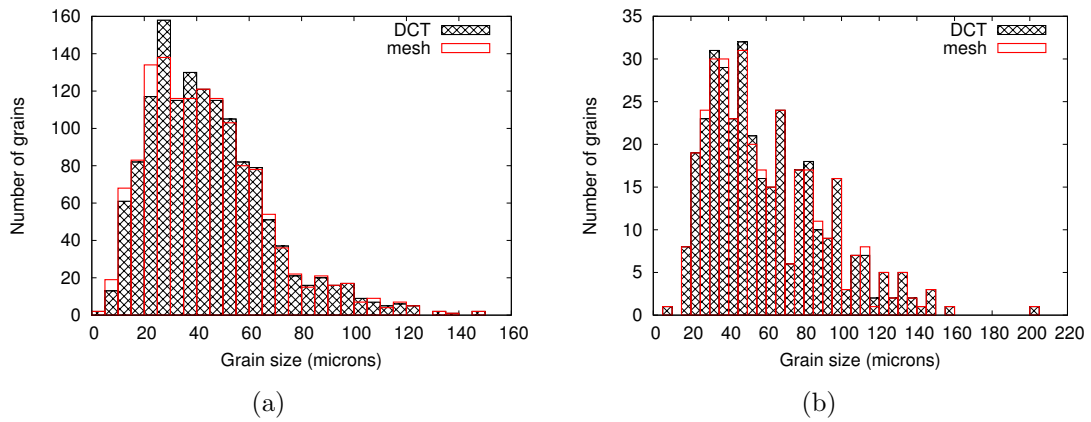
FIGURE 2.7: Grain diameter distribution in FE mesh and in DCT images for the cylinder mesh (a) and for the prism mesh (b).
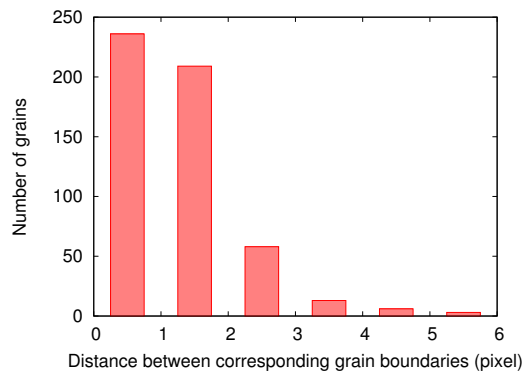
FIGURE 2.8: Distance between corresponding grain boundaries in the DCT images and the FE mesh.

the minimum edge lengths can be user-controlled during the simplification and the volume filling procedure, manual definition or modification of certain edge lengths seems to be impossible in Avizo and in Ghs3d. iii) The precision linked with the surface mesh simplification method does not support a high mesh simplification rate, which means that removing more than 95% of the vertices will generate large errors [Cignoni *et al.*, 1998].

2.2 3D crack insertion

A 141×26 μm notch has been machined by Focused-Ion Beam Machining at the middle of the sample in order to localise stress, to initiate and propagate a crack during the in-situ experiment. The position of the pre-notch is measured from the
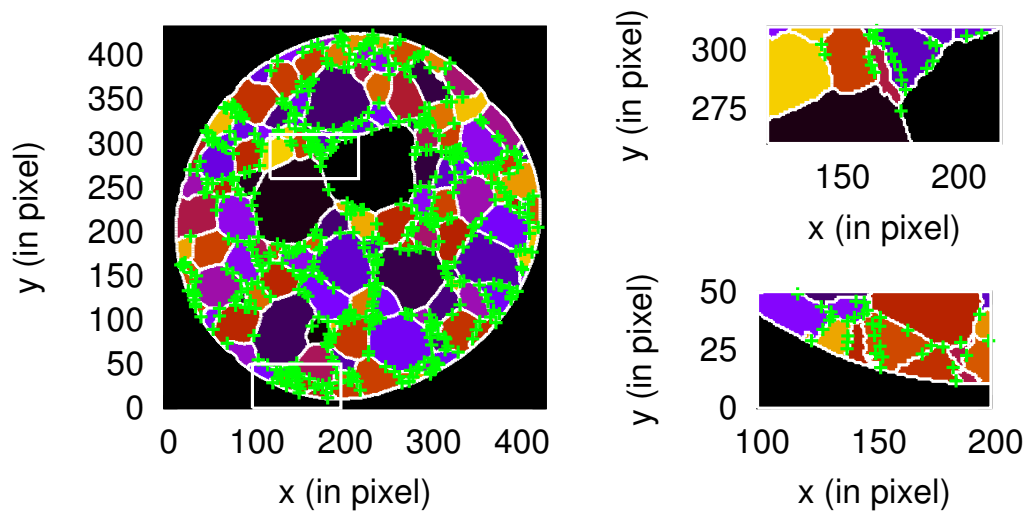
FIGURE 2.9: Comparison of grain boundaries in the tomographic images (white lines) and in the FE mesh (green crosses) on one horizontal slice of the sample. Two selected domains are magnified on the right.

PCT images. Based on this measurement, a surface mesh of the notch is created and then inserted automatically into the 3D FE polycrystalline mesh using Z-cracks, a module of the Z-set software suite. An assumption has been made that the thickness of the notch in the sample would be zero. It is indeed not realistic and the stress and strain fields in the elements at the notch tip will be unstable. However, the crack propagation method presented in Chapter 4 will be applied to the elements at a certain distance from the notch tip.

The main steps of crack insertion are as follows [Chiaruttini *et al.*, 2010, 2013]: first the crack surface is meshed independently. Then, the initial volume mesh is refined in the corresponding region of the crack, see Figure 2.11 (a) for a $100 \times 100 \times 100$ μm³ cubic single crystal which will be cut by a through-crack. The element size of the refined mesh is determined from a distance between a node in the initial volume mesh to the nearest node in the crack surface mesh. This process is carried out iteratively. Next, the adapted volume mesh is cut by the surface mesh of the crack using boolean operations as shown in Equation 2.4. Then it is remeshed several times using a combination of Yams, Meshadapt and Ghs3d to achieve the desired mesh refinement around the crack tip, as shown in Figure 2.11 (b),(c). For polycrystals, grain boundaries are preserved during the remeshing process and the grain numbers are reassigned to the cracked mesh after remeshing.
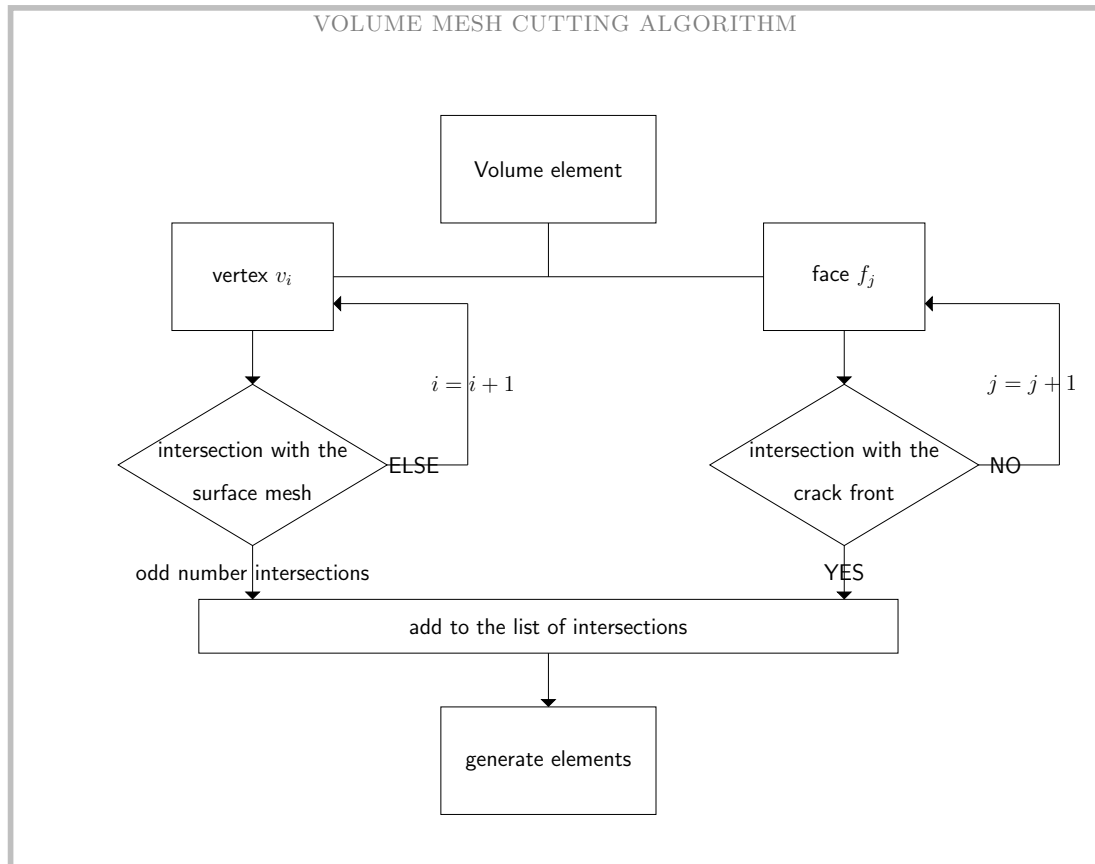
FIGURE 2.10: Volume mesh cutting algorithm.

The algorithm for cutting a volume mesh by a surface mesh is described in Figure 2.10. For each element of the initial volume mesh, the intersections of its vertices as well as its faces with the surface mesh are created. The convex elements of the cracked surface are generated from these intersections. Because the thickness of the crack is zero, these elements are duplicated to represent the upper and the lower side of the crack. In order to obtain an accurate crack shape, the elements of the initial surface mesh should be smaller than those of the volume mesh.

The remeshing process is carried out by defining the minimum edge length l near the crack front and a degradation factor h that specifies the maximum edge length variation between adjacent elements. For the minimum edge length l, h means that its neighbor element has a maximum edge length of $l^2 \times h$. In general, h is between 1.1 and 1.3. The edge length is calculated using a refinement function in Z-cracks, as follows:

$$f(x,y,z) = l + (x^2 + y^2 + z^2 > 3^2 \times l^2) \times (h^2 - 1) \times \sqrt{||x^2 + y^2 + z^2 - 3^2 \times l^2||}, \quad (2.4)$$

(a)

(b)

(c)
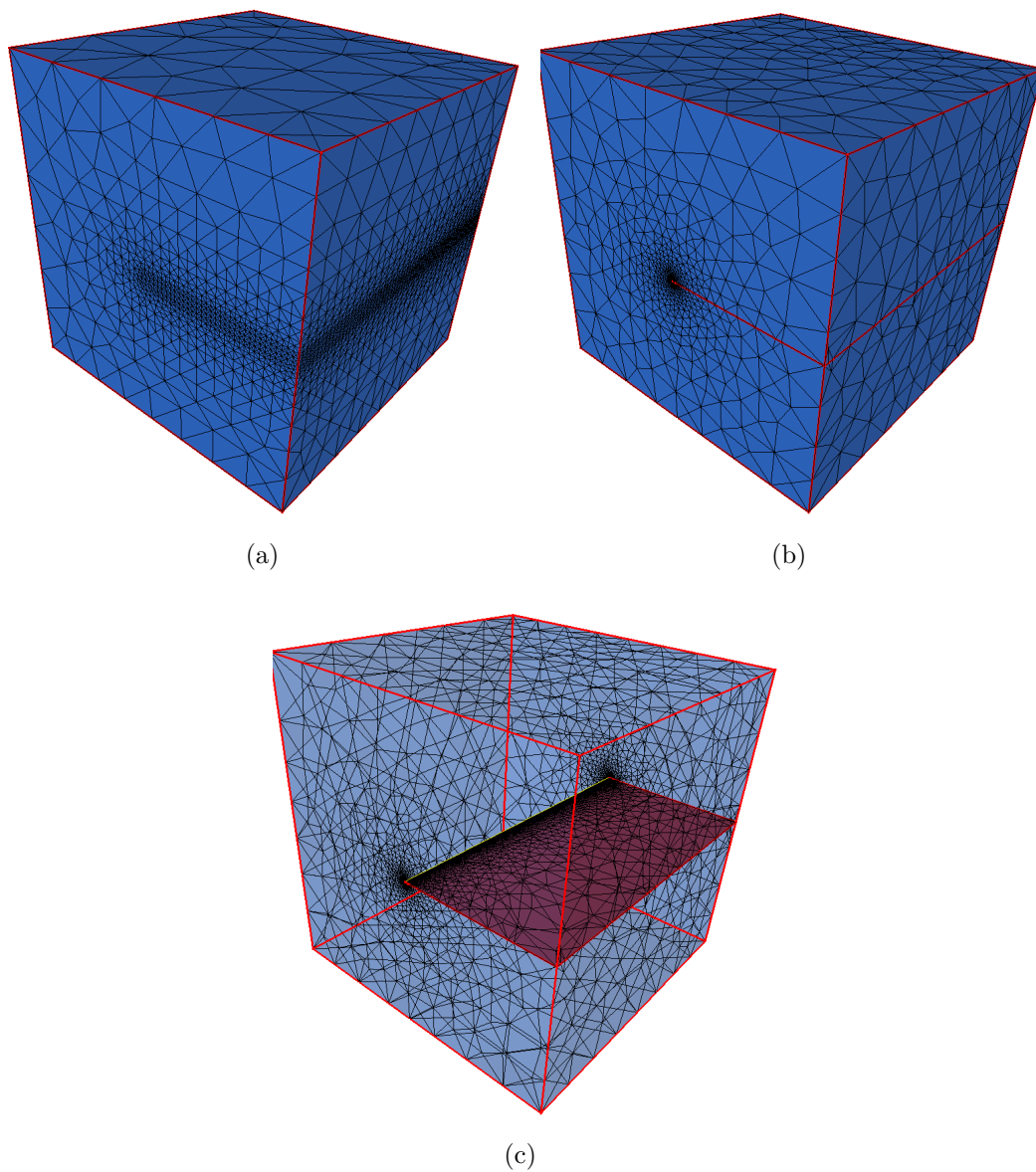
FIGURE 2.11: A $100 \times 100 \times 100 \ \mu m^3$ cubic single crystal cut by a through-crack (a) the refined volume mesh before cutting (b) final cracked volume mesh with a through crack, (c) a view of the crack with inside the volume, where only the element traces at the surfaces are shown. The minimum element size near the crack front is $0.1 \ \mu m$ and the degradation factor h is 1.1.

with x, y and z the coordinates of the elements. The boolean term $x^2 + y^2 + z^2 > 3^2 \times l^2$ specifies which element should be refined, with 3 the number of the minimum size element layer.

Figure 2.12 (a) shows the 3D microstructural mesh reconstructed from tomographic images without including the notch. It contains 357 grains and 4 469 307 elements. Remeshing this huge mesh requires large amounts of computer

(a)   (b)

(c)

(d)
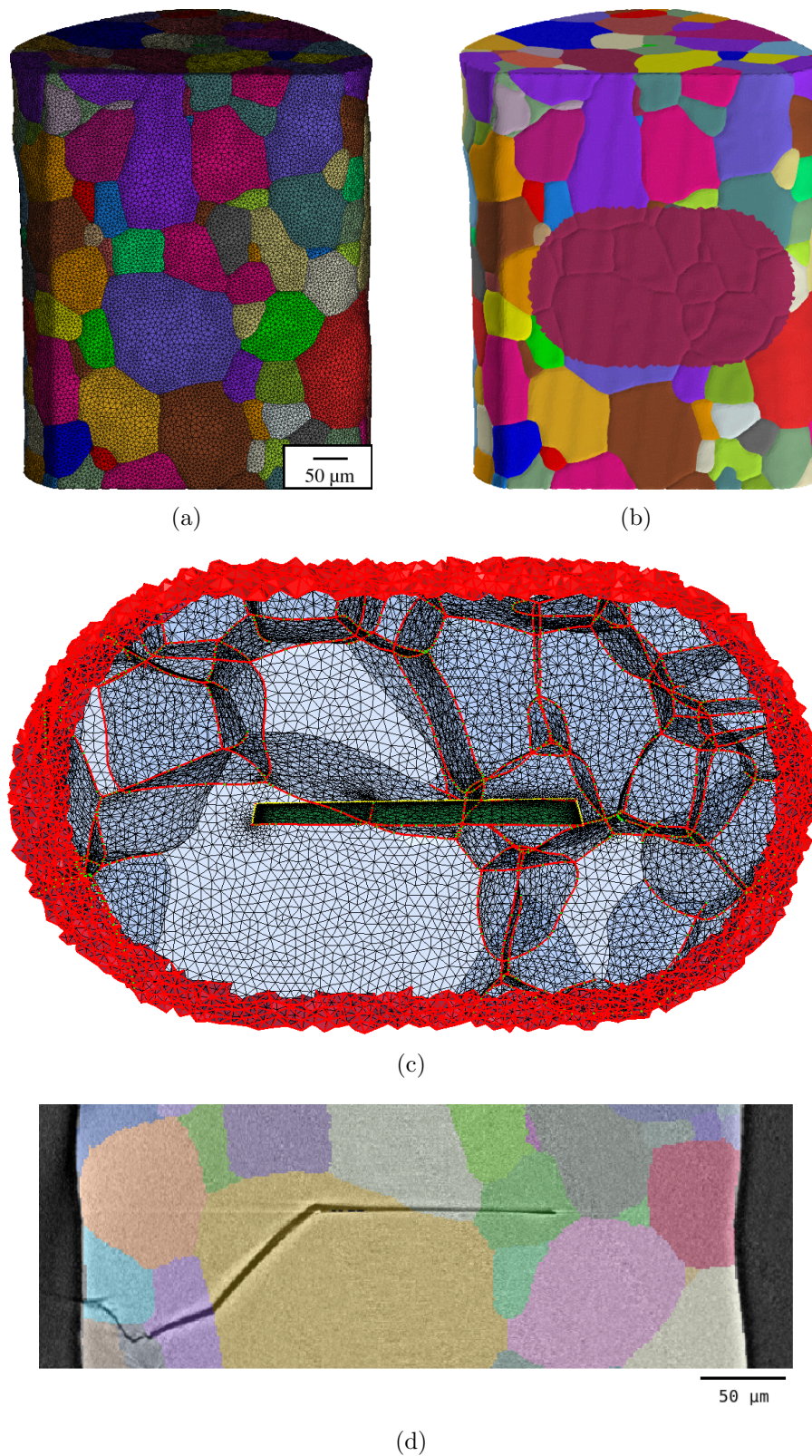
FIGURE 2.12: (a) The polycrystal mesh reconstructed from the tomographic images. (b) A region of 100 μm around the notch is extracted, represented in red. (c) A 3D view of the remeshed region with the notch. (d) Composite of DCT and PCT images of the sample surface containing the notch and the propagated crack.

(a)

(b)
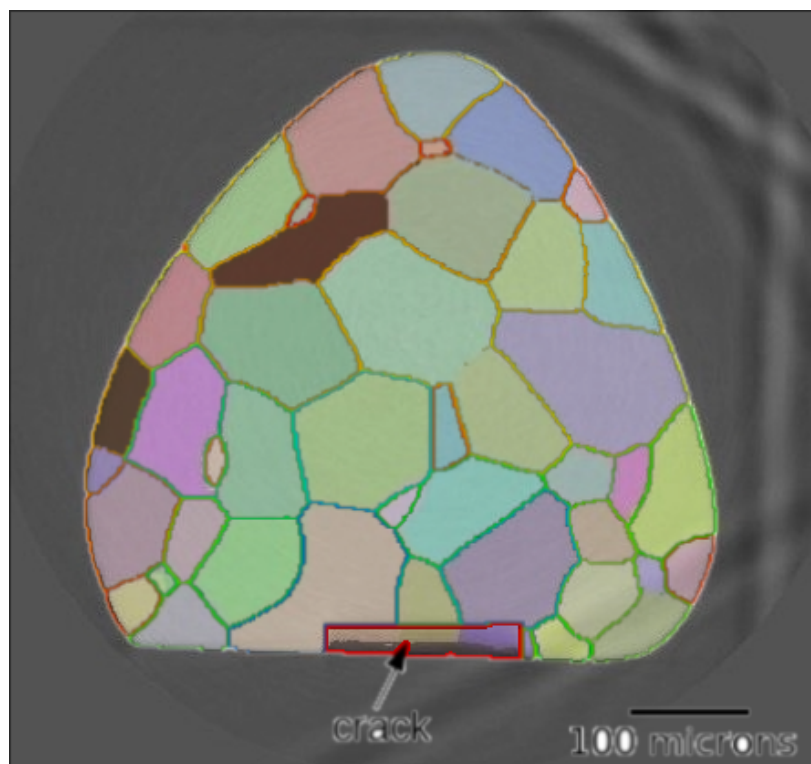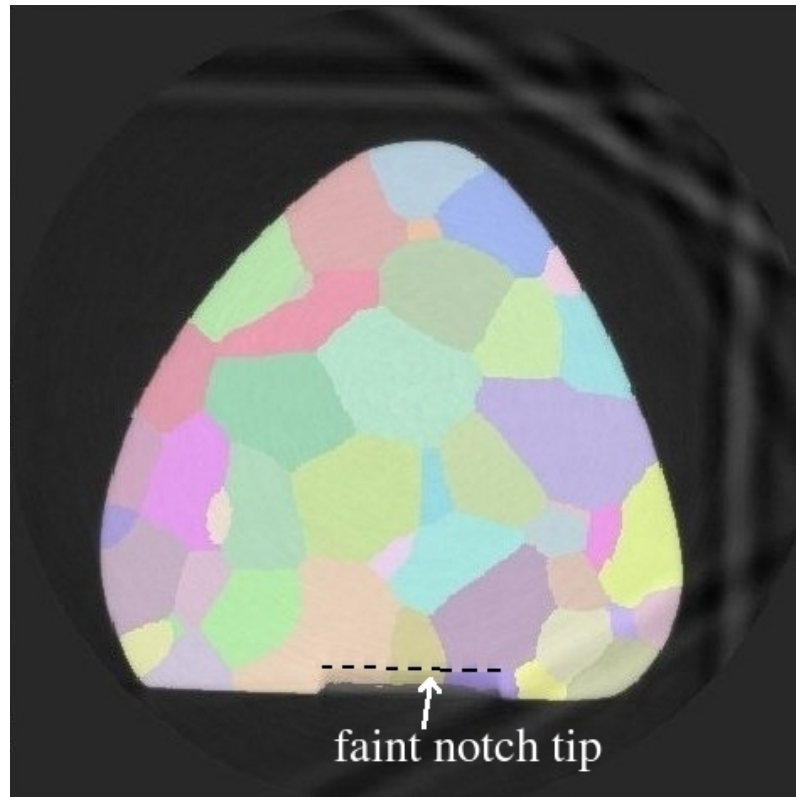
FIGURE 2.13: Top view of the pre-notch in (a) absorption image obtained by the DCT experiment overlapping with the grain map, (b) FE mesh overlapping with the absorption image.

memory and time. Thus, a region of 100 μm radius around the notch has been extracted, as shown in Figure 2.12 (b). The topology of elements at the boundary of this region is preserved during remeshing in order to assemble with the rest of volume mesh after remeshing.

Figure 2.12 (c) shows a 3D view of the crack region after remeshing. It contains 5 million elements, and the minimum element size at the notch tip is 1 μm. The rectangular notch cuts across three grains at the sample surface. The experimental crack at the sample surface is shown in Figure 2.12 (d), in which the notch is observed as a horizontal line.

The position of the two crack-tip points of the experimental notch at the sample surface is measured from the absorption image, as shown in Figure 2.13 (a). Their coordinates in pixels are (174, 63, 187) and (276, 63, 187) respectively. The pixel size is 1.4 μm. The other two vertices inside the volume are calculated from the crack dimensions due to the inaccurate image aquisition. The precison of this measurement is 1.4 μm. Figure 2.13 (b) shows a top view of the notch of the absorption image overlapping with the same view of the FE mesh. The coordinates of the crack-tip points in FE mesh in μm are (243.6, 88.2 262.0) and (385.0 88.0 262.0). Therefore, the precision of the crack insertion that is considered as the difference of the crack tip coordinates is less than 1 μm that is the minimum element size at the notch tip.

Several main advantages of this crack insertion method can be highlighted: First, the ease of insertion complex shape of crack in a given FE volume mesh. Second, by extracting a region near the crack it can deal effeciently with large FE meshes featuring millions of elements. Third, its precision can be adjusted by the initial element size of crack surface mesh and the minimum element size in the remeshing process. With the technique of adaptive remeshing, the computation time can be reduced significantly.

2.3   Parallel computing

The heterogeneous stress and strain fields inside a polycrystal and their evolution can be calculated by FE with a realistic mesh of the 3D microstructure and by using crystal plasticity constitutive laws. However, this approach becomes very

time consuming for large meshes and complex loading paths. Therefore, the calculations have been accelerated by parallelisation through a domain decomposition method. An example of simulations of tensile loading with the notched realistic microstructural mesh reconstructed in the previous section is discussed in the following. All FE calculations are carried out with the FE software Z-set, jointly developed by *Mines ParisTech* and *ONERA* [Z-set].

The polycrystalline mesh used in this section corresponds to a near β-titanium alloy VST55531 studied in more details later on (see Section 3.2). There for demonstration purpose, a simplified crystal plasticity behaviour using the 12 $\{110\}\langle111\rangle$ slip systems of the BCC crystal structure is adopted. This material is assumed to be anisotropic elastic up to the elastic limit and then perfectly plastic. The small strain tensor $\underset{\sim}{\varepsilon}$ is partitioned into an elastic part $\underset{\sim}{\varepsilon}^e$ and a plastic part $\underset{\sim}{\varepsilon}^p$ according to

$$\underset{\sim}{\varepsilon} = \underset{\sim}{\varepsilon}^e + \underset{\sim}{\varepsilon}^p. \tag{2.5}$$

Linear elasticity is described by Hooke's law, with $\underset{\approx}{C}$ the four-order tensor and $\underset{\sim}{\sigma}$ the Cauchy stress

$$\underset{\sim}{\sigma} = \underset{\approx}{C} : \underset{\sim}{\varepsilon}^e, \tag{2.6}$$

with $C_{1111} = 134$ GPa, $C_{1122} = 110$ GPa and $C_{2323} = 55$ GPa [Petry *et al.*, 1991]. The plastic strain is the result of the possible activation of 12 $\langle111\rangle\{110\}$ slip systems according to

$$\underset{\sim}{\dot{\varepsilon}}^p = \sum_{s=1}^{12} \dot{\gamma}^s \underset{\sim}{m}^s, \tag{2.7}$$

where $\underset{\sim}{m}^s$ is the orientation tensor defined by the slip plane $\underline{n}^s$ and the slip direction $\underline{l}^s$ in each system s

$$\underset{\sim}{m}^s = \frac{1}{2}\left(\underline{n}^s \otimes \underline{l}^s + \underline{l}^s \otimes \underline{n}^s\right), \tag{2.8}$$

and $\dot{\gamma}^s$ is the slip rate defined by a power law

$$\dot{\gamma}^s = sign(\tau^s) \left\langle \frac{|\tau^s| - \tau_0}{K} \right\rangle^n, \tag{2.9}$$

where K and n are Norton's parameters. In this study, the $\langle111\rangle\{112\}$ and $\langle111\rangle\{123\}$ slip systems are neglected. $\tau_0 = 100$ MPa is the critical resolved shear stress and τ^s is the resolved shear stress in the form of

$$\tau^s = \underset{\sim}{\sigma} : \underset{\sim}{m}^s. \tag{2.10}$$

In the next section, the computing time and the stress state around the notch are compared in order to assess the speedup by parallelisation. The simulations are carried out on a computing cluster using 25 nodes each with 256 Gb memory. Each node has 4 processors with 8 cores.

2.3.1 Parallel and multithreaded computations

First, parallel computations by domain decomposition are compared with its sequential, i.e. non-decomposed but multithreaded counterpart. Parallel computing consists of decomposing a large problem into smaller domains which are then treated simultaneously on several CPUs. This becomes even necessary when the memory required for the calculation exceeds the capacity of one machine. The computing time and the precision of parallel computations depend on the number of sub-problems.

The mesh partitioning is carried out by the METIS software [Karypis and Kumar, 1998] based on multilevel graph partitioning. For a given number of domains, it seeks to minimise the number of mesh edges at the domain boundaries while at the same time keeping the number of elements inside the different domains the same. This is important because the computing time depends (among other factors) on the size of the largest sub-domain. Figure 2.14 (a) shows a pre-notched microstructural mesh of polycrystalline materials with 32 sub-domains. It can be observed that the size of subdomains in the vicinity of the notch is smaller than near the top or the bottom surface, since the elements around the notch are much smaller than elsewhere.

After the mesh partitioning, the simulations are performed by FETI (Finite Element Tearing and Interconnecting) [Farhat and Roux, 1991]. At each iteration, the local sub-problems are solved independently and simultaneously. At the boundary nodes, Lagrange multipliers are introduced to enforce continuity of the displacements. Next, a parallel conjugate projected gradient algorithm is applied to solve Lagrange multipliers that represents the interaction forces at the boundary.

MUMPS (MUltifrontal Massively Parallel sparse direct Solver) is used for both sequential and parallel computations [Amestoy *et al.*, 2001]. It can solve both symmetric and non-symmetric problems and detect rigid body motions. Compared to the sparse-direct solver as present in Z-set, MUMPS is very efficient for large

(a)   (b)
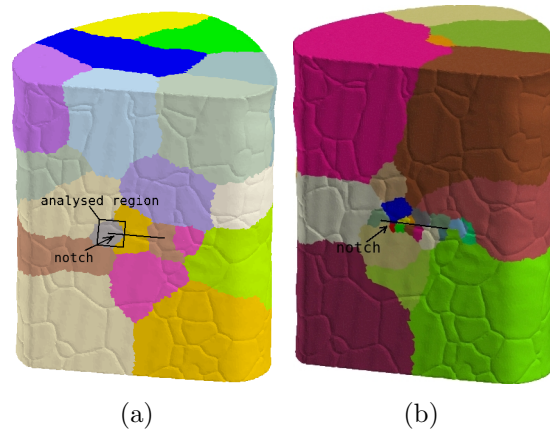
FIGURE 2.14: Domain partitioning into 32 sub-domains of (a) the notched linear mesh, (b) quadratic elements near the notch and linear elements in far region.

problems. However, it is not very robust for highly heterogeneous problems or contact problems [Guèye *et al.*, 2011]. For the present work, the Z-Set MUMPS interface has been modified slightly so that it can be used in conjunction with FETI, see Appendix A.

Comparisons between a parallel and a sequential multithreaded simulation are given in Table 2.2. The meshes and the boundary conditions in both simulations are the same. The applied vertical displacement U3 = 1 μm at the top surface correponds to a mean strain ε_{33} of 0.19%. Some Degrees of Freedom (DOF) were also blocked in the horizontal direction in order to prevent rigid body motions, but this is not indicated in Table 2.2. Three variables are analysed: the strain component *eto*33 (ε_{33}), the stress component *sig*33 (σ_{33}) and the cumulative slip *octgeq* of the 12 {111} slip systems. For the latter two quantities, the results are plotted along a circular path around the notch, of radius 3 μm, at intervals of 1°. The analysed region is located around the left side of notch at the front surface of the sample, see Figure 2.14. The comparisons in Table 2.2 show that the stress and strain localisations can be reproduced by the parallel computations, and that the computing time has been reduced dramatically, from 43 hours to 9 hours.

2.3.2 Linear versus quadratic elements

The accuracy of FE simulations depends also on the element order that is associated to the integration scheme. Comparisons between linear elements and

computation	sequential 32 threads	parallel 32 domains
element	linear	linear
D.O.F.	2.7 million	2.7 million
increments	25	25
B.C.	U3 = 1 μm (top) U3 = 0 μm (bottom)	U3 = 1 μm (top) U3 = 0 μm (bottom)
eto33		
octgeq		
sig33		
Time	**43 h**	**9 h**
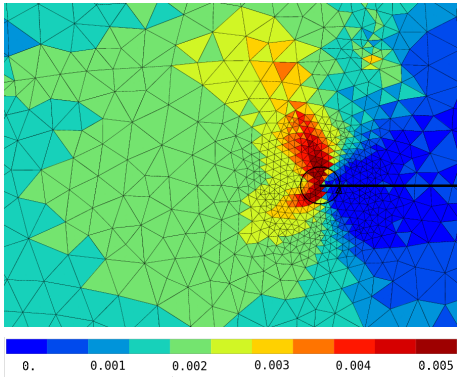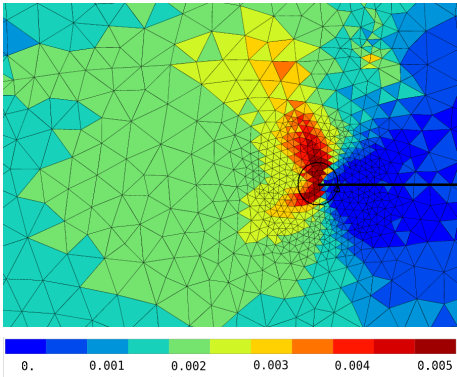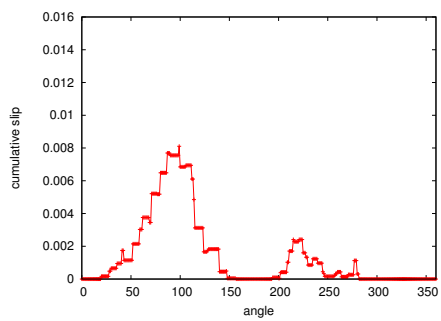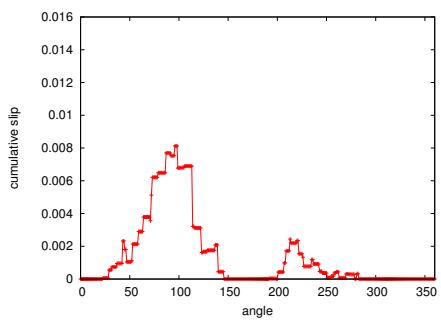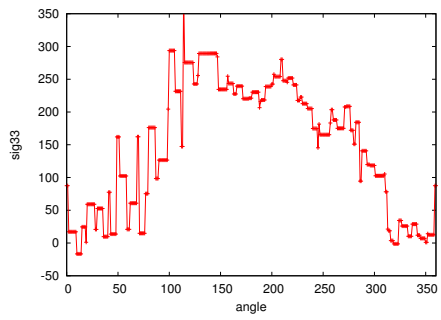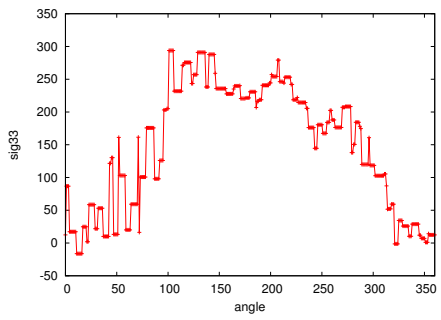
TABLE 2.2: Comparisons of simulations with domain decomposition ("parallel") and multithreading ("sequential").

quadratic elements are shown in Table 2.3. Again, the problems are divided into 32 subdomains. The linear element computation contains 2.7 million DOF. The quadratic element computation contains 21.7 million DOF, which is *impossible* to calculate on a single node of our current cluster with a multithreaded sequential computation because of its memory requirements. In Table 2.3, the two figures of the strain field *eto*33 show the differences between the simulations with linear and quadratic elements. With the same boundary conditions, the strain localisation of quadratic elements is more apparent compared to linear elements. The fact using a perfectly plastic material makes the strain localisation bands form very locally. The strain values change progressively from the notch tip to other regions. However, on the map of linear elements, a numerical locking problem can be observed in some regions. Concerning the cumulative slip, the maximum value for quadratic elements is twice as high as for the linear elements, and the curve is much smoother. This study indicates that several issues remain in the simulations with linear elements. The parallel computation makes the quadratic elements calculation *possible*, but at 49 h it is very costly.

2.3.3 An alternative solution

Because of the time-consuming nature of the computation with quadratic elements and the inaccuracy of the linear elements simulations, an alternative solution has been developed. Since only the results around the notch tip are of interest for the crack propagation, quadratic elements are used in the region around the notch and linear elements elsewhere. This solution is first validated by a multithreaded computation and then applied to parallel computation with domain decomposition.

When combining linear and quadratic elements in the same mesh, special care has to be taken at the interfaces between them. A mesh edge shared between a linear and a quadratic element contains three nodes attached to the quadratic element of which only two are attached to the linear element. In order to enforce continuity, a Multi-Point Constraint (MPC) is applied which imposes its displacement at the unshared middle node (the one attached to the quadratic element only). This displacement is linearly interpolated between both end nodes of the mesh edge.

Table 2.4 shows the results of multithreaded computation with combination of linear and quadratic elements compared to parallel computation with quadratic

computation	parallel 32 domains	parallel 32 domains
element	linear	quadratic
D.O.F.	2.7 million	21.7 million
increments	25	25
B.C.	U3 = 1 μm (top) U3 = 0 μm (bottom)	U3 = 1 μm (top) U3 = 0 μm (bottom)
eto33		
octgeq		
sig33		
Time	**9 h**	**49 h**
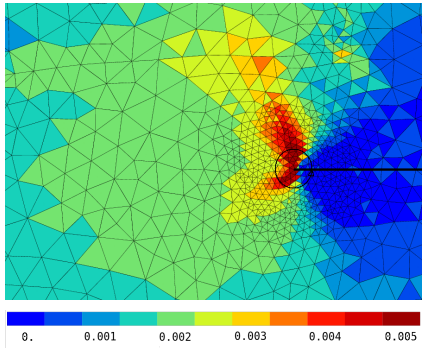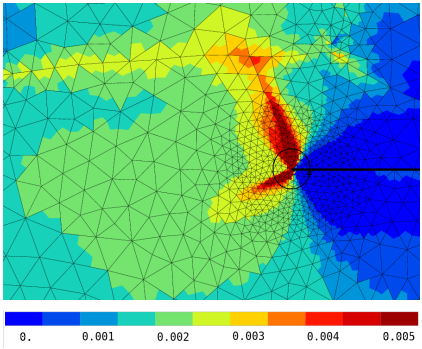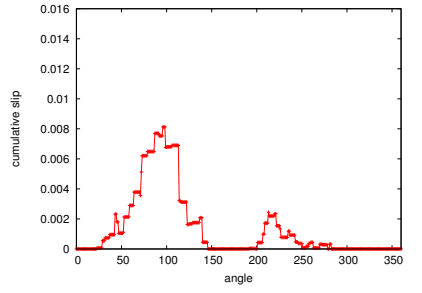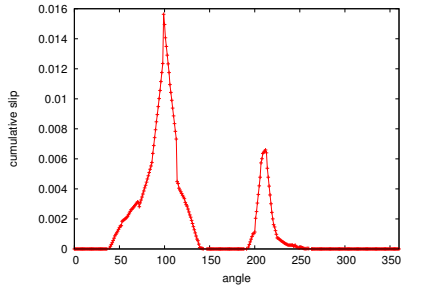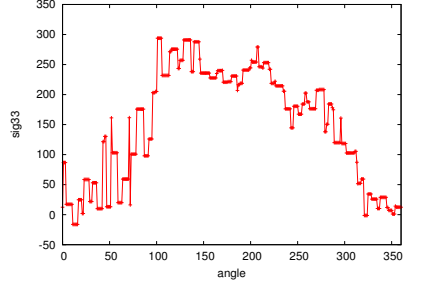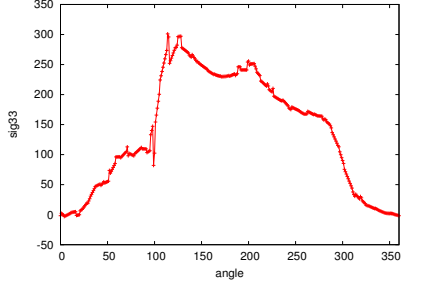
TABLE 2.3: Comparisons of the parallel computations with linear and quadratic elements.

computation	sequential 32 threads	parallel 32 domains
element	linear & quadratic	linear & quadratic
D.O.F.	5 million	5 million
increments	25	25
B.C.	U3 = 1 µm (top) U3 = 0 µm (bottom)	U3 = 1 µm (top) U3 = 0 µm (bottom)
eto33		
octgeq		
sig33		
Time	**62 h**	**11 h**
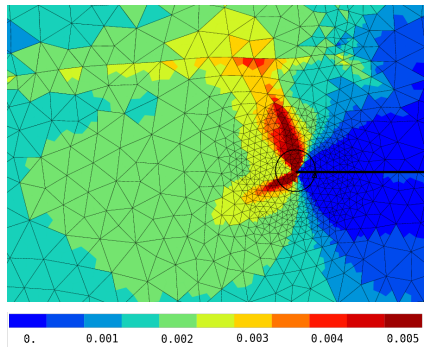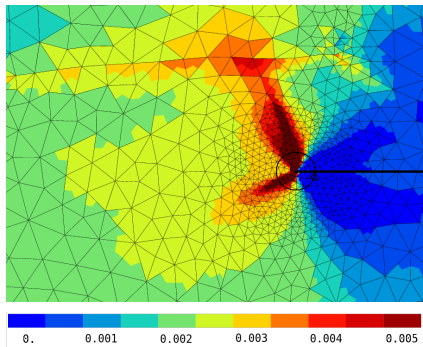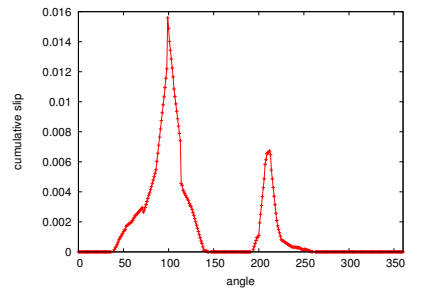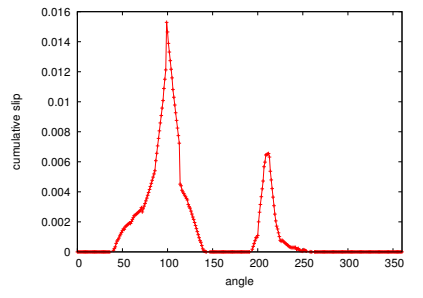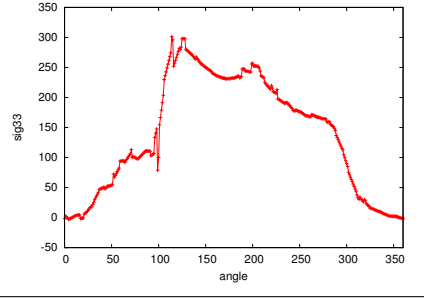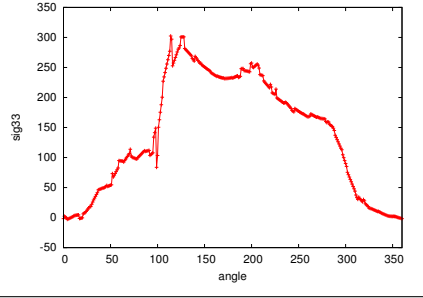
TABLE 2.4: A parallel computation compared to a multithreaded sequential computation with quadratic elements near the notch and linear elements in other regions.

elements. It can be observed that the stress and strain fields around the notch correspond. Also the solutions at the interface between linear and quadratic elements no anomalies could be observed.

The computing time could be reduced significantly by using parallel computation with both linear and quadratic elements. However, one of the difficulties for parallel computation of the combined linear and quadratic mesh is the domain partitioning. Having the same number of elements in each subdomain is not acceptable, because the quadratic elements have more DOF and the parallel computing time depends on the largest number of DOF of the subdomains. Therefore, a new option `*weight_by_node` has been added to the METIS mesh splitter to assign a weight factor according to the number of nodes of each element in order to improve the distribution of the number of DOFs between domains. Figure 2.14 (b) shows the domain partitioning into 32 domains with linear and quadratic elements with the weight parameter. The input file for the mesher used in this case is given in Appendix A. Compared to Figure 2.14 (a), the size of subdomains around the notch with quadratic elements is much smaller than the size of subdomains with linear elements in other regions.

Another problem is that the unshared middle node MPC cannot be applied directly in parallel computations. Specifically, when the boundary between linear and quadratic elements coincides at least partly with a domain boundary, the DOF associated to the unshared node of the quadratic element should not be taken into account when enforcing continuity across the boundary. Also, the detection of the unshared middle nodes is very complex in parallel, where each domain does not know the elements on the outside of its boundary. These have been fixed for this project: the detection of the unshared middle nodes now takes place before the domain decomposition (a new mesher `**unshared_middle_nodes` has been created to that effect; its syntax is given in the Appendix) and the MPC has been adapted to use this information inside each domain. This has been validated on a test calculation on a very small polycrystal, and its validation on the mesh of Figure 2.14 (b) is shown in Table 2.4. Finally, the computing time has been reduced significantly from 62 h for the multithreaded computation to 11 h for the parallel computation.

Conclusions

Two microstructural meshes were reconstructed from the tomographic images. The cylindrical mesh will be used to study the anisotropic elastic behaviour in Chapter 3. A rectangular notch was inserted into the prismatic polycrystalline mesh. It will be used to simulate crack propagation in Chapter 5. In the present chapter, a monotonic tensile loading was simulated. Multithreaded and parallel computations are carried out with both linear and quadratic elements. The comparisons show the relevant results of parallel computations using quadratic elements. The computation using quadratic elements around the notch and linear elements in other regions is validated by multithreaded computation and parallel computation. This approach will be used to simulate crack propagation in Chapter 5.

Conclusions

Deux maillages microstructuraux ont été reconstruits à partir des images tomographiques. Le maillage cylindrique servira à étudier l'anisotropie de déformation élastique dans Chapitre 3. Une préfissure rectangulaire a été insérée dans le maillage prismatique afin de controller l'endroit de fissuration. La simulation de propagation de fissure sera réalisée en utilisant ce maillage pré-fissurée dans Chapitre 5. Dans ce chapitre, un essai de traction a été simulé par les calculs en multithread et en parallèle avec les éléments linéaires et quadratiques. Les résultats de calculs en multithread et en parallèle sont cohérents. Afin d'optimiser le temps et la précision de calculs, les éléments autour de fissure sont quadratiques et les éléments linéaire dans les autres zones. Cette approch sera utilisée pour la simulation de propagation de fissure dans Chapitre 5.

Chapter 3

Mechanical behaviour of pure titanium and VST55531

Two materials are studied in this work: a commercially pure α-titanium and a near β-titanium alloy VST55531. The first part (Section 3.1) of this chapter is dedicated to the elastic behaviour of a pure titanium sample under compression loading. The elasto-visco-plastic behaviour of plain VST55531 samples under tension-compression loading is studied in Section 3.2. In order to apply the real orientation of grains measured by the DCT in the form of Rodrigues vectors into the CPFE calculations, the conversion to Euler angles, especially with the Euler convention in the Z-set code, is described. It is then validated by comparing the average strain tensors of each grain between DCT measurement and FE simulation in the pure titanium sample. Next, the tension-compression tests using the VST55531 sample are carried out. The elasto-visco-plastic material parameters of the crystal plasticity model are identified. These parameters will be used in the crack propagation simulations in Chapter 5.

Résumé

Deux matériaux sont étudiés dans ce chapitre: α titane pure et alliage titane quasi β VST55531. La première partie (Section 3.1) est consacrée au comportement élastique d'une éprouvette en titane pure soumise à un chargement compression.

Le comportement élasto-visco-plastique d'une éprouvette en VST55531 en chargement cyclique est étudié dans Section 3.2. Afin d'appliquer l'orientation réelle de grains mesurée par DCT sous forme de vecteurs Rodrigues, la conversion à l'angles d'Euler du code Z-set est décrite. Cette conversion est validée par une comparaison de tenseurs de déformation élastique moyennés aux grains entre DCT et simulation. Ensuite, les paramètres de matériau VST55531 du modèle plasticité cristalline ont été identifiés. Ces paramètres sera utilisés pour la simulation de propagation de fissure dans Chapitre 5.

3.1 Elastic behavior of pure titanium

The pure α-titanium has a relatively low atomic number of 22 and an appropriate mass density favourable for tomographic acquisition. Typically at energy $E = 40$ keV, the mass attenuation coefficient is 2.214 cm^2/g. Combined with a mass density of $\rho = 4.54$ g/cm^3, the Beer-Lambert law in Equation 1.2 gives a transmission of 36% through a 1 mm sample and 54% through a 0.6 mm sample. Moreover, its elastic constants are well-known. It is also possible to obtain a well-recrystallised microstructure with a grain size of around 50 µm. Therefore, it has been selected to investigate the anisotropic elastic behaviour both experimentally and numerically.

3.1.1 Anisotropic elasticity of pure titanium

Pure α-titanium has a Hexagonal Close-Packed (HCP) crystal structure with a transversely isotropic symmetry. The lattice parameters are $a = 0.295$ nm and $c = 0.468$ nm [Lutjering and Williams, 2007], as defined in Figure 3.1 (a). The ratio of c/a is 1.578. The elastic constants (in MPa) in Voigt's notation for pure

titanium are the following [Simmons and Wang, 1971]:

$$
\underset{\approx}{C} =
\begin{pmatrix}
162000 & 92000 & 69000 & 0 & 0 & 0 \\
92000 & 162000 & 69000 & 0 & 0 & 0 \\
69000 & 69000 & 180000 & 0 & 0 & 0 \\
0 & 0 & 0 & 46700 & 0 & 0 \\
0 & 0 & 0 & 0 & 46700 & 0 \\
0 & 0 & 0 & 0 & 0 & 35000
\end{pmatrix}.
\tag{3.1}
$$

The tensor of elasticity is anisotropic, with the anisotropy factors as follows:

$$
A = \frac{s_{11}}{s_{33}} = 1.39,
\tag{3.2}
$$

$$
B = \frac{2(s_{11} - s_{13})}{s_{44}} = 1.07,
\tag{3.3}
$$

where s_{11}, s_{13}, s_{33} and s_{44} are the components of the compliance tensor $\underset{\approx}{S}$. The relationship between the components $C_{ij}(i, j = 1, 2, .., 6)$ of $\underset{\approx}{C}$ and $\underset{\approx}{S}$ for the hexagonal symmetry are given in [Cazzani and Rovati, 2003] and recalled as follows:

$$
s_{11} = \frac{-c_{13}^2 + c_{11}c_{33}}{(c_{11} - c_{12})(-2c_{13}^2 + (c_{11} + c_{12})c_{33})},
$$

$$
s_{12} = \frac{c_{13}^2 - c_{12}c_{33}}{(c_{11} - c_{12})(-2c_{13}^2 + (c_{11} + c_{12})c_{33})},
$$

$$
s_{13} = \frac{c_{13}}{2c_{13}^2 - (c_{11} + c_{12})c_{33}},
$$

$$
s_{33} = \frac{c_{11} + c_{12}}{-2c_{13}^2 + (c_{11} + c_{12})c_{33}},
$$

$$
s_{44} = \frac{1}{c_{44}},
$$

$$
s_{66} = 2(s_{11} - s_{12}).
$$
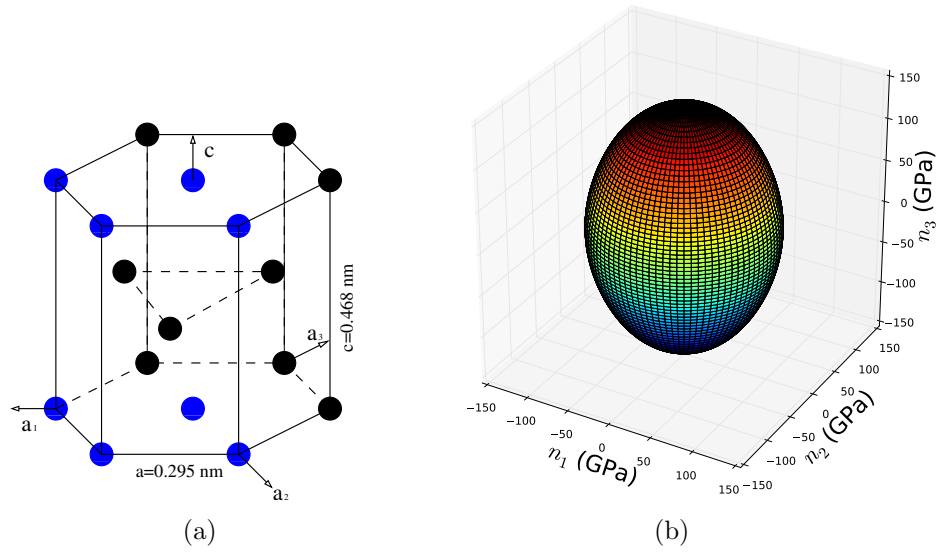
FIGURE 3.1: (a) HCP crystal structure composed of 3 unit cells, one unit cell is represented in blue. (b) Representation of elastic anisotropy for pure α-titanium. The surface represents the magnitude of the Young's modulus for all tensile loading directions $\underline{\boldsymbol{n}}$.

The compliance tensor for pure titanium are as follows:

$$\underset{\approx}{\boldsymbol{S}} = \begin{pmatrix} 0.962918 & -0.465653 & -0.190618 & 0 & 0 & 0 \\ -0.465653 & 0.962918 & -0.190618 & 0 & 0 & 0 \\ -0.190618 & -0.190618 & 0.701696 & 0 & 0 & 0 \\ 0 & 0 & 0 & 2.141328 & 0 & 0 \\ 0 & 0 & 0 & 0 & 2.141328 & 0 \\ 0 & 0 & 0 & 0 & 0 & 0.714286 \end{pmatrix} \times 10^{-5}. \tag{3.4}$$

Under uniaxial tension of magnitude σ along a tensile direction $\underline{\boldsymbol{n}}$, the corresponding stress tensor is given by

$$\underset{\sim}{\boldsymbol{\sigma}} = \sigma(\underline{\boldsymbol{n}} \otimes \underline{\boldsymbol{n}}). \tag{3.5}$$

The normal strain along $\underline{\boldsymbol{n}}$ is

$$\varepsilon(\underline{\boldsymbol{n}}) = \underset{\sim}{\boldsymbol{\varepsilon}} : (\underline{\boldsymbol{n}} \otimes \underline{\boldsymbol{n}}). \tag{3.6}$$

Through Hooke's law, the stress and elastic strain tensors can be related by

$$\underset{\sim}{\boldsymbol{\sigma}} = \underset{\approx}{\boldsymbol{C}} : \underset{\sim}{\boldsymbol{\varepsilon}}^{e} \qquad \text{or} \qquad \underset{\sim}{\boldsymbol{\varepsilon}}^{e} = \underset{\approx}{\boldsymbol{S}} : \underset{\sim}{\boldsymbol{\sigma}}. \tag{3.7}$$

From Equations (3.5), (3.6) and (3.7), the Young's modulus as a function of the direction $\underline{\boldsymbol{n}}$ can be deduced as

$$\frac{\varepsilon(\underline{\boldsymbol{n}})}{\sigma} = \frac{1}{E(\underline{\boldsymbol{n}})} = (\underline{\boldsymbol{n}} \otimes \underline{\boldsymbol{n}}) : \underset{\sim}{\boldsymbol{S}} : (\underline{\boldsymbol{n}} \otimes \underline{\boldsymbol{n}}). \tag{3.8}$$

Equation 3.8 can be written in index form as

$$\frac{1}{E(\underline{\boldsymbol{n}})} = S_{ijkl} n_i n_j n_k n_l \tag{3.9}$$

Young's modulus for hexagonal symmetry expressed in terms of the elastic coefficients s_{ij} is according to [Cazzani and Rovati, 2003]:

$$\frac{1}{E(\underline{\boldsymbol{n}})} = s_{11} - [(s_{11} - s_{33})n_3^2 + (2s_{11} - 2s_{13} - s_{44})(n_1^2 + n_2^2)]n_3^2 \tag{3.10}$$

A schematic representation of Young's modulus $E(\underline{\boldsymbol{n}})$ for pure titanium is plotted in Figure 3.1 (b). Young's modulus is maximum along the [0001] direction with a value of 142511 MPa and minimum on the (0002) plane of with a value of 103850 MPa.

3.1.2 Crystal orientations

The DCT experiment of the pure titanium sample was carried out in 2009 (prior to this project) by W. Ludwig and P. Reischig at the ESRF on the ID19 beamline using a Frelon Charge Coupled Device (CCD) camera with an effective pixel size of 1.5 µm. The setup is similar to Figure 1.1 and the X-ray energy was 36 keV. The distance between the sample and the detector was 6 mm. The diameter of the circular cross section of the sample was 648 µm and the height of the illuminated zone was 423 µm. Two stages of compressive loading were recorded: one at a compressive force of −4 N and one at −29 N. After image reconstruction, 1343 grains were indexed in the volume at −4 N of which 1322 grains remained after merging overlapping grains. Concerning the volume at −29 N, 1401 grains were indexed and 1397 grains remained after the merging operation. Comparing these two datasets, the sample volume at −29 N was chosen for the creation of the FE mesh (see Chapter 2) because it contains more grains than in the volume at −4 N.

The grain orientations in the volume at -29 N are determined by DCT and expressed as Rodrigues vectors ($\underline{\boldsymbol{R}}$) [Becker and Panchanadeeswaran, 1989]. It describes grain orientations by a rotation axis ($\underline{\boldsymbol{c}}$) and an angle of rotation (ω) in the sample coordinate system as follows:

$$\underline{\boldsymbol{R}} = \tan\left(\frac{\omega}{2}\right) \cdot \underline{\boldsymbol{c}}. \tag{3.11}$$

In a Cartesian basis, it can be written as

$$\underline{\boldsymbol{R}} = \frac{\lambda}{\rho}\underline{\boldsymbol{x}} + \frac{\mu}{\rho}\underline{\boldsymbol{y}} + \frac{\nu}{\rho}\underline{\boldsymbol{z}}, \tag{3.12}$$

with $\lambda = c_x \sin\left(\frac{\omega}{2}\right)$, $\nu = c_z \sin\left(\frac{\omega}{2}\right)$, $\mu = c_y \sin\left(\frac{\omega}{2}\right)$, $\rho = \cos\left(\frac{\omega}{2}\right)$, $\underline{\boldsymbol{c}} = c_x\underline{\boldsymbol{x}} + c_y\underline{\boldsymbol{y}} + c_z\underline{\boldsymbol{z}}$ and $\underline{\boldsymbol{x}}$, $\underline{\boldsymbol{y}}$ and $\underline{\boldsymbol{z}}$ the unit vectors of the sample coordinate system.

In the Z-set FE code, grain orientations are specified by Euler angles. In Bunge notations, Euler angles correspond to three angles (ϕ_1, ψ, ϕ_2) that represent three rotations around z, x' and z'' axes, respectively. The x, y, z denote the initial reference frame. x', y', z' are the coordinates after first rotation. x'', y'', z'' are the final coordinate system.

The relationship between the Rodrigues vector and the Euler angles is:

$$\phi_1 = \arctan\left(\frac{\nu}{\rho}\right) + \arctan\left(\frac{\mu}{\lambda}\right) \tag{3.13}$$

$$\psi = 2\arctan\sqrt{\left(\frac{\lambda^2 + \mu^2}{\nu^2 + \rho^2}\right)} \tag{3.14}$$

$$\phi_2 = \arctan\left(\frac{\nu}{\rho}\right) - \arctan\left(\frac{\mu}{\lambda}\right) \tag{3.15}$$

This conversion is applied for each grain to define its orientation measured by DCT. In the framework of small deformation, the grain orientation will be used to rotate the strain tensor in order to solve the constitutive equations as presented from Equation 2.6 to Equation 2.9 in the crystal reference frame.

3.1.3 Boundary conditions

In the DCT measurements at -29 N, it was observed, see Figure 3.2(a), that the compression was not perfectly uniaxial and that a bending load was also present

due to the small misalignment between sample surfaces which were not perfectly parallel. Moreover, from the strain measurements at -4 N, see Figure 3.2(b), it can be noted that the deformation in some grains is already significant, of the order of 0.001. This strain can be considered as a residual strain and should be removed for comparing to the FE strain. Therefore, for the following calculations and comparisons, a difference $\Delta\varepsilon$ of the strain tensors between -29 N and -4 N stages was applied. In order to apply the corresponding Boundary Conditions (BC) in the FE simulations, a linear regression of the $\Delta\varepsilon_{33}$ at $(-29$ N $- (-4$ N$))$, which is -25 N along the direction of compression z was determined as a function of the coordinates (x,y) of the grain centers, see Figure 3.2(c):

$$\Delta\varepsilon_{33}(x, y) = -0.00060 - 0.00243 \ x - 0.00252 \ y, \tag{3.16}$$

with x and y in mm. The displacement difference at the top surface is then written as

$$\Delta U_3(x, y) = \Delta\varepsilon_{33}(x, y) \ H, \tag{3.17}$$

with H the height of the illuminated zone.

By applying $\Delta U_3(x, y)$ according to Equation 3.17 at the top surface of volume in FE, $U_3 = 0$ at the bottom surface and fixing the rigid body movements, the vertical component of the total reaction force (RU3) at the top surface was -28.9 N instead of $(-29$ N $- (-4$ N$)) = -25$ N as measured by the experiment along the loading direction. This difference is thought to be due to the fact that the linear regression used to obtain Equation 3.16 does not take into account the volume of the grains.

Thus, another expression in which each strain contribution to the $\Delta\varepsilon_{33}$ is weighted by its corresponding grain volume is determined. For this purpose, $\Delta\varepsilon_{33}$ is integrated along the loading direction at each pixel of the top surface and then divided by its pixel number of the z-direction. A second linear regression, $\Delta'\varepsilon_{33}$ is then obtained:

$$\Delta'\varepsilon_{33}(x, y) = -0.00044 - 0.00313 \ x - 0.00291 \ y, \tag{3.18}$$

A comparison between Equation 3.16 and Equation 3.18 is shown in Figure 3.2 (d). It can be observed that the new equation represents a slightly higher bending than the old one, which means that the positive part is higher and the negative part is lower. Using the new BC deduced from Equation 3.18 and Equation 3.17,

(a)

(b)

(c)

(d)
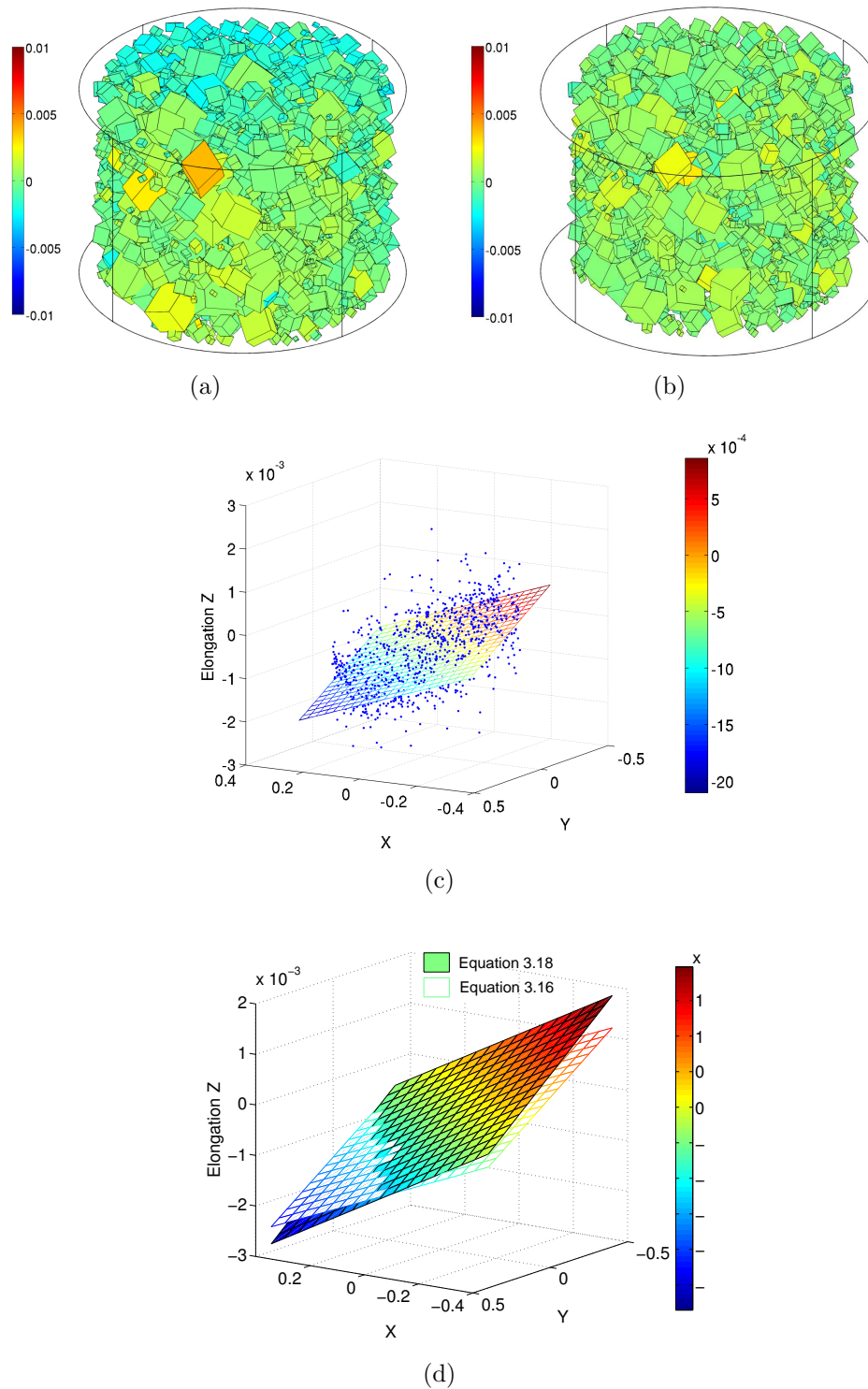
FIGURE 3.2: (a) ε_{33} along the compression direction z in the volume at -29 N. (b) ε_{33} along the compression direction z in the volume at -4 N. (c) Fitting surface (Equation 3.16) of the measured ε_{33} along z at $(-29$ N $-(-4$ N$))$. The accuracy of the measurements is about 5×10^{-4}. (d) A comparison between $\Delta\varepsilon_{33}(x, y)$ (Equation 3.16) and $\Delta'\varepsilon_{33}(x, y)$ (Equation 3.18).

RU3 at the top surface decreased to -21.5 N. The experimental measured force is -25 N, which is between the two calculations.

3.1.4   Comparison of elastic strain tensors

All 165 grains composing the middle slice of the volume were investigated in detail. The strain tensors of grains that lie close to the top and the bottom surfaces were considered not reliable because of the effect of the applied boundary conditions and the incomplete grain shapes due to the limited height of X-ray beam. The shear strains are of the order of 10^{-6} which is below the accuracy of the measurements estimated at about 5×10^{-4}. Therefore, in the following results, only the mean $\Delta\varepsilon_{11}$, $\Delta\varepsilon_{22}$ and $\Delta\varepsilon_{33}$ of each grain are compared.

In Figure 3.3, almost all values of $\Delta\varepsilon_{33}$ are distributed between -0.2% to +0.1%. On the x-axis, grains are sorted by their size: grain number 1 is the largest grain and grain number 1400 is the smallest one. Apart from a few grains, the DCT measurement is able to capture the variations of $\Delta\varepsilon_{33}$ between one grain and another. This can be observed clearly around grain number 400 in Figure 3.3. This variation is mainly due to the different crystal orientations between grains. The capability of following the strain variation can also confirm that the conversion of crystal orientation from the Rodrigues vector to the Euler angles in Equation 3.13, 3.14 and 3.15 is correct. The distribution of this particular strain component is shown in Figure 3.5. It can been seen that the distribution calculated from $\Delta'\varepsilon_{33}(x,y)$ in Figure 3.5 (c) is larger than that in Figure 3.5 (b) calculated from $\Delta\varepsilon_{33}$ and is more similar to the experimental measurements in Figure 3.5 (a), particularly for the grains in tensile load. This can be explained by more bending compression in Equation 3.18.

The experimental $\Delta\varepsilon_{22}$ and particularly $\Delta\varepsilon_{11}$ components shown in Figure 3.3 present distributions larger than the calculated ones. These differences could be induced by the inappropriate boundary conditions in which only the displacement along the z-direction was imposed, but none along x or y. Nevertheless, the measured values are small and close to the resolution limit.

The comparison of $\Delta\varepsilon_{33}$ is plotted by grain size in Figure 3.4, in which the big grains are represented by the big points. The black line along the diagonal represents the same strain value between DCT and FE simulation. The black dashed
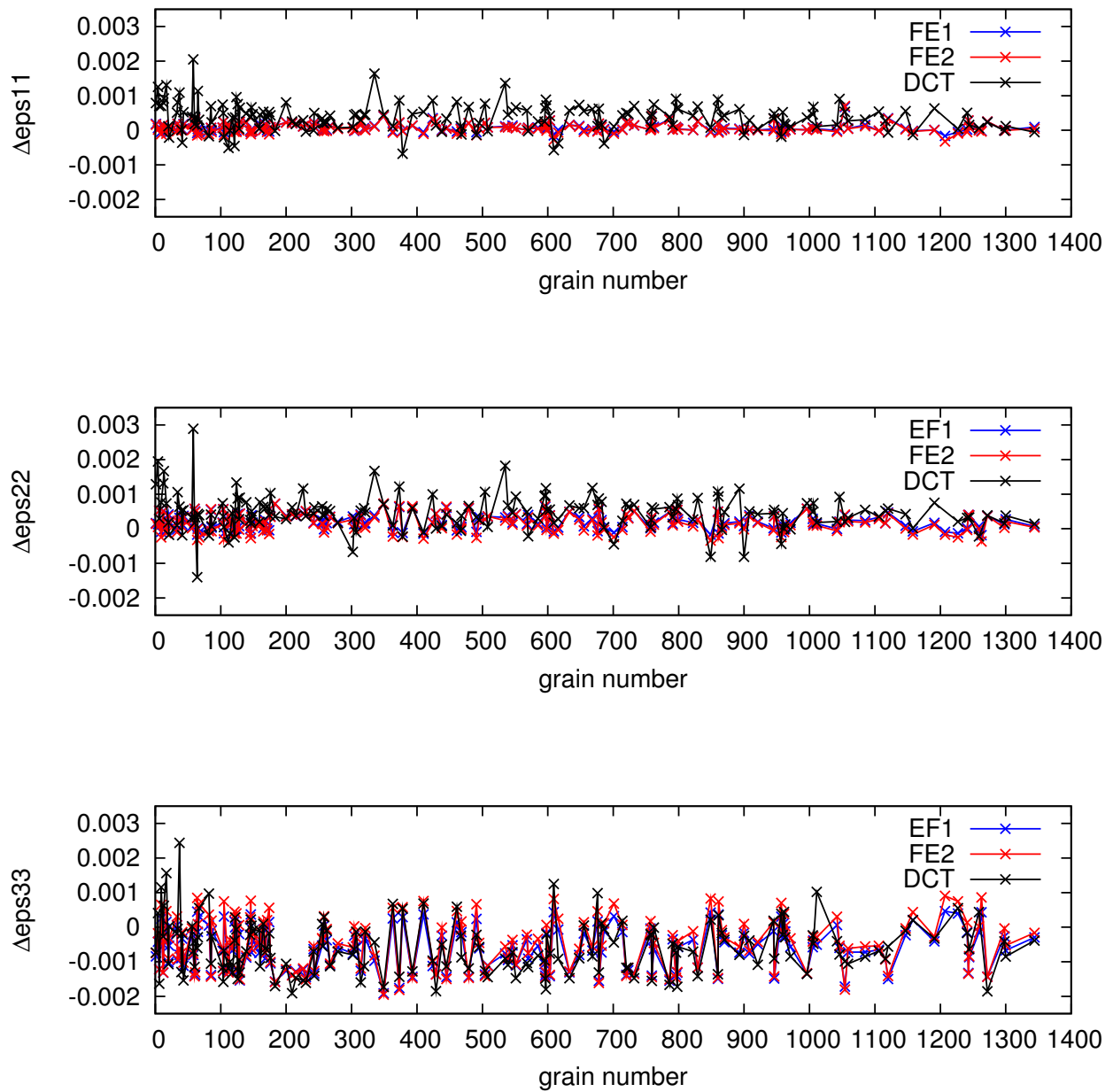
FIGURE 3.3: Comparison of the mean average strain components per grain $\Delta\varepsilon_{11}$, $\Delta\varepsilon_{22}$ and $\Delta\varepsilon_{33}$ between DCT and FE computations with different BC. The uncertainty in these measurements is about 5.10^{-4}.
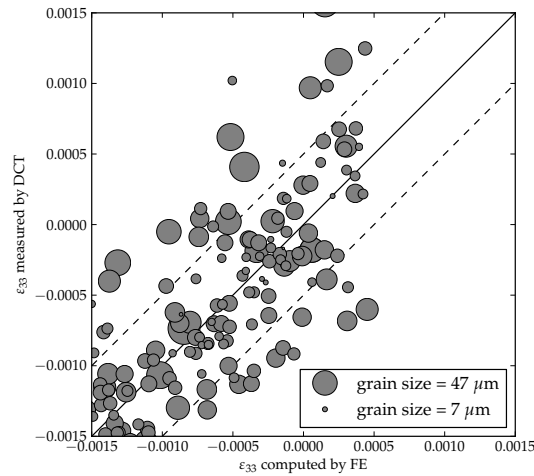
FIGURE 3.4: Comparison of the $\Delta\varepsilon_{33}$ per grain between DCT and FE simulation plotted by grain size.

lines show the ±0.0005 differences that is the precision of DCT measurement. It can be observed that the comparison for the medium-sized grains (grain numbers between 50 and 1000) is satifying. A visual representation of the comparison of this component is given in Figure 3.6. The grains in grey colour represent the largest grains with numbers from 1 to 50. The difference between experiment and FE for medium-sized grains is generally lower than $\pm5 \times 10^{-4}$ i.e. within the experimental uncertainty. For the small-sized grains (with numbers higher than 1000 in Figure 3.3), the DCT measurement is less accurate than that for the medium sized grains, because it is more difficult to identify all the small diffraction spots. Contrary to the small-sized grains, the diffraction spots for the big grains (grain numbers from 1 to 50) are large. However, the comparison of strain tensors of the big grains is also less accurate. This is due to a less precise determination of the center of mass of big grains in the DCT measurements, leading to their unrealistically large deformations, as shown in Figure 3.4.

The reaction force is analysed as a function of vertical position z in the volume, see Figure 3.7. For the experimental force, the mean strain tensors determined in the sample reference frame $\Delta\underset{\sim}{\varepsilon}_s$ are expressed in the crystal reference frame $\Delta\underset{\sim}{\varepsilon}_c$ as follows:

$$\Delta\underset{\sim}{\varepsilon}_c = \underset{\sim}{g} \cdot \Delta\underset{\sim}{\varepsilon}_s \cdot \underset{\sim}{g}^{-1}, \tag{3.19}$$

with $\underset{\sim}{g}$ the orientation matrix of the grain.

(a)

(b)

(c)
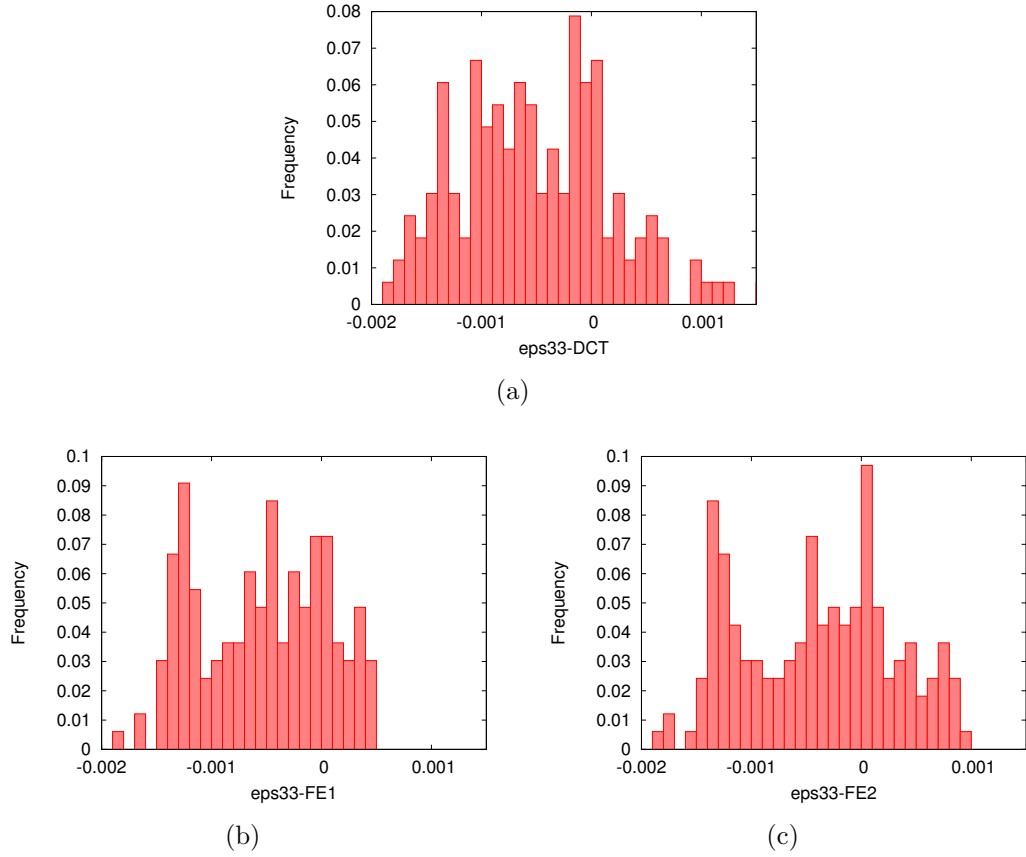
FIGURE 3.5: Distribution of average $\Delta\varepsilon_{33}$ in the middle slice in the DCT measurements (a) and in the FE simulations with the BC based on $\Delta\varepsilon_{33}(x,y)$ (b) and with the BC based on $\Delta'\varepsilon_{33}(x,y)$ (c).

Then, the stress tensors are calculated in the crystal reference frame by linear elasticity:

$$\Delta\underset{\sim}{\boldsymbol{\sigma}}_c = \underset{\approx}{\boldsymbol{C}} : \Delta\underset{\sim}{\boldsymbol{\varepsilon}}_c, \tag{3.20}$$

with $\underset{\approx}{\boldsymbol{C}}$ the fourth order elasticity tensor (Equation 3.1). The stress tensor in the sample reference frame is obtained from

$$\Delta\underset{\sim}{\boldsymbol{\sigma}}_s = \underset{\sim}{\boldsymbol{g}}^{-1} \cdot \Delta\underset{\sim}{\boldsymbol{\sigma}}_c \cdot \underset{\sim}{\boldsymbol{g}}. \tag{3.21}$$

By assuming uniform stress in the grains, the resulting force on each slice is

$$\Delta\underline{\boldsymbol{F}} = \sum_i \Delta\underset{\sim}{\boldsymbol{\sigma}}_{s_i}\underline{\boldsymbol{n}}\,A_i, \tag{3.22}$$

with i the grain number in the slice, $\underset{\sim}{\boldsymbol{\sigma}}_{s_i}$ the average strain tensor of grain i in the sample reference frame, $\underline{\boldsymbol{n}}$ the normal vector of the slice and A_i the area of grain
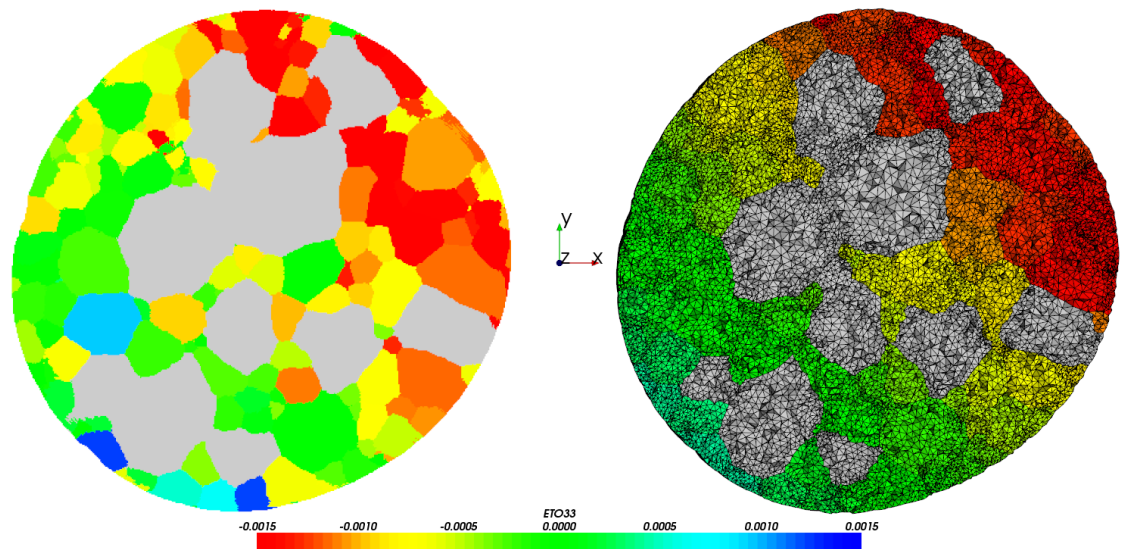
(a)
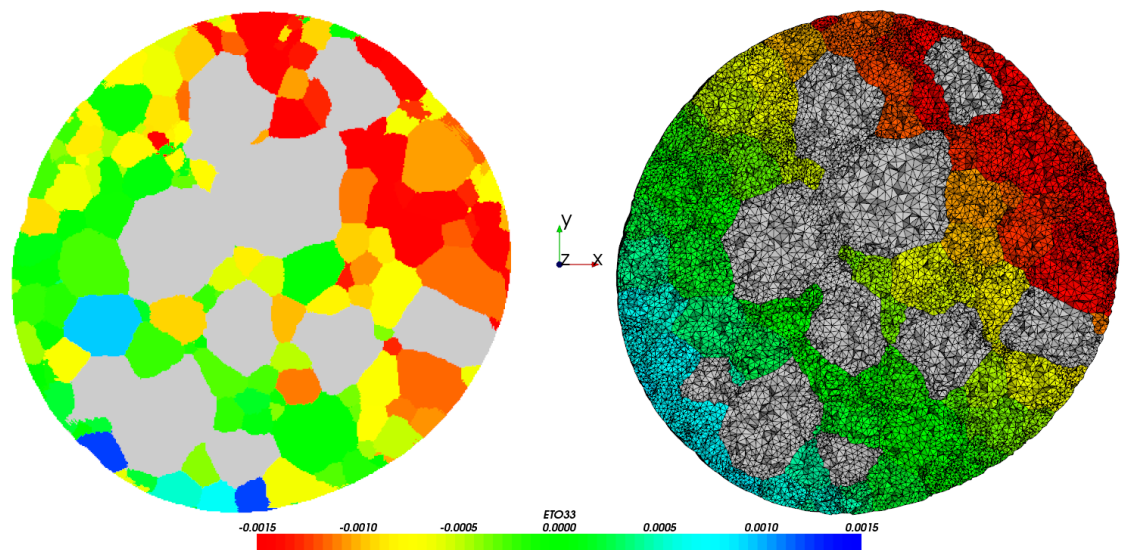
(b)

FIGURE 3.6: Average $\Delta\varepsilon_{33}$ per grain in the middle slice determined by DCT measurements (on the left) and by FE simulations (on the right), using the BC based on $\Delta\varepsilon_{33}(x,y)$ (a), and the BC based on $\Delta'\varepsilon_{33}(x,y)$ (b). The grains in gray color represent the big grains whose numbers from 1 to 50.
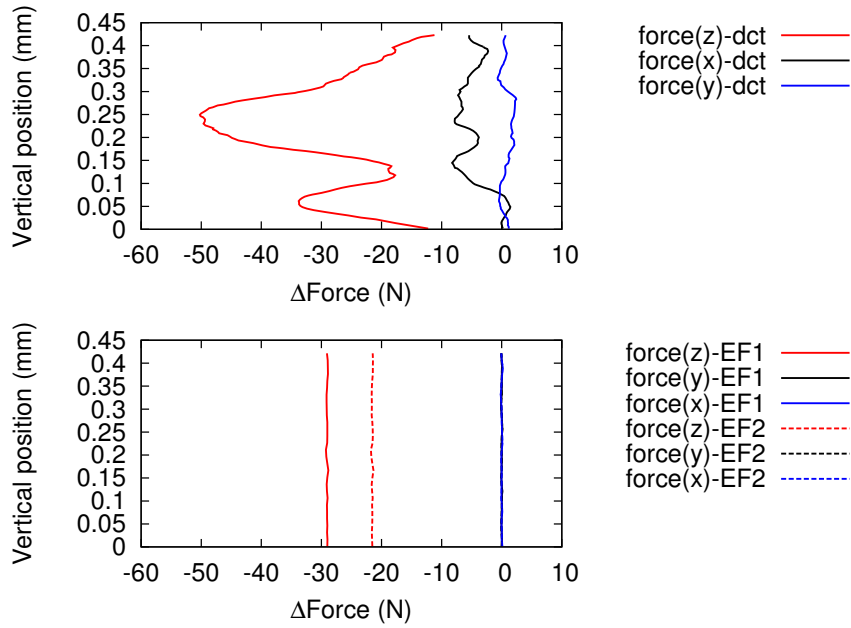
FIGURE 3.7: The variation of the reaction force components along the height of the specimen determined by DCT (top) and by FE simulations (bottom), according to Equation 3.22.

i of the slice, which is calcultated from the tomographic images with the pixel size of 1.5 μm.

In Figure 3.7, it can be observed that the experimental force along the direction z varies through the height of volume. Theoretically, and also in the simulation results, the force is constant on each horizontal slice of volume equal to the applied compression load. This could be caused by the uncertainty of strain tensors in the DCT measurements particularly in the largest grains, which is about 5×10^{-4}, and the inaccuracy of the components $\Delta\varepsilon_{11}$ and $\Delta\varepsilon_{22}$, also $\Delta\varepsilon_{33}$ for the large grains (see Figure 3.3) that influence strongly the component $\Delta\sigma_{33}$ of the stress tensors. Moreover, the assumption of uniaxial stress in Equation 3.22 produces an error of the force less than 1 N. A rudimentary error analysis shows that these uncertainties can indeed cause variations of the same order of magnitude as the measured total force. Furthermore, the reaction forces at the top and the bottom surfaces are smaller than the forces inside the volume. One possible explanation is that the reconstruction of strain tensors involves a complete description of grain shapes. However, the grains at the top and the bottom surface are only partially resolved because they are near the limits of the area illuminated by the X-ray beam.

3.1.5 Conclusions

In this section, the comparison of the mean elastic strain tensors was carried out for the first time grain by grain in a polycrystalline material. The comparison shows that the $\Delta\varepsilon_{33}$ component of strain tensors determined by DCT measurements and by FE calculations are consistent to within the accuracy of the measurement in most of the grains, especially the averaged size ones. The variations around their average values of the distributions of the experimental $\Delta\varepsilon_{22}$ and $\Delta\varepsilon_{11}$ components are larger than the calculated ones. However, the computation with the BC based on $\Delta'\varepsilon_{33}(x,y)$ reveals a more accurate strain distribution with respect to the experimental measured one. The crystal orientations conversion method was also validated. This conversion will be used for the simulation of short fatigue crack propagation.

3.2 Elasto-visco-plastic behaviour of VST55531

The tomographic characterisation of crack propagation was carried out using a VST55531 sample. As explained in Chapter 1, the *in-situ* fatigue experiment was carried out by controled displacement, that corresponded to 40 N of loading amplitude. The global deformation was in the elastic range. However, the local deformation at the crack tip started to plastify. In order to simulate crack propagation in this sample (Chapter 5), the elasto-visco plastic material parameters of the crystal plasticity model are identified.

3.2.1 Mechanical experiments

VST55531 is a near-β titanium alloy with the chemical compositions as shown in Table 3.1. The crystal structure is Body-Centered Cubic (BCC). It is a high-strength titanium forging alloy with minimum ultimate tensile strength of 1240 MPa. The β transus temperature is 803°C. The sample studied in this work was annealed at 843°C for 2 hours under vacuum and then air cooled. After the heat treatment, a fully static recrystallization of the β phase was obtained with a mean grain diameter of 65 μm, as the EBSD measurement shown in Figure 3.8. The heat treatment was carried out by *INSA-Lyon* in the framework of this project.
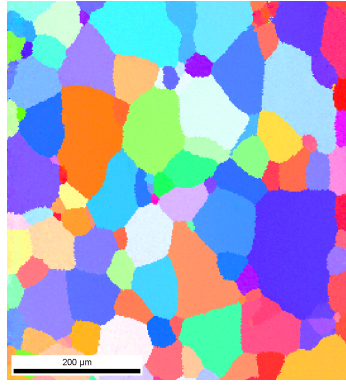
FIGURE 3.8: EBSD micrograph before the fatigue experiment, inverse pole figure coloring.

Ti	Al	V	Mo	Cr	Zr
81	5	5	5	3	1

TABLE 3.1: Chemical compositions in wt% of VST55531.

The experiments were carried out with a servohydraulic MTS test machine, model 810, using axisymmetric specimens, as shown in Figure 3.9. The dimensions of specimen are shown in Figure 3.9 (c). A 120 Ω resistance strain gauge is mounted on the surface of the specimen to measure accurately the axial strain within the range of $\pm 2\%$. The maximum amount of strain in those tests is therefore limited to 2%. This corresponds well to the in-situ fatigue experiment in which the global deformation is still in the range of elasticity.

A strain-controled monotonic tensile test is carried out with two different successive strain rates, see Figure 3.10. The strain rate $\dot{\varepsilon} = 10^{-4}$ s^{-1} is applied until $\varepsilon = 1.5\%$ and then the strain rate changes to $\dot{\varepsilon} = 10^{-3}$ s^{-1}. This is visible in the stress jump at $\varepsilon = 1.5\%$ in Figure 3.10. The strain rate change allows to characterise the viscosity of the material.

Tension-compression tests were performed either in stress control or in strain control, with the deformation rate at approximatly $\dot{\varepsilon} = 10^{-4}$ s^{-1}. For the stress-controlled test, the maximum stress is $\sigma_{max} = 1150$ MPa and the minimum stress is $\sigma_{min} = -1100$ MPa, see Figure 3.11 (a). 17 cycles were performed before the strain gauge failure. Cyclic softening is observed during the first 5 cycles. Then, ratchetting occurs with plastic strain accumulation per cycle of $\delta\varepsilon_p = 0.02\%$. In the strain-controlled tensile-compression test, the imposed strain range is between

(a)   (b)

(c)
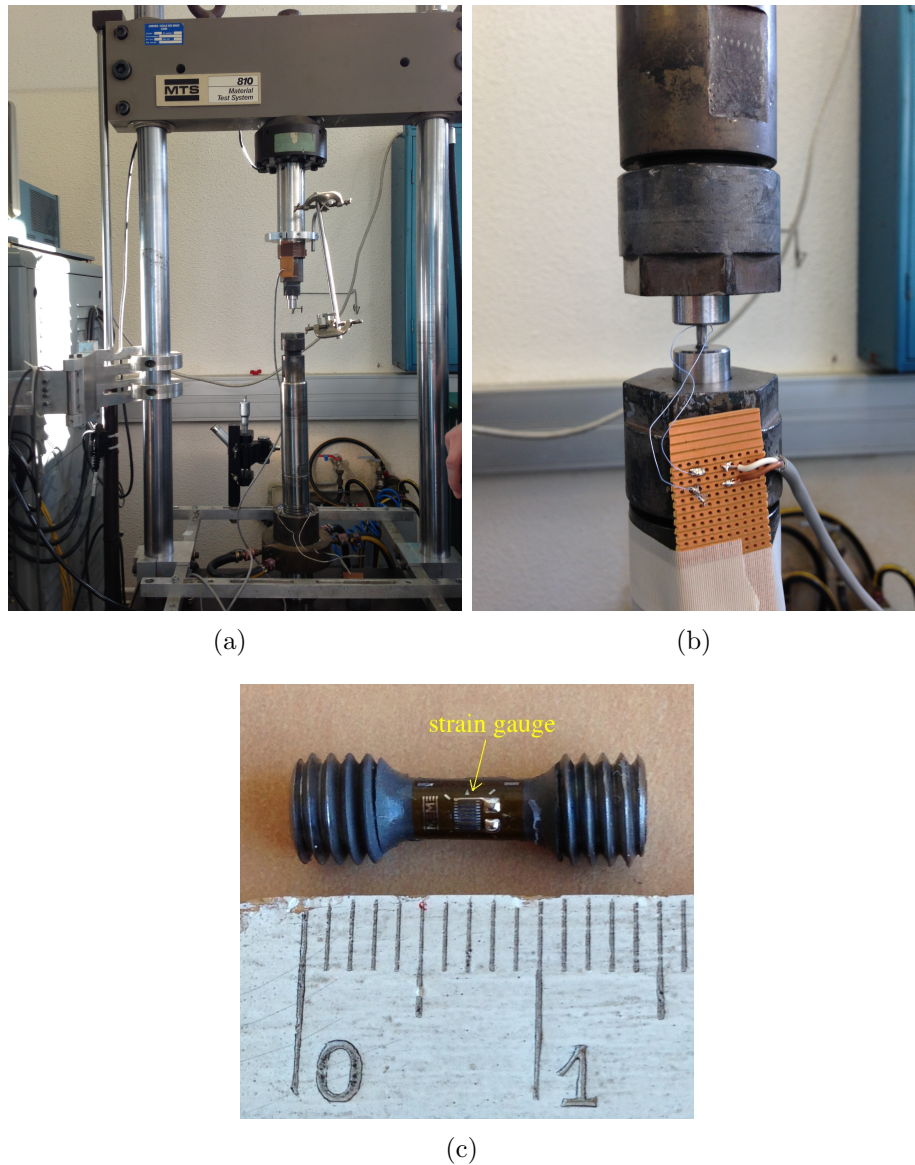
FIGURE 3.9: (a) Tensile-compression machine, (b) with the axisymmetric specimen. (c) The strain gauge is mounted on the surface of the axisymmetric specimen.

$\varepsilon = \pm 1.3\%$. 5 cycles are performed. Cyclic softening is observed in Figure 3.11 (b).

3.2.2   Determination of material parameters

The material parameters are identified by FE simulations using 3D Voronoi aggregate of 100 grains with periodic boundary conditions, see Figure 3.12(a). According to a numerical study in [Martin, 2012], the aggregate is a polycrystalline
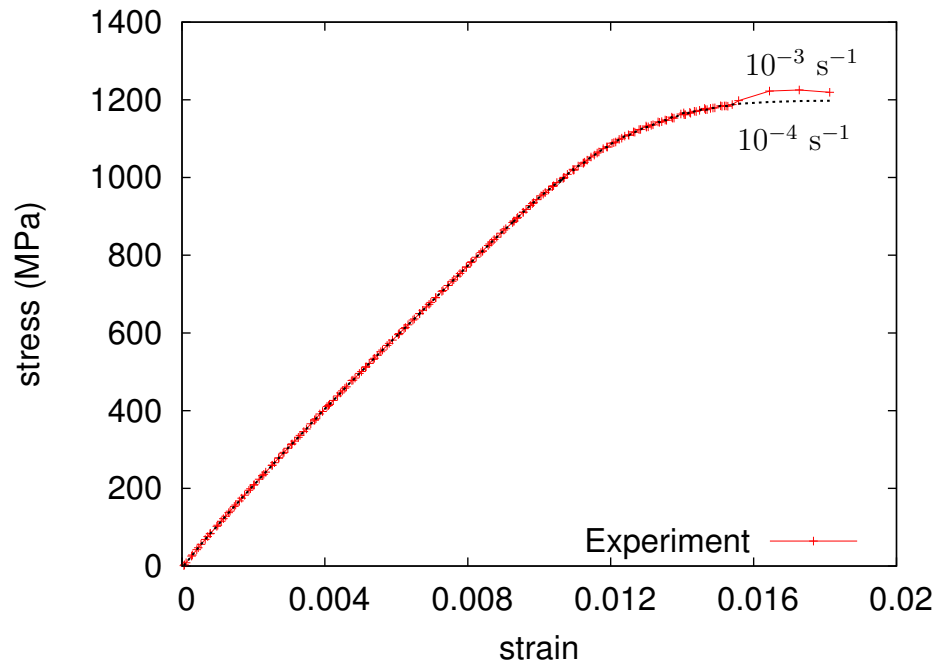
FIGURE 3.10: Tensile test in strain control, the strain rate changes from 10^{-4} to 10^{-3} at $\varepsilon = 1.5\%$. The dotted line in black represents the trend tensile curve at constant strain rate of 10^{-4}.

Representative Volume Element (RVE). The RVE is a material piece that contains sufficient number of grains to represent the isotropic stress-strain curve without any effects of grain heterogeneities. The grain orientations are generated randomly. The {111} pole figure is shown in Figure 3.12(b).

The total strain tensor $\underset{\sim}{\varepsilon}$ is partitioned into an elastic part $\underset{\sim}{\varepsilon}^e$ and a plastic part $\underset{\sim}{\varepsilon}^p$. Regarding elasticity, the material VST55531 has a cubic crystal structure, according to Hooke's law in Equation 2.6, the elastic moduli C_{ij} in Voigt's notation are the following (in MPa) [Fréour *et al.*, 2011]:

$$
\underset{\sim\sim}{C} = \begin{pmatrix}
167000 & 115000 & 115000 & 0 & 0 & 0 \\
115000 & 167000 & 115000 & 0 & 0 & 0 \\
115000 & 115000 & 167000 & 0 & 0 & 0 \\
0 & 0 & 0 & 44000 & 0 & 0 \\
0 & 0 & 0 & 0 & 44000 & 0 \\
0 & 0 & 0 & 0 & 0 & 44000
\end{pmatrix}. \tag{3.23}
$$

The homogenised Young's modulus for RVE is 98500 MPa.
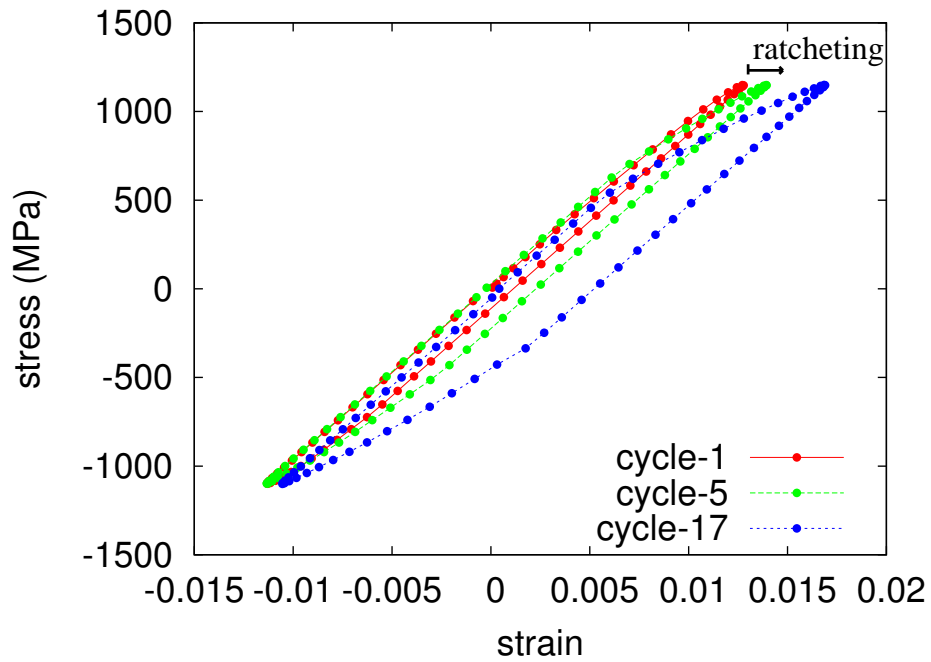
(a)
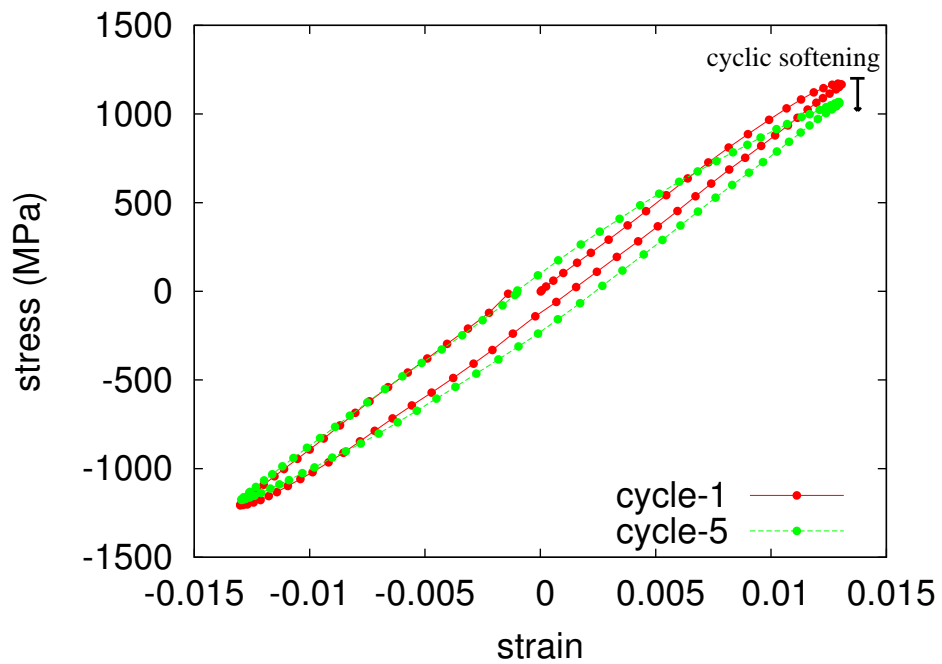
(b)

FIGURE 3.11: Tensile-compression tests in stress control (a) with $\sigma_{max} = 1150$ MPa and $\sigma_{min} = -1100$ MPa, and in strain control (b) with $\varepsilon_{max} = 1.3\%$ and $\varepsilon_{min} = -1.3\%$.
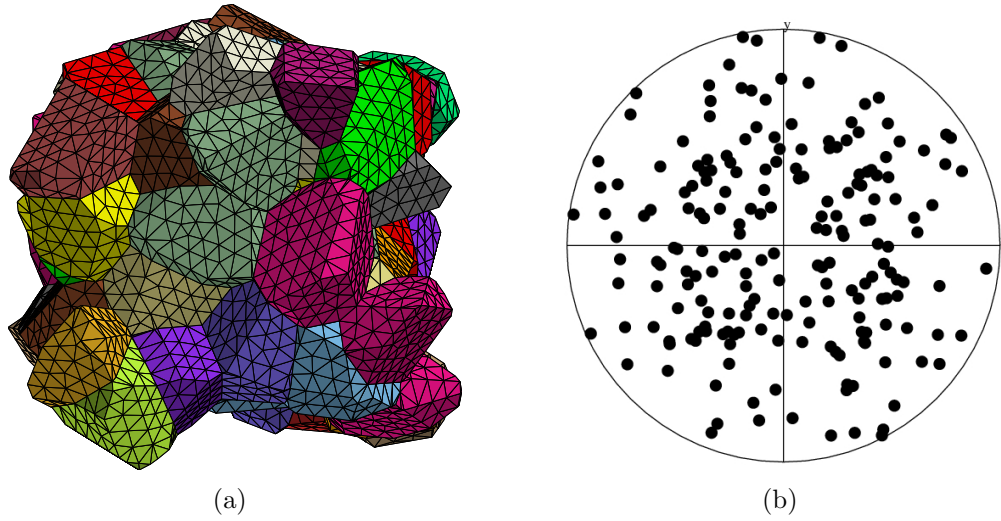
FIGURE 3.12: (a) 3D aggregate of the 100 grains periodic polycrystal. (b) {111} pole figure of the Voronoi aggregate.

The plastic strain is the result of the possible activation of N slip systems s. There for simplicity only 12 $\langle 111 \rangle \{110\}$ slip systems are considered, according to Equation 2.7 and Equation 2.8. Equation 2.9 is here modified to account for isotropic work hardening, as follows:

$$\dot{\gamma}^s = sign(\tau^s) \left\langle \frac{|\tau^s - x^s| - r^s - \tau_0}{K} \right\rangle^n, \tag{3.24}$$

with parameters $K = 100$ MPa.s$^{1/n}$ and $n = 5$. The critical resolved shear stress $\tau_0 = 150$ MPa. r^s is the isotropic hardening. A non-linear isotropic hardening law is used in this work:

$$r^s = Q \sum_{r=1}^{N} h^{sr}(1 - \exp(-bv^r)), \tag{3.25}$$

$$\dot{v}^s = |\dot{\gamma}^s|. \tag{3.26}$$

with $Q = -30$ MPa, $b = 30$. The negative value of Q allows to describe the cyclic softening.

The kinematic hardening x^s is given by:

$$x^s = C\alpha^s \tag{3.27}$$

and

$$\dot{\alpha}^s = (\text{sign}(\tau^s - x^s) - D\alpha^s)\dot{v}^s, \tag{3.28}$$

Viscosity		Isotropic hardening			Kinematic hardening	
K (MPa.s^1/n)	n	τ_0 (MPa)	Q (MPa)	b	C (MPa)	D
100	5	150	-30	30	450000	1400

TABLE 3.2: Viscoplastic material parameters of Ti 55531.

with $C = 450000$ MPa and $D = 1400$.

This non-linear kinematic hardening leads to ratcheting effect when the stress-controlled cycles are not centered, i.e. ($\sigma_{min} + \sigma_{max} \neq 0$). This corresponds to $\Delta\varepsilon_p^{rat} = 0.023\%$ per cycle. The simulation results are shown in Figure 3.13. The visco-plastic material parameters are summarised in Table 3.2. The transition from elasticity to plasticity in the tensile curve is not perfectly identified. This can be better identified by increasing the number of kinematic hardening component, i.e. $x^s = x_1^s + x_2^s$. However, this is not the objective of this work. For the simplicity of the CPFE model, only one kinematic hardening component is considered. A high value of τ_0 limits the microplasticity in grains and particular at the crack tip, which is an essential component for fatigue crack propagation. Moreover, all the simulations of fatigue crack propagation will be performed with imposed displacement. Thus, the identification of strain softening with controled strain was taken carefully.

3.2.3 Conclusions

The elasto-visco-plasticity material parameters of a crystal plasticity constitutive law were identified in this section. The strain gauge can measure precisely the elastic strains at the beginning of plasticity, with the accuracy lower than 0.01% in strain. However, the number of cycles is limited. In spite of these limitations, the parameters will be used to simulate the fatigue crack propagation in Chapter 5. Because the global deformation in the *in-situ* fatigue test was in the elastic range, the plastic deformation will remain confined to the crack tip.
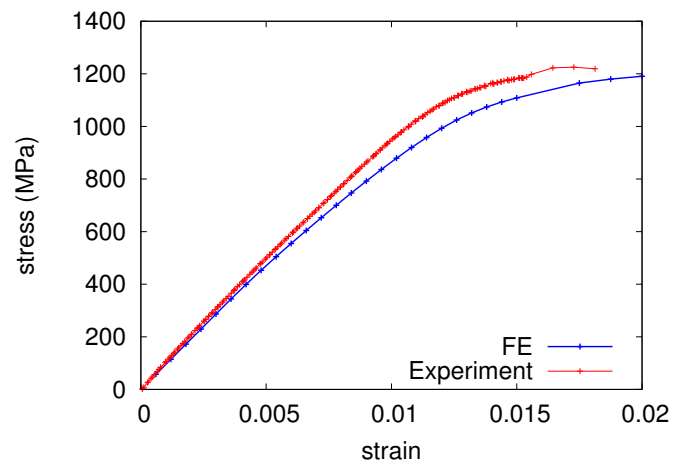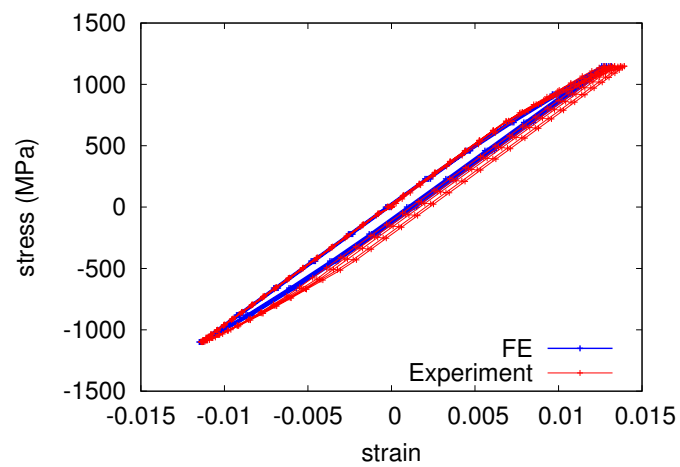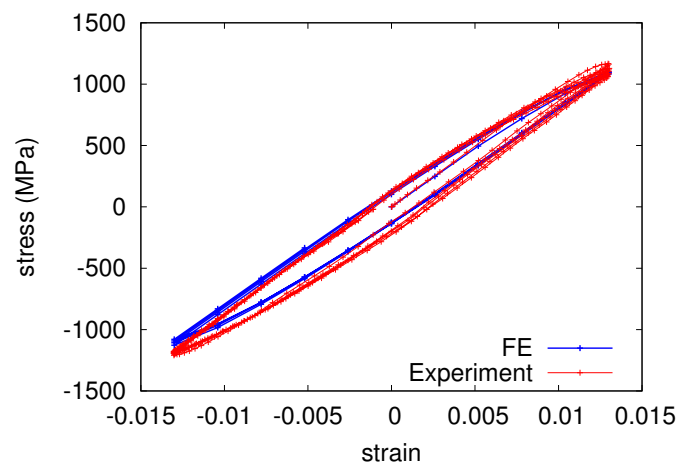
FIGURE 3.13: Simulation results of tensile test in (a), stress-controled test in (b) and strain-controled test in (c).

Conclusions

In the present chapter, using the 3D microstructural mesh reconstructed from the tomographic images and the measured crystal orientations, an elastic compression test is simulated for a pure titanium sample. Different boundary conditions are studied. The simulated mean elastic strain tensors are compared to the experimentally measured ones for the first time grain by grain in a polycrystalline material. In order to prepare the simulation of fatigue crack growth in a VST55531 sample in Chapter 5, the material parameters of crystal plasticity model were identified by a set of mechanical tests.

Conclusions

Dans le présent chapitre, un essai de compression dans le régime élastique d'une éprouvette en titane pur est simulé en utilisant un maillage microstructural créé par des images tomographiques avec l'orientation de grains mesurée expérimentalement. Les tenseurs de déformation élastique moyennés en grains calculés par différentes conditions aux limites sont comparés avec les tenseurs expérimentaux grain par grain. Pour l'éprouvette en alliage titane VST55531 dans laquelle la propagation de fissure sera simulée au chapitre 5, les paramètres de matériau de plasticité cristalline sont identifiés par une série de tests mécaniques.

Chapter 4

Crack Propagation Simulation in Single Crystals

A new method for simulation of 3D crack growth in crystal materials is proposed. Two examples in a BCC single crystal featuring different slip systems demonstrate the crack propagation simulations under monotonic loading over distances comparable to typical grain sizes and with non-regular crack shapes and paths. The effect of transferring state variables between propagation steps is also analysed.

Résumé

Une nouvelle méthode de simulation de la propagation de fissure en 3D dans matériaux cristallins est proposée. Deux exemples d'un BCC monocristal soumis à un chargement monotone sont étudiés avec différents systèmes de glissement. Les fissures qui ont propagé jusqu'à la rupture de monocristal possèdent les formes et les chemins irrégulières. L'effet de transfert de champs entre différents états de propagation est également analysé.
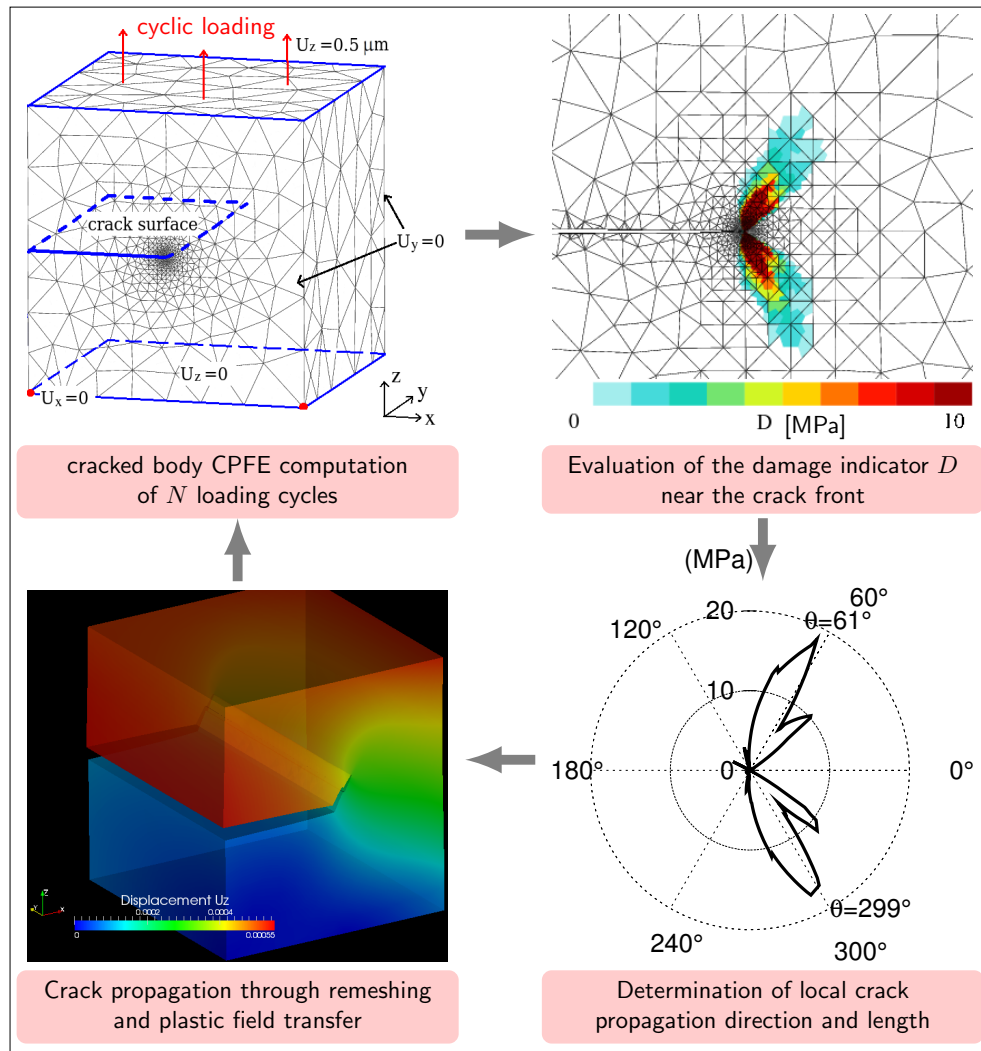
FIGURE 4.1: Crack propagation simulation methodology.

4.1 Methodology

From CPFE computations of a pre-cracked single crystal, a damage indicator based on the accumulated slip, the resolved shear stress and the normal stress on each slip system is calculated at each integration point and for every time increment. The crack growth direction is then determined by analysing the damage indicator in the region around the crack front. The crack is extended via remeshing at each propagation event. At this point the state variables can be transfered to the new crack configuration. The CPFE computation is then continued. Figure 4.1 summarises the main steps of the crack growth simulation methodology.

4.1.1   Damage indicator

The crystal plasticity constitutive equations are described in Equation 2.6, Equation 2.7, Equation 2.8 and Equation 2.9, with Young modulus $E = 110$ GPa, Poisson ratio $\nu = 0.3$, $K = 300$ MPa.s$^{1/n}$ and $n = 3$. During fatigue loading of the pre-cracked sample, plastic deformation occurs near the crack tip due to the dislocation movements along the slip planes. This mechanism is described by the slip γ^s on each slip system s in the crystal plasticity model. When the crack propagates, the tomographic observation of the 3D fatigue crack surface of the VST55531 sample, see Figure 1.4, reveals that the crack propagates mostly on crystallographic planes, although a complex combination of slip planes is observed in each grain to achieve a more or less continuous crack. This stage is governed by the mode II loading and driven by the resolved shear stress τ^s, as explained in [Cheng and Laird, 1983]. In addition, it was demonstrated that the normal stress σ_n^s acting on the slip planes could also influence nucleation and short crack propagation [Fatemi and Socie, 1988]. Therefore, in this work a damage indicator that is the combination of γ^s, τ^s and σ_n^s is retained. Previously, a similar form was proposed by [Dang Van *et al.*, 1989, Fatemi and Socie, 1988]. Here, at each integration point the damage indicator D at time t is the maximum value among the slip systems s, according to

$$D(t) = \max_s \int_0^t |\dot{\gamma}^s|(|\tau^s| + k\langle\sigma_n^s\rangle)\mathrm{d}t, \tag{4.1}$$

with k a material parameter set to 0.4 [Fatemi and Socie, 1988]. This value was found by fitting the uniaxial data against pure torsion data. It enforces the role of normal stress in D. The effect of k will be discussed in section 4.2.3.

4.1.2   Determination of local crack growth direction

4.1.2.1   Local crack front coordinate system

During the numerical procedure, an approximated smoothed crack front Γ, composed of $i+1$ equidistant points on the initial crack front, is computed [Chiaruttini *et al.*, 2012], see Figure 4.2. These nodes are called control points $P_k(0 \leqslant k \leqslant i)$ and do not necessarily correspond to the real mesh nodes. The precision of the approximation can be controlled by the number of control points i. According to a
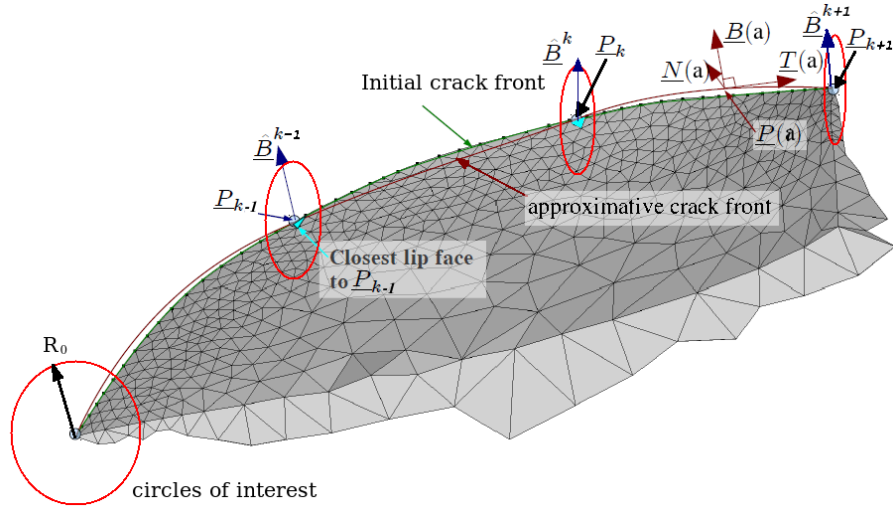
FIGURE 4.2: Schematic representation of initial crack front (green line), approximative crack front Γ (red line), control points P_k (open blue circles), local orthonormal coordinate basis (shown at $\underline{\boldsymbol{P}}(a)$ and the circles of interest of preset radius R_0 (red circles), that is the distance of crack growth, along Γ centered at control points on normal planes to the crack front, edited from [Chiaruttini *et al.*, 2012].

numerical analysis in [Chiaruttini *et al.*, 2012], i should be larger than $1/16$ of the number of nodes on the initial crack front. Any point at the approximated crack front Γ is then modeled as an oriented regular curve $\underline{\boldsymbol{P}}(a)$, with $a \in [0; a_{max}]$ the curvilinear parameter and a_{max} the maximum length of $\underline{\boldsymbol{P}}(a)$.

Then, a local orthonormal coordinate basis associated to $\underline{\boldsymbol{P}}(a)$ is computed, which contains the tangent vector $\underline{\boldsymbol{T}}(a)$, written as

$$\underline{\boldsymbol{T}}(a) = \left\| \frac{d\underline{\boldsymbol{P}}(a)}{da} \right\|^{-1} \frac{d\underline{\boldsymbol{P}}(a)}{da}, \tag{4.2}$$

and the vector $\underline{\boldsymbol{N}}(a)$, defined as

$$\underline{\boldsymbol{N}}(a) = \underline{\boldsymbol{B}}(a) \wedge \underline{\boldsymbol{T}}(a), \tag{4.3}$$

with $\underline{\boldsymbol{B}}(a)$ the normal vector. In order to calculate $\underline{\boldsymbol{B}}(a)$, for any $a \in [0; a_{max}]$, an auxiliary vector $\hat{\underline{\boldsymbol{B}}}(a)$ is introduced as a linear interpolation between $\hat{\underline{\boldsymbol{B}}}_k$ and $\hat{\underline{\boldsymbol{B}}}_{k+1}$, as follows:

$$\hat{\underline{\boldsymbol{B}}}(a) = (1-u)\hat{\underline{\boldsymbol{B}}}_k + u\hat{\underline{\boldsymbol{B}}}_{k+1}, \tag{4.4}$$

with $u = (a_{k+1} - a)/(a_{k+1} - a_k)$. As shown in Figure 4.2, the $\hat{\underline{B}}_k$ vectors are set up at each control point P_k as vectors normal to the crack surface element that is nearest to P_k. Two of these elements are highlighted in light blue in the figure. The orientation of $\hat{\underline{B}}_k$ is such that $\hat{\underline{B}}_k \wedge \underline{T}(a)$ is oriented inside the material, into which the crack propagates. Thus, the normal vector $\underline{B}(a)$ is written as

$$\underline{B}(a) = \frac{\hat{\underline{B}}(a) - (\hat{\underline{B}}(a) \cdot \underline{T}(a))\underline{T}(a)}{\|\hat{\underline{B}}(a) - (\hat{\underline{B}}(a) \cdot \underline{T}(a))\underline{T}(a)\|}. \tag{4.5}$$

With this local orthonormal basis, all the points situated at the circle of radius R_0 around each control points can be defined (see circles of interest on Figure 4.2).

4.1.2.2 Crack growth direction by post-processing the damage indicator

The damage indicator $D(t)$ is computed during the CPFE calculation at all integration points. At the end of the loading sequence, the propagation angle θ is determined by post-processing the radial distributions of D at each control point P_k of the curve representing crack front in the plane $(\hat{\underline{B}}_k, P_k, \hat{\underline{N}}_k)$ which is locally normal to the crack. Then, the crack growth direction is selected as pointing from the origin P_k to the location where the damage indicator is the maximum, at a preset distance R_0 from the origin, see Figure 4.2. The set of propagation directions along the front is used to create the geometry of the crack propagation area, which is then inserted into the FE mesh of the single crystal, as will be explained in detail in subsection 4.1.2.

For the sake of simplicity, in the two examples developed in this chapter, the crack growth distance is set to a fixed value equal to R_0 (*i.e.* 2 μm here). The crack growth distance is then representative of a number of cycles (typically 1000 cycles in the present work). The 2 μm corresponds indeed to the average crack growth distance measured over 1000 cycles in the β-Ti experiment. It is thus clear that the parameter R_0 is related to material properties, loading amplitude and other experimental conditions.

Alternatively, the growth distance could be evaluated from the distribution of D along the crack growth direction θ which decreases rapidly when moving away from the crack tip, see Figure 4.3 (b). It is thus possible to define a threshold of D to define locally the ammount of crack growth. This would be particularly
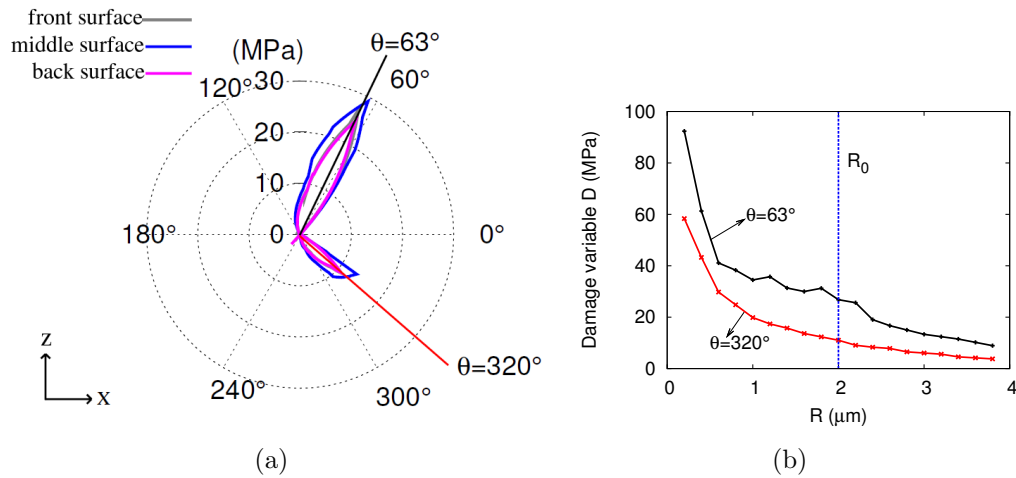
FIGURE 4.3: (a) The damage indicator D (at maximum load) around the crack tip on the xz plane interpolated to the circles of interest of radius of 2 µm on different depths below the surface (represented by different colors). (b) The value of D (at maximum load) along two directions at $\theta = 63°$ and $\theta = 320°$ at the front surface.

useful if done by comparison with experimental measurements, as done in the next chapter.

4.1.3 Propagation through remeshing

Once the crack growth direction has been determined for each control point, a new crack front is generated using the preset crack growth distance R_0. The surface of the crack extension is built using the initial and the new crack fronts. The 3D crack propagation is obtained by inserting the crack extension surface into the single crystal mesh with the Z-cracks software. Detailed information about the crack surface extension procedure is described in [Chiaruttini *et al.*, 2012]. Plastic fields may be transferred to the new mesh at this stage, see section 4.1.4. Next, a new CPFE computation is started with the new FE mesh. Then, the whole routine as shown in Figure 4.1 is carried out again.

4.1.4 Field transfer of state variables

Depending on the chosen propagation length R_0, or on the chosen threshold in D to determine the propagation distance, the crack may exit the plastic zone or not. In the latter case, it is expected that the plastic strain already accumulated during

the past steps may contribute to the distribution of D, influencing the subsequent crack growth. In this case, it is important to transfer the pastic fields between the propagation steps.

After a crack propagation event, the state variables can be transferred to the new mesh and treated as the initial state of the second CPFE computation [Chiaruttini *et al.*, 2013]. The variables U^n at the node whose coordinates are $\underline{\boldsymbol{x}}_n$ in the new mesh are calculated using the standard FE interpolation functions P_i^o associated to the elements E^o as follows

$$U^n = \sum_{i \in E^o} P_i^o(\underline{\boldsymbol{x}}_n) U_i^o, \tag{4.6}$$

with U_i^o the nodal variables in the initial mesh and i the nodes in the element E^o. The variables at integration points in the initial mesh are copied directly to the closest integration points in the new mesh.

Special attention should be paid to the nodes at the crack surface, because they are overlapping on the upper and lower side of the crack. The nodes on each side of the crack belong to a particular node set. During the transfer process, these nodes are distinguished by their node set. Finally, the global mechanical equilibrium of the computation is verified using a very small time increment.

4.2 Crack propagation in the case of a single slip system

In this section, the computational crack propagation method is presented on a simplified test case, as shown in Figure 4.1. It consists of a $(112)[11\bar{1}]$ single slip crystal, in which the initial crack plane is perpendicular to the loading direction and the slip plane is oriented at an angle of 54.7° with respect to the crack plane, see Figure 4.4 (b). In section 4.3, the method is applied to a single crystal with 2 slip systems, $(112)[11\bar{1}]$ and $(11\bar{2})[111]$. The maximum loading applied in the simulations is a nominal stress of 500 MPa which is comparable to the load in the experiments with the β-Ti alloy.

The initial FE mesh is a pre-cracked single crystal with a rectangular crack, as shown in Figure 4.4(a). It is generated by inserting a surface mesh representing the crack into another volume mesh representing a single crystal using Z-cracks as was already explained in Chapter 2. The size of the single crystal is 100 μm ×100 μm ×100 μm, which approximately corresponds to the size of pre-cracked grain 6 in the experimental polycrystalline sample (see the next chapter).

4.2.1 Mesh sensitivity

Mesh sensitivity is analysed with quadratic elements in order to find a reasonable element size with respect to the crack growth distance R_0. For the first crack propagation event in the single slip crystal, the analysed element sizes near the crack front are 0.1 μm, 0.4 μm, 0.6 μm and 0.8 μm. The interpolated variables along the circles and the crack growth direction are identical for every simulation except for the element size of 0.8 μm as shown in Figure 4.6 (a). For the element size of 0.8 μm, D decreases to 23 MPa with respect to 27 MPa for the element size of 0.6 μm and θ increases to 70° with respect to 63°. These differences can be attributed to the discretisation errors during the FE approximations. Thus, to avoid the errors and decrease the computational time, the element size is set to 0.6 μm at the crack front.

4.2.2 Boundary conditions

Regarding the boundary conditions, according to the loading applied in the *in situ* experiments, a displacement of 0.5 μm is applied monotonically in a time interval of 1 s at the top surface in the vertical tensile direction z, and vertical displacement is blocked at the bottom surface, so that the loading rate $\dot{\varepsilon}_{zz} = 5 \times 10^{-3}$ s^{-1}. Detailed boundary conditions are shown in Figure 4.4 (a). Symmetry conditions in the y direction are applied at the back and the front surfaces to minimise the effect of the free surface.

4.2.3 Results

For a single crystal with one slip system $(112)[11\bar{1}]$ oriented in such a manner that the initial crack plane is (001) and the crack front is $[\bar{1}10]$, see Figure 4.4 (b),

(a)   (b)
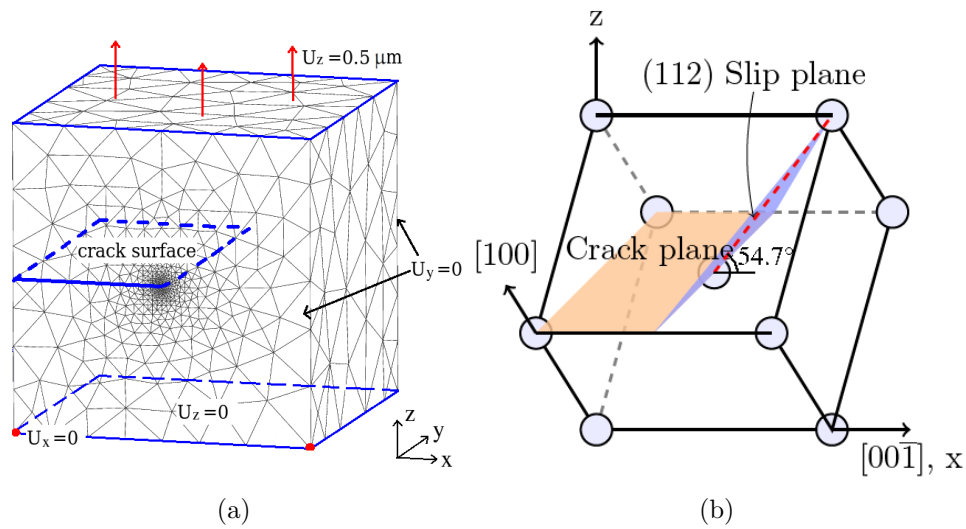
FIGURE 4.4: (a) FE mesh of the pre-cracked single crystal and the applied boundary conditions. The dimension of the mesh is 100 μm³. (b) Schematic representation of the crystal lattice orientation and the single slip system $[11\bar{1}](112)$ of the example in the present section.

Figure 4.3 (a) shows D along the circles of interest at different depths along the crack front, which lies along the y-axis. The different depths are represented by different colours. The crack tip is at the center of the figure. Two branches of D appear, respectively at $\theta = 63°$ and $\theta = 320°$. In order to determine the direction of the crack propagation, the value of D is plotted along these two directions for up to 4 μm from the crack tip, see Figure 4.3 (b).

For a given distance $R_0 = 2$ μm, the value along the direction of $\theta = 63°$ is higher than that of $\theta = 320°$. Therefore, $\theta = 63°$ is selected as the crack growth direction, this holds true all along the y-axis. Figure 4.3 (a) shows that for a mesh size chosen appropriately near the crack front, the crack growth direction does not change with R, at least in a given range of R values (here from 0.6 μm to 4 μm). The crack growth distance of 2 μm corresponds to approximately 3 elements of the FE mesh.

Figure 4.5 (a) shows the damage indicator map at the end of the first cycle. Then, the crack propagated by 2 μm along the direction $\theta = 63°$ through remeshing. The new computation is initialised with the transferred variables, as shown in Figure 4.5 (b). It can be observed that the damage indicator field is rather small with respect to the crack growth distance. Next, the computation continues. The result of D at the end of the second cycle is shown in Figure 4.5 (d). Compared to
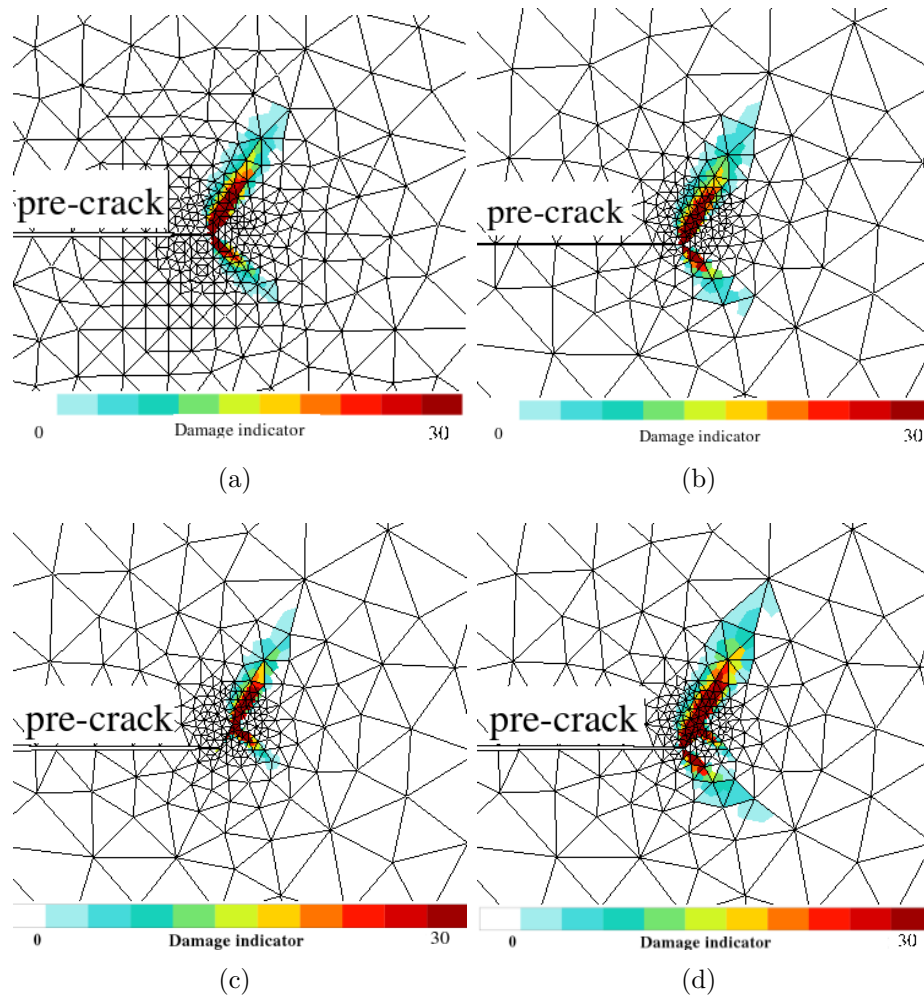
FIGURE 4.5: Front view of the sample with damage indicator D (in MPa) at the crack tip (a) at the end of the first step, (b) at the beginning of the second step with transferred internal variables, (c) at the end of the second step without transferred internal variables, (d) at the end of the second step with transferred internal variables.

the simulation without field transfer, in Figure 4.5 (c), the interpolated value of D to the circles increases slightly in the direction of $\theta = 320°$. However, the direction of crack propagation remains the same at this step. This is related to the single slip system and the 2 µm propagation length, a distance where the accumulated plastic activity is rather small. Another comparison of the FE simulations with and without transfer fields will be given in section 4.3 for a single crystal with two slip systems.

Figure 4.7 shows the intermediate stages among the 32 steps of the crack propagation in the single slip single crystal at the end of step 8, 28 and 32 [Li *et al.*, 2014]. It can be observed that apart a minor bifurcation along the kink direction,
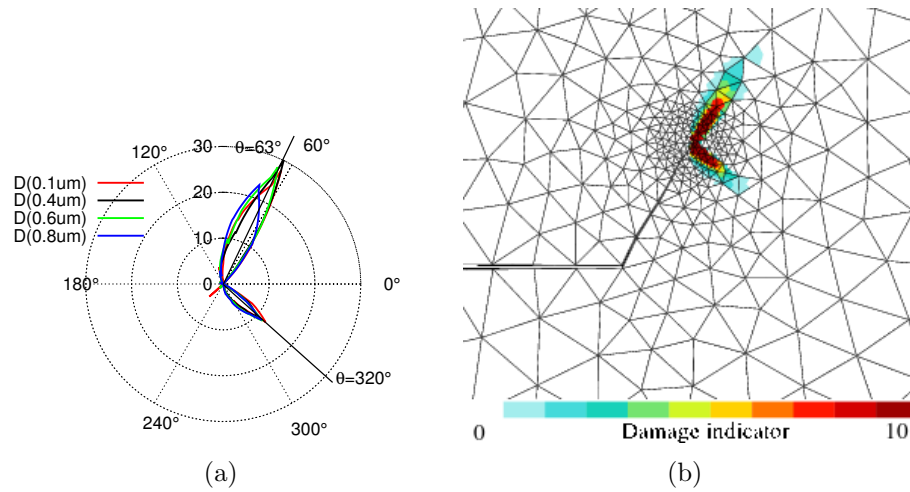
FIGURE 4.6: (a) Damage indicator around the crack tip interpolated to the circles of radius of 2 μm for the simulations with different element size. (b) An intermediate stage of crack propagation with $k = 0$.

and past the pre-crack bifurcation, the crack propagated steadily in a rather constant direction close to 60°. The crack bifurcation occured after 8 μm of crack propagation, i.e. 4 crack propagation events. This kind of crack bifurcation along the kink band direction does exist in fatigue experiments [Flouriot *et al.*, 2003].

In addition, it was found that the crack path is rather stable with the parameter k (Equation 4.1). Another calculation with k set to zero was carried out and the crack path remains identical excepth the crack bifurcation does not take place. Figure 4.6 (b) shows that the 6$^{\text{th}}$ step of crack propagation with $k = 0$.

Apart the small kink bifurcation event, the crack continues upwards, globally in the same direction as the first steps, until the crystal is completely broken. More precisely, the direction of crack propagation decreases progressively from 63° at the beginning to 56° due to the changing equilibrium of structure and the free boundaries as the crack moves forward. It can be observed that the crack growth direction is not exactly along the slip plane, oriented at an angle of 54.7° with respect to the horizontal direction, see Figure 4.4 (b). As a result, the crack surface does not exactly coincide with a definite crystallographic plane. The $\sim 10°$ difference is consistent with the systematic study presented in section 4.2.4 (see Table 4.1 and Figure 4.8) where the crystal is rotated with respect to the loading direction.
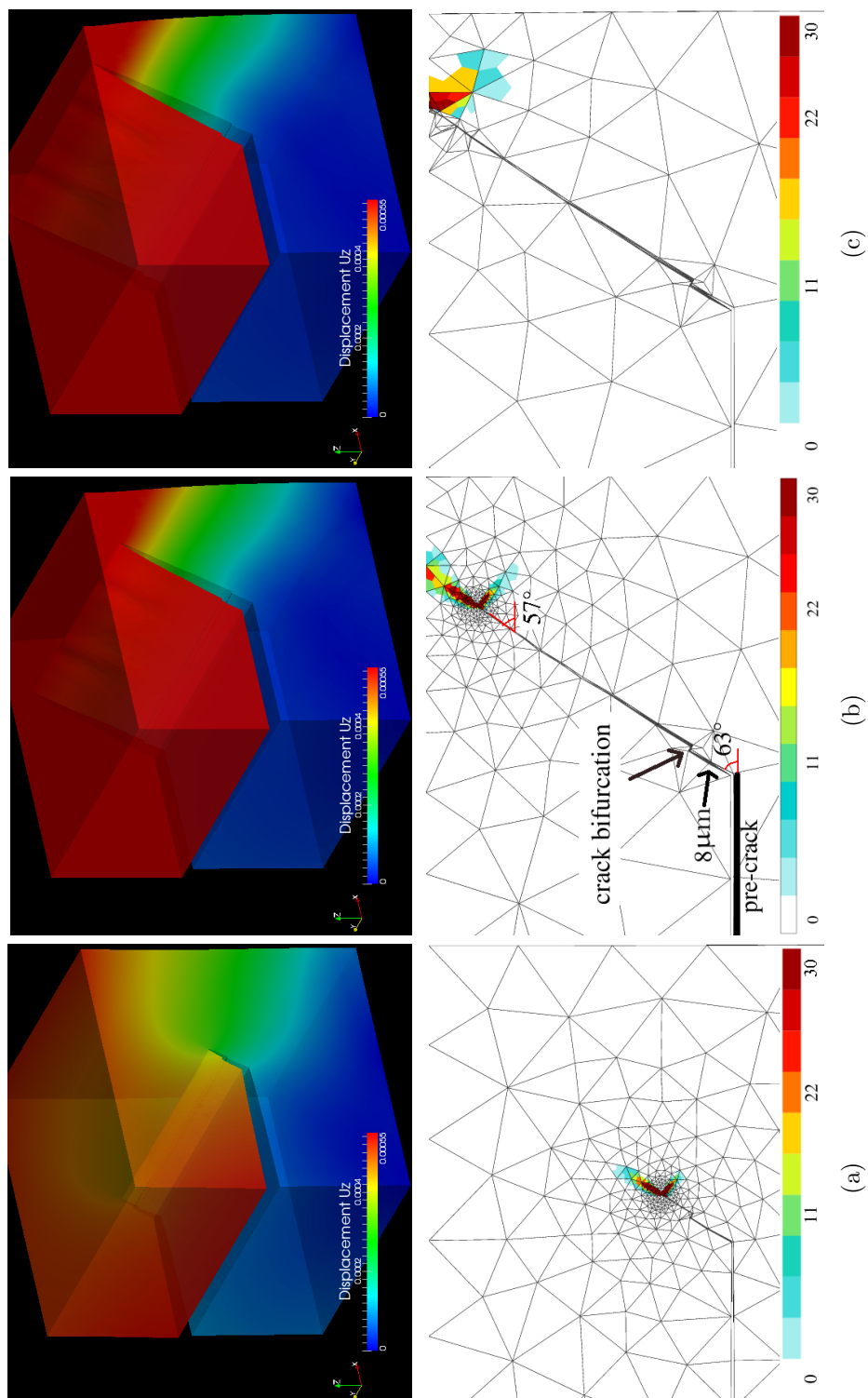
FIGURE 4.7: Crack propagation steps in a single crystal with a single slip system showing both the displacement field in the tensile direction (in mm, the mesh deformation is magnified by a factor 10 for better visualisation) and the damage indicator D (in MPa). (a) step 8, (b) step 28 and (c) step 32.

4.2.4 Influence of the crystal orientation

In order to analyse the influence of the crystal orientation on the crack growth direction, the crystal is rotated for which the (112) slip plane is oriented at an angle ω from 0° to 180° with respect to the horizontal direction. The corresponding crystal orientations expressed in Euler angles (Bunge convention) are given in Table 4.1. For each simulation, D is evaluated along circles of three different radii, (which showed no significant differences) $R = 1.5$ µm, $R = 2.5$ µm and $R = 3.5$ µm.

Angle	0	10	20	30	40	50	60	70	80	90
ϕ_1	180	180	180	180	180	180	0	0	0	0
ψ	54	44	34	24	14	4	5.2	15.2	25.2	35.2
ϕ_2	225	225	225	225	225	225	45	45	45	45
Angle	100	110	120	130	140	150	160	170	180	
ϕ_1	0	0	0	0	0	0	0	0	0	
ψ	45.2	55.2	65.2	75.2	85.2	95.2	105.2	115.2	125.2	
ϕ_2	45	45	45	45	45	45	45	45	45	

TABLE 4.1: The ω angles between (112) slip plane and the horizontal direction, and the corresponding crystal orientations expressed in Euler angles (in degree).

The results show that the crack propagation direction varies for different crystal orientations, as shown in Figure 4.8 (a). The black line represents the variation of angles between the slip plane or the normal to the slip plane and the horizontal direction, resp. ω and $\omega + \pi/2$ [π]. Thus, according to the maximum of D, the crack propagates in a direction close to the slip plane or the slip plane normal. More precisely, the propagation direction is close to the slip direction in the range $\omega \in [35°, 125°]$ and close to the kink direction otherwise. This can be explained by the equivalent role of slip plane and slip direction in the small deformation in Equation 2.8.

However, an unforeseen systematic difference of about 10° between the crack growth direction and the slip plane or the slip plane normal is observed, which is attributed to the competition between crystal plasticity and the global mechanical equilibrium with the horizon pre-crack. Another calculation with the pre-crack lying exactly along the slip plane shows that the distribution of D is maximum at $\omega = 54°$, i.e. just along the crystallographic direction.

(a)

(b)
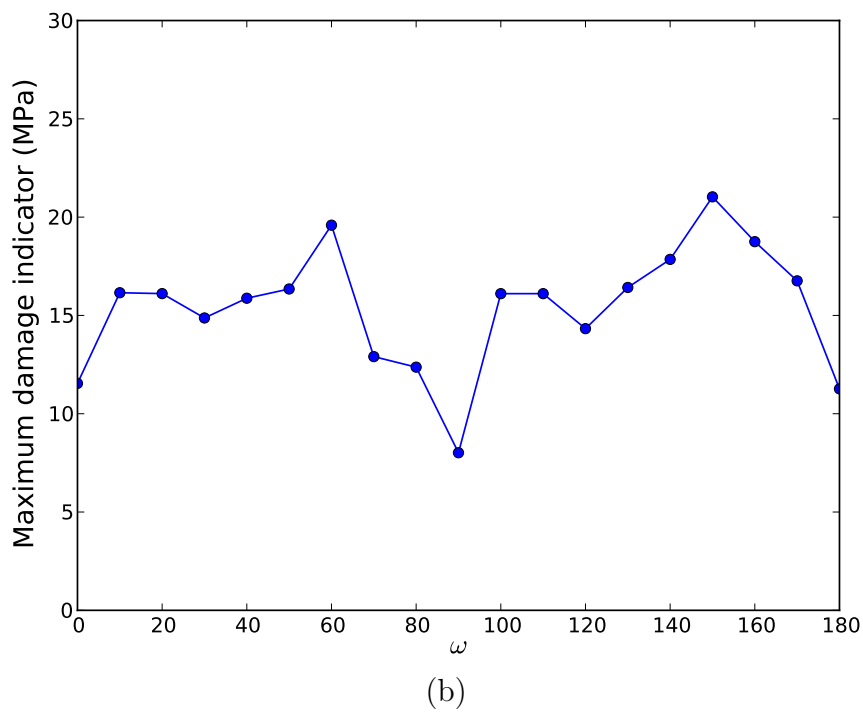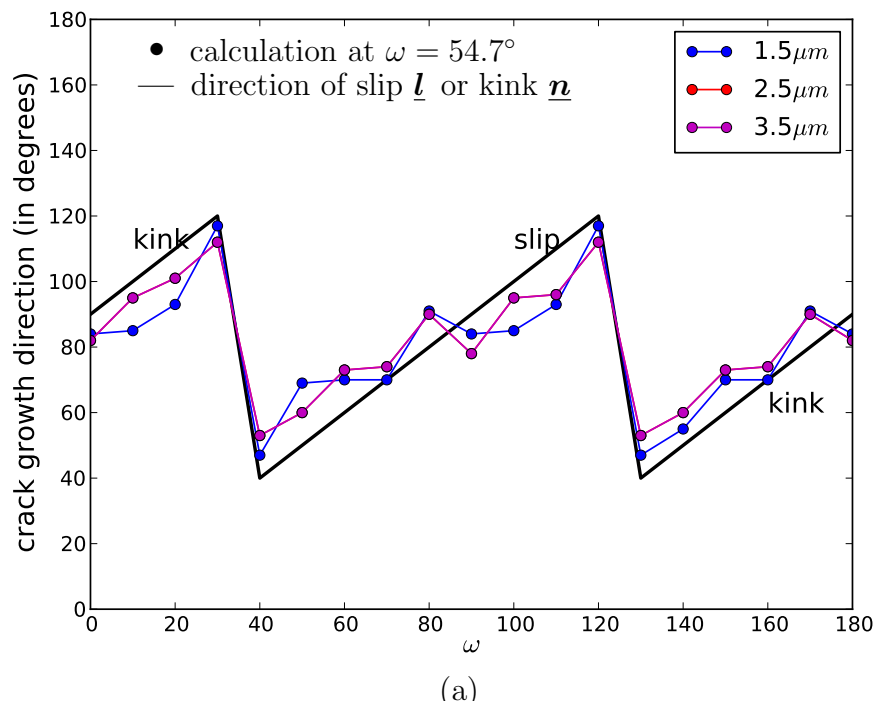
FIGURE 4.8: (a) The variation of crack growth directions for different crystal orientations at which the angle ω between (112) slip plane and the horizontal direction varies from 0° to 180° and the corresponding values of D (b).

The corresponding values of D along the crack growth direction at a radius of $R = 1.5$ μm are shown in Figure 4.8 (b). At ω equals to 0°, 90° and 180°, the value of D is smaller with respect to other orientations. At $\omega = 60°$ and $\omega = 150°$, D reaches a higher value, which means that the plastic slip is large, thus, the crack will propagate more easily for these two crystal orientations. The variation of D will be useful to define the crack growth rate by applying a threshold, as described in the next Chapter.

4.3 Crack propagation in the case of two slip systems

In this section, crack propagation simulation in a single crystal with two slip systems, $(112)[11\bar{1}]$ and $(11\bar{2})[111]$, are considered. These two slip planes are symmetric with an angle of $\pm 54.7°$ with repect to the pre-crack plane (001) and the slip directions are normal to the crack front $[110]$. The minimum element size at the crack-tip is 0.1 μm in this case.

The first simulation is carried out without transferring state variables. The crack propagation distance is the same as in the single slip case with $R_0 = 2$ μm. Applying the same boundary conditions as in Figure 4.4, the results of 22 steps of crack propagation are shown in Figure 4.9 (a). Before the crack propagation, the value of D along $\theta = 61°$ is 18.5 MPa that is slightly higher than D along $\theta = 299°$, which equals to 17.3 MPa, see Figure 4.10 (a). Therefore, the initial crack growth direction is selected along $\theta = 61°$ with respect to the horizontal direction.

Then, the CPFE continues and the global balance of the structure involves that the value of D at $\theta = 299°$ increases, as shown in Figure 4.10 (b). Also, the direction of $\theta = 61°$ in Figure 4.10 (a) changes to $\theta = 59°$. The crack propagates along $\theta = 299°$ for the second step of crack growth. As a result, it grows alternatively along the two directions that forms a zig-zag crack shape as shown in Figure 4.10 (a). This type of crack bifurcation was observed in nickel-based superalloy at 650° as well as a 2024 aluminium alloy, see Figure 4.9 (b) and (c) respectively. In each case, the particular crystallographic configuration is such that two slip systems equally activated are in competition.
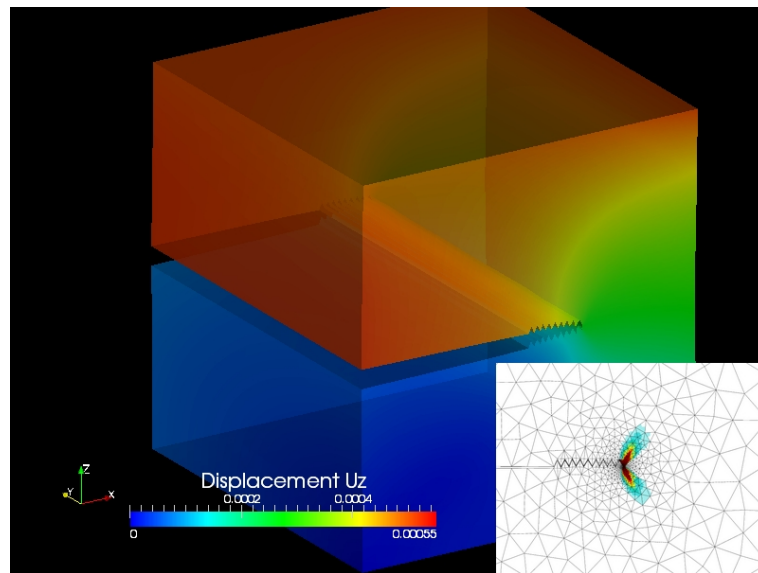
(a)
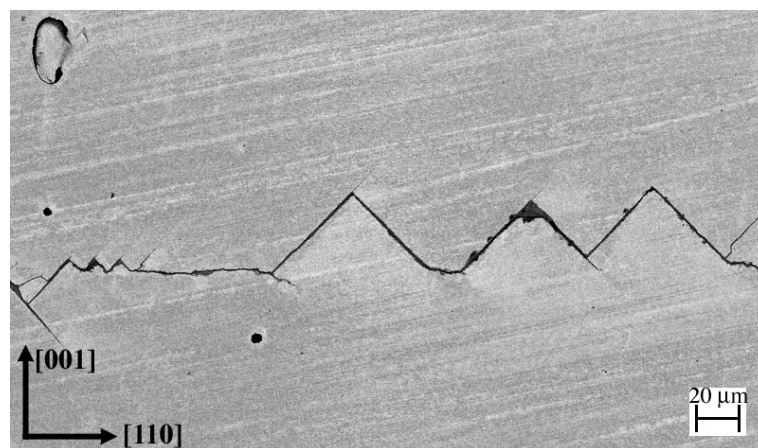
(b)
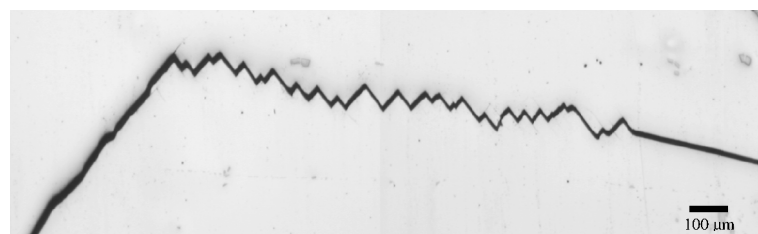
(c)

FIGURE 4.9: (a) Simulation results of crack propagation in double slip single crystal without tranferring field variables. (b) Experimental crack bifurcation in a (001)[110] nickel-based superalloy CT specimen in fatigue at 650° [Marchal, 2006]. (c) Fatigue crack propagation in a 2024 aluminium alloy [Proudhon, 2005].
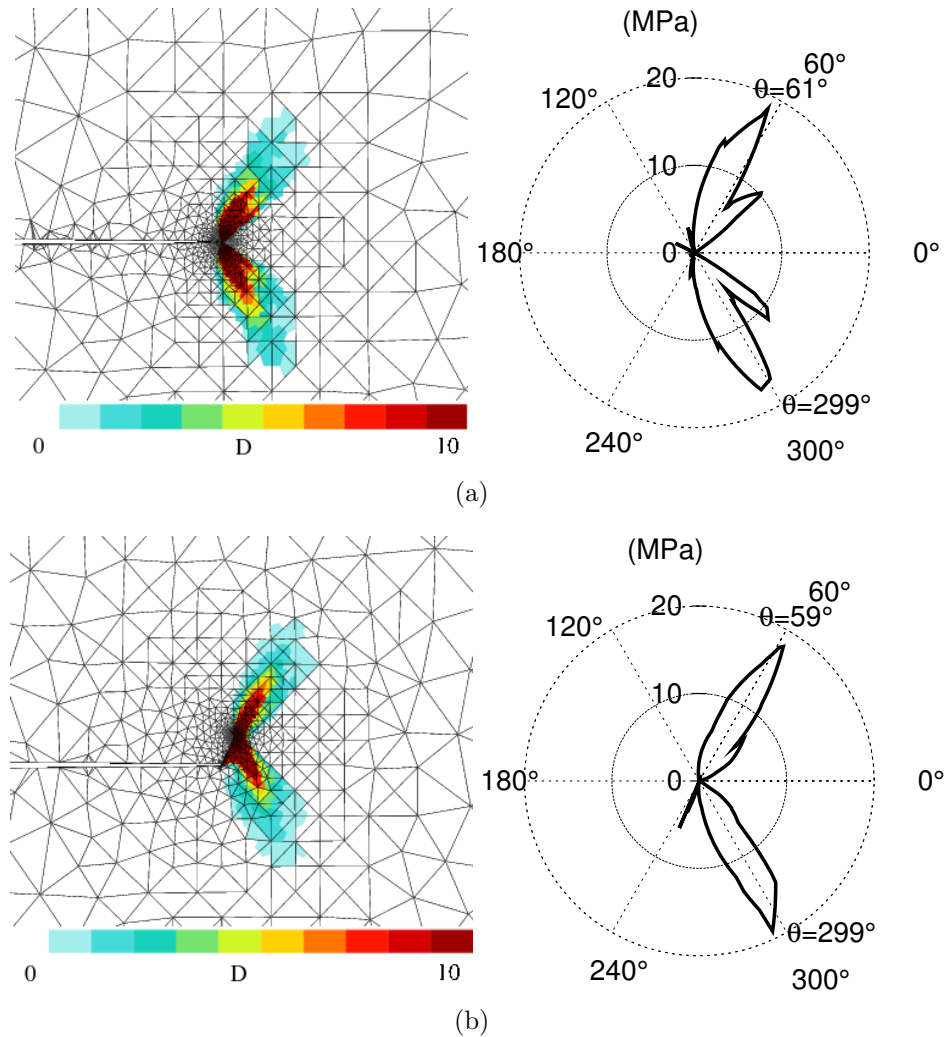
FIGURE 4.10: The damage indicator at the crack tip before crack propagation and the value of D evaluated at a circle of a radius of 2 μm (a) and at the first step of crack propagation (b).

Compared to the distribution of D in the single slip case in Figure 4.3 (a), the maximum value of D in the double slip calculation in Figure 4.10 (a) is smaller. This can be associated to different values of the driving force for the crack which lead to different crack growth rate. An important point to notice here is since the plastic fields are not transferred from one step to the next, the crack will bifurcate whatever the fixed propagation distance is. This is confirmed by simulations with crack growth distances of $R = 1$ μm and $R = 0.5$ μm. The crack bifurcates also after each loading sequence whatever the crack growth distance.

The second set of simulations takes into account the transferred field variables in order to compare the differences to the previous calculations without field transfer

and determine where the crack will bifurcate. R_0 is chosen to be small, which is 0.5 μm, because crack can bifurcate either through very small or large distance. Figure 4.11 (a) and (b) show the distribution of D at the end of the first propagation. With the transferred variables, the field of D at the crack tip of the previous cycle can be observed apparently. The crack propagates along the direction of $\theta = 59°$. Figure 4.11 (c) shows the damage indicator after 2 steps of crack propagation, i.e. 1 μm. Because the variables are transferred from previous step to the next, the value of D cumulates along the direction of $\theta = 59°$. The crack bifurcation does not occur at the second step of crack growth. It can be anticipated that due to the increasing crack length, the mechanical equilibrium will change and at some point the crack bifurcation will take place. This point in the simulation has not however been reached due to a lack of time.

In the present section, the crack propagation simulations of a single crystal with two slip systems were carried out. Without considering the field variables transfer, the crack bifurcations occured at the end of each cycle for the crack growth distance R_0 of 0.5 μm, 1 μm and 2 μm. The zigzag crack propagation can be explained by that the symmetric slip systems with respect to the pre-crack plane make the two slip systems have a very similar values of D. Therefore, with the mechanical balance of the crystal, the crack hesitates between the two systems and propagates along the two systems alternatively.

However, by conducting the calculations with field transfer, the crack bifurcation didn't occur after two crack propagation steps for $R_0 = 0.5$ μm. Because the 0.5 μm crack growth distance is small compared to the damage indicator field, the plastic field of the previous step become important. However, if the propagation distance is large (larger than the plastic zone size) and the crack propagates to where D is almost zero, the plastic field transfer would be less important. This is the reason that the simulations in Chapter 5 are carried out without transferring plastic field variables.

Conclusions

The methodology of crack growth simulation is presented. The crack propagation simulations were performed in a single crystal with one and two slip systems. The crystal orientation effects were analysed for the single crystal with one slip

(a)

(b)

(c)
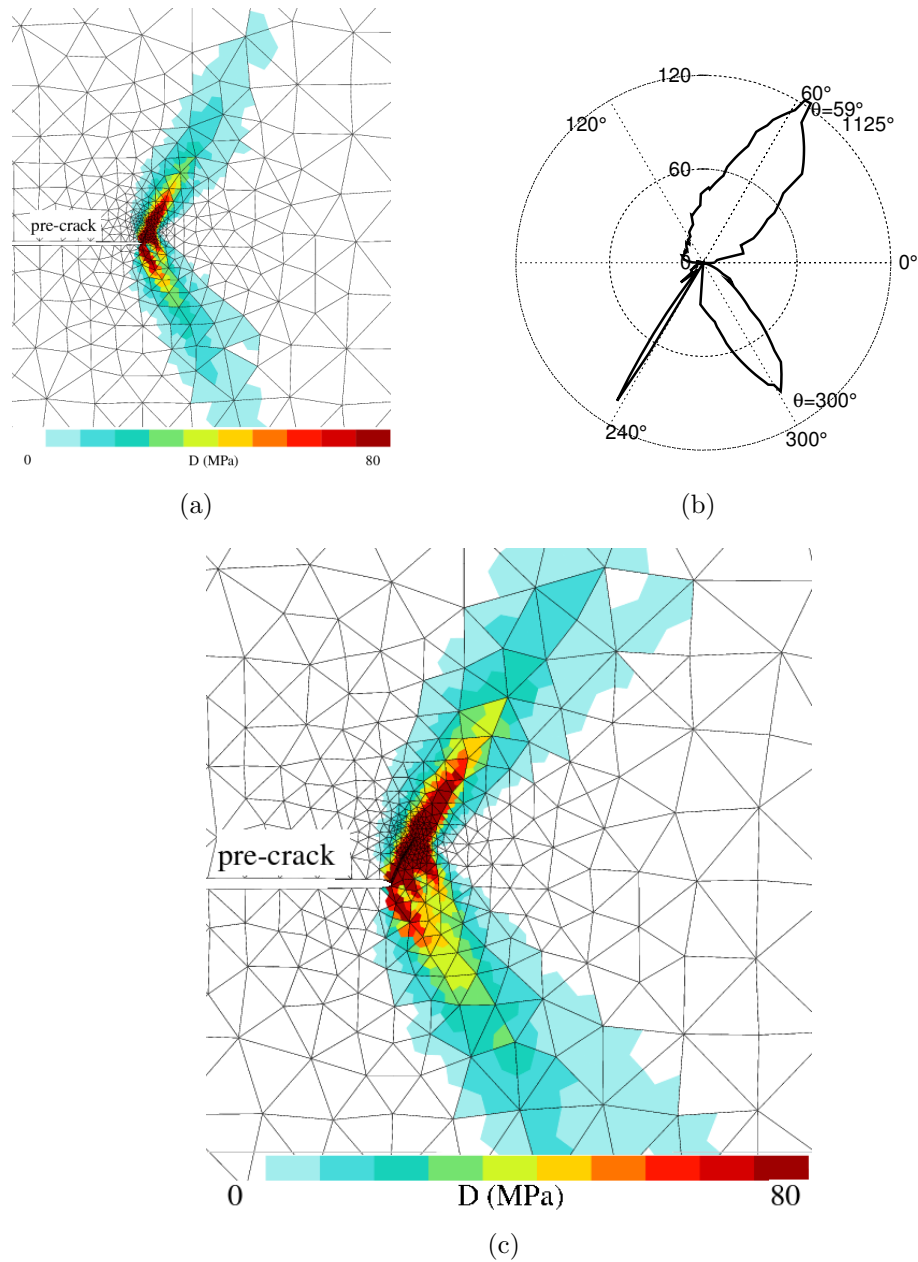
FIGURE 4.11: The results of double slip systems with field transfer (a) at the end of the first cycle, the corresponding value of D at a circle of 0.5 µm radius (b) and at the end of the second cycle (c).

system. The zigzag crack bifurcation was simulated in the two slip systems single crystal. The state variable transfer between propagation steps were considered for both simulations. For simplicity, crack propagation simulations in the present chapter were carried out with a fixed crack growth rate. The definition of crack growth rate will be introduced in the next chapter.

Conclusions

La méthodologie de simulation de propagation de fissure est présentée. Les simulations ont été effectuées dans un monocristal avec un et deux systèmes de glissement. L'effet d'orientation de cristal ont été analysés dans le monocristal avec un système de glissement. La fissure en zigzag a été simulée dans le monocristal avec deux systèmes de glissement. Les variables d'état ont été transférés d'une étape de propagation à une autre dans ces deux exemples. La distance de propagation a été considérée comme un constant pour simplifier. La vitesse de propagation sera introduite dans le chapitre suivant.

Chapter 5

Crack propagation simulation in polycrystals

In this chapter the crack propagation method is applied to the simulation of the cyclically loaded real polycrystal mesh reconstructed in Chapter 3 with an initial pre-crack. Before any crack propagation, a CPFE simulation is carried out and the plastic behaviour of grains at the crack front is analysed in detail in Section 5.1. Then local crack growth rates are defined from the damage indicator along the crack front in Section 5.2. The influence of the formulation of the damage indicator on the crack growth direction is analysed in Section 5.4. At the end of this chapter, the results are compared with the real crack as measured by X-ray tomography.

Résumé

La méthode de propagation de fissure est appliquée à un polycrsital réel pré-fissuré reconstruit dans Chapitre 3. Avant de simuler la propagation de fissure, les champs de slip dans les grains autour de front de fissure sont analysés par le calcul CPFE dans Section 5.1. Ensuite, la vitesse locale de propagation est définie par l'indicateur d'endommagement au long de front de fissure dans Section 5.2. L'influence de formulation de l'indicateur d'endommagement sur la direction de propagation est ensuite analysée. Les fissures simulées et expérimentales sont comparées à la fin du chapitre.

grain	ϕ_1	ψ	ϕ_2
6	142.8	32.0	214.4
52	196.4	3.7	202.4
221	81.1	25.4	291.1

TABLE 5.1: Grain orientations in the sample reference frame shown in Figure 5.4

5.1 Plastic behaviour of grains before propagation

The pre-crack passes through three grains: grain 6, grain 52 and grain 221. Their positions with respect to the surface pre-crack are shown in Figure 5.1. It can be observed that the crack front in grain 221 is close to the grain boundary both at the sample surface and in the bulk. The influence of the grain boundary on the plastic behaviour will be investigated in this grain.

The crystal orientations are given in Table 5.1 and the corresponding pole figures are shown in Figure 5.2. One can observe that the poles distribute over the pole figures and the grains have distinct grain orientations. First, the mechanical behaviour of the individual grains treated as single crystal in tension is simulated using a unique Gauss point with the single crystal plasticity model, described in Chapter 3. A strain of 5% is imposed along the $z-$direction in the sample coordinate frame. There is no effect of grain geometry and neighbouring grains in these reference simulations. The stress-strain responses of the three single grains are shown in Figure 5.3. Grain 6 has the highest apparent elastic modulus due to its orientation. A softening is observed in the three grains because of the negative isotropic hardening parameter Q, see Chapter 3.

Several slip systems can be activated in a grain according to its orientation. The slip system activation is calculated by Schmid's law. In a pure tensile test it simplifies as

$$\tau^s = \underset{\sim}{\boldsymbol{\sigma}} : \underset{\sim}{\boldsymbol{m}^s} = \sigma \cos\theta \cos\chi, \tag{5.1}$$

with θ and χ the angles between the tensile direction and the slip direction and the slip plane normal. The coeffcent $\cos\theta\cos\chi$, called the Schmid factor, for the three grains is given in Table 5.2. The highest absolute value of the Schmid factor corresponds to the most easily activated slip system in the grain in simple tension.
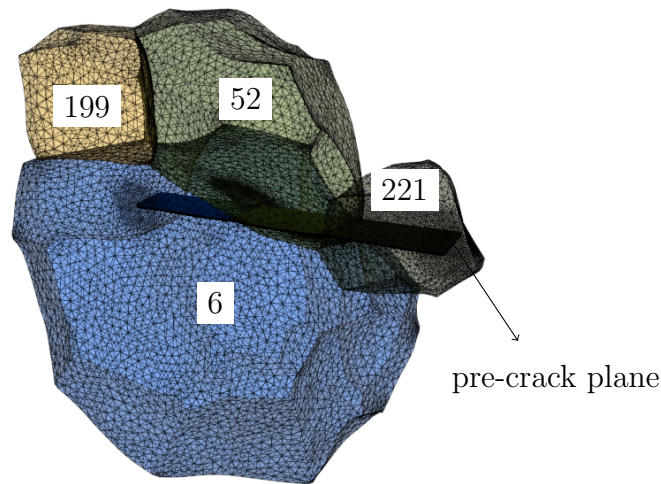
FIGURE 5.1: A front view of the three grains cut by the pre-crack in the FE mesh.
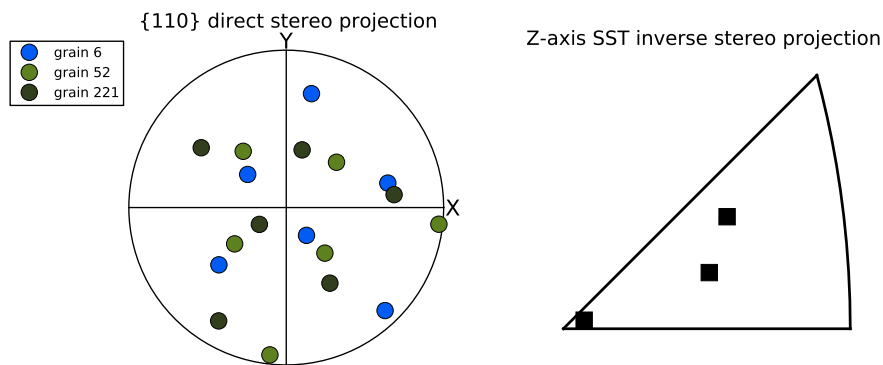
FIGURE 5.2: {110} pole figure of grain 6, grain 52 and grain 221.

For grain 6 and grain 52, the most easily activated slip system is $(\bar{1}01)[1\bar{1}1]$ that corresponds to system number 4 in Table 5.2 and for grain 221 it is $(011)[11\bar{1}]$ corresponding to system number 12 in Table 5.2.

Then, the polycrystal simulation with a pre-crack is carried out using the combination of linear and quadratic elements, see Chapter 2. A displacement of $U_3 = 1.65$ μm is imposed at the top surface as boundary conditions, which corresponds to a tensile load of 45 N. The loading amplitude is more severe than the experimental fatigue loading that is 40 N in order to increase the damage indicator and accelerate the crack propagation. Field transfer of the state variables are not
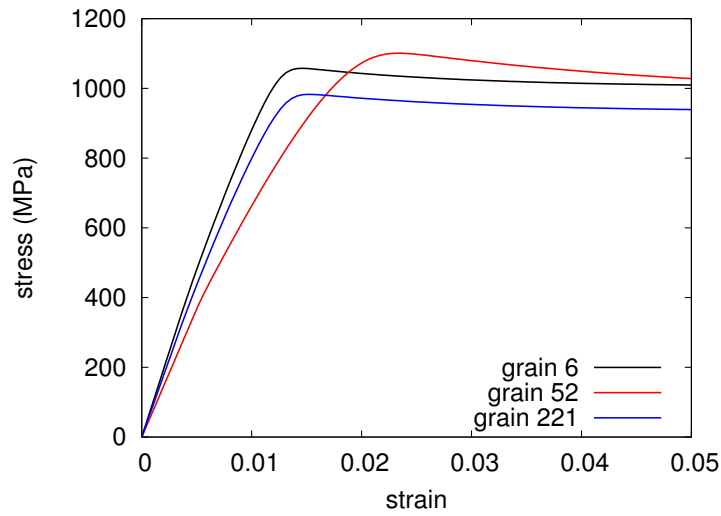
FIGURE 5.3: Axial stress σ_{zz} strain ε_{zz} curves of grain 6, grain 52 and grain 221.

system number	slip system	grain 6	grain 52	grain 221
1	$(\bar{1}\ 0\ 1)\ [1\ 1\ 1]$	0.052	0.381	0.350
2	$(0\ \bar{1}\ 1)\ [1\ 1\ 1]$	0.058	0.394	0.201
3	$(\bar{1}\ 1\ 0)\ [1\ 1\ 1]$	-0.006	-0.013	0.149
4	$(\bar{1}\ 0\ 1)\ [1\ \bar{1}\ 1]$	**0.461**	**0.431**	0.185
5	$(0\ 1\ 1)\ [1\ \bar{1}\ 1]$	0.165	0.395	0.150
6	$(1\ 1\ 0)\ [1\ \bar{1}\ 1]$	-0.296	-0.036	-0.035
7	$(0\ \bar{1}\ 1)\ [\bar{1}\ 1\ 1]$	0.372	0.415	0.445
8	$(1\ 1\ 0)\ [\bar{1}\ 1\ 1]$	-0.213	-0.033	-0.146
9	$(1\ 0\ 1)\ [\bar{1}\ 1\ 1]$	0.159	0.382	0.299
10	$(\bar{1}\ 1\ 0)\ [1\ 1\ \bar{1}]$	0.089	0.015	-0.260
11	$(1\ 0\ 1)\ [1\ 1\ \bar{1}]$	-0.355	-0.430	-0.236
12	$(0\ 1\ 1)\ [1\ 1\ \bar{1}]$	-0.266	-0.414	**-0.496**

TABLE 5.2: Schmid factor of grain 6, grain 52 and grain 221. The highest Schmid factors are highlighted.

performed from one crack propagation to the next due to numerical problem of the field transfert during parallel computation.

The accumulated plastic strain at the surface of the sample is shown in Figure 5.4. In this figure, the traces of slip planes of grain 6 at the left of the notch and of grain 221 at the right of the notch are drawn on a close up view of the notch tips. The corresponding values of the activated slip systems for the two grains are shown in Figure 5.5 (a) and Figure 5.6 (a). It can be observed that in grain 6 one slip band localises along the (101) plane, another slip band localises along a combination of
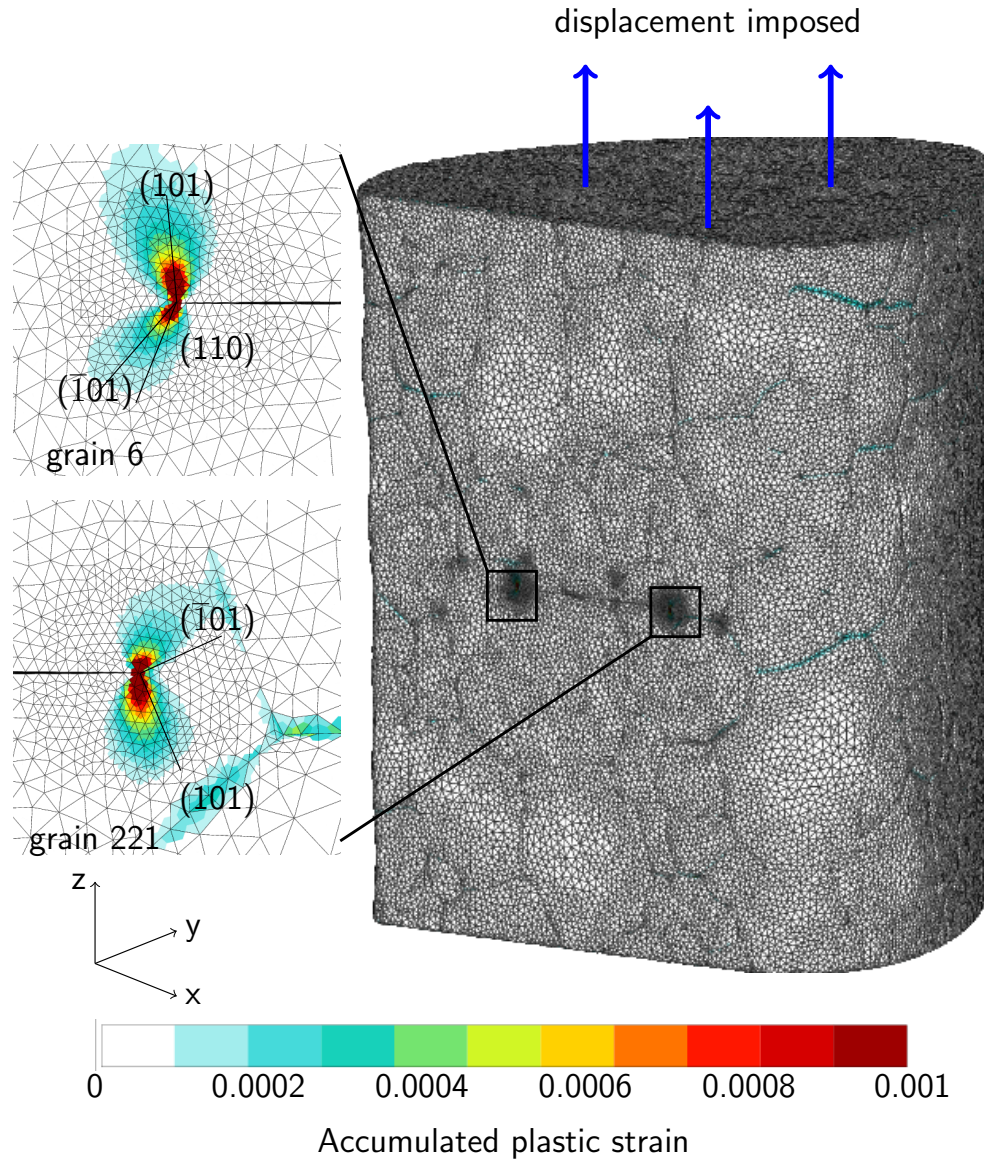
FIGURE 5.4: Accumulated plastic strain of the entire volume and a near front view at the notch tips.

($\bar{1}01$) and (110) slip planes, of which the ($\bar{1}01$) slip plane has the maximum Schmid factor. In grain 221, the slip localises mainly along a combination of (101) and (011) slip planes. In contrast, the ($\bar{1}01$) slip plane that has the maximum Schmid factor is hardly activated.

The above analysis shows that the slip activity and the mixed loading mode at the crack tip of the polycrystal is so complex that the Schmid factor calculated from uniaxial loading cannot predict the slip activation. Also, the presence of the initial crack which is a first order parameter makes the slip activation completely different. Moreover, there are other factors than the Schmid factor that influence
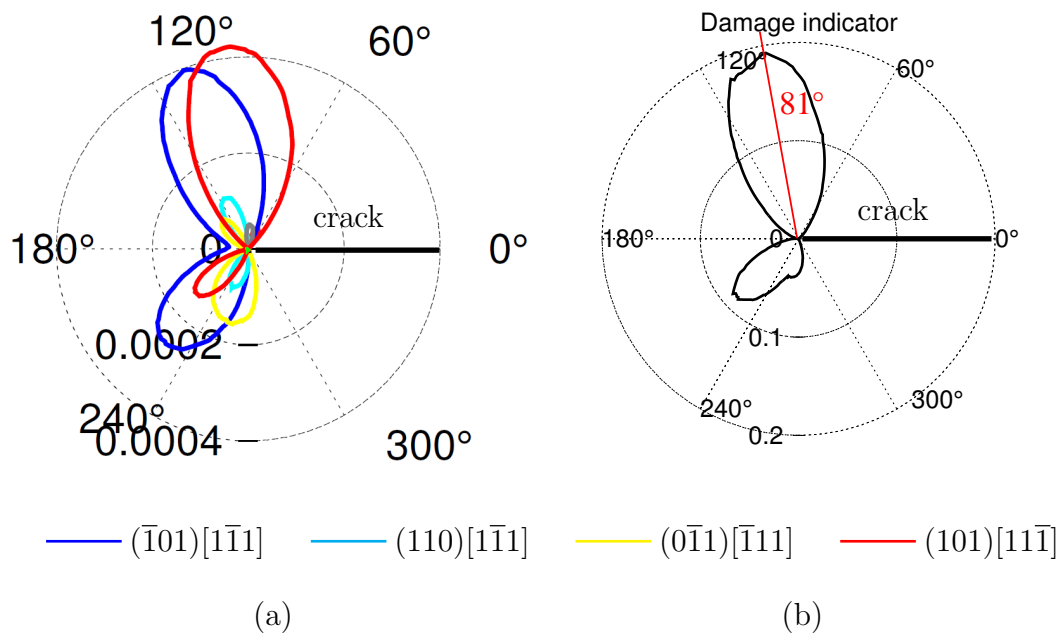
FIGURE 5.5: (a) The cumulated plastic strain of the 4 most activated slip systems and (b) the damage indicator value (in MPa) at a radius of 5 μm around the crack tip at the sample surface in grain 6.
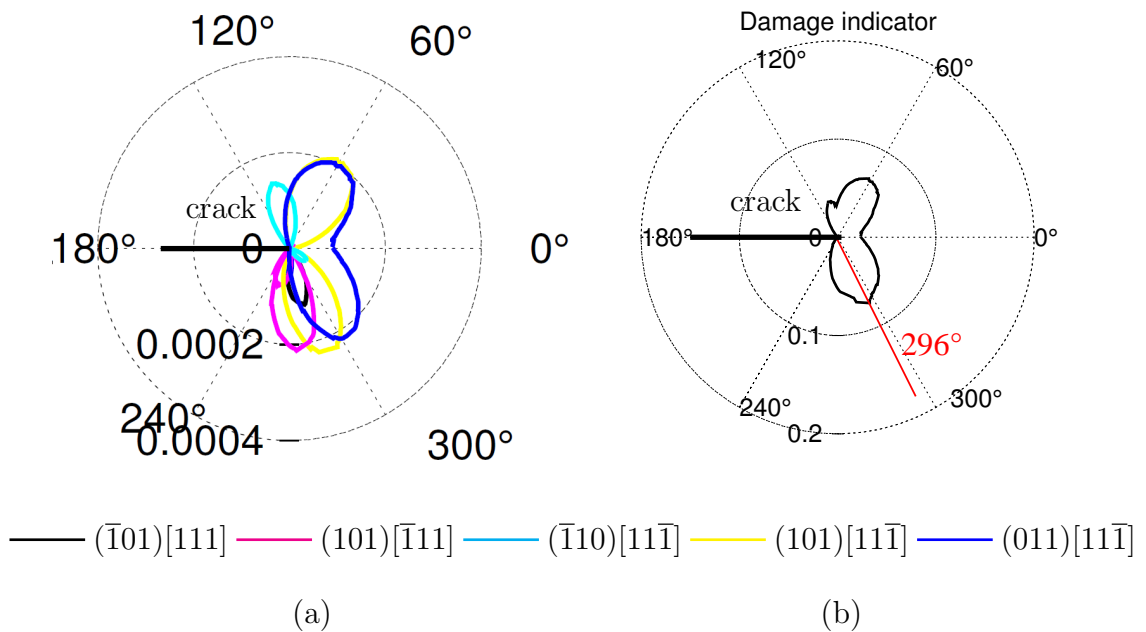
FIGURE 5.6: (a) The cumulated plastic strain of the 5 most activated slip systems and (b) the damage indicator value (in MPa) at a radius of 5 μm around the crack tip at the sample surface in grain 221.

slip activation in the grain of a polycrystal. These parameters are the elastic anisotropy, grain shapes and grain incompatibility, as mentioned in Chapter 1.

5.2   Evaluation of local crack growth rate

The damage indicator D with $k = 0.4$ in these two grains at a radius of 5 μm is shown in Figure 5.5 (b) and Figure 5.6 (b). The local crack propagation direction is determined, as explained in Chapter 4 in grain 6, as $\theta = 81°$ and as $\theta = 296°$ in grain 221. The variation of D is plotted along the direction of crack propagation over a distance R_b up to 20 μm from the crack tip, as shown in Figure 5.7. It can be observed that the values of D in grain 6 are higher than in grain 221 for R_b between 0 and 12 μm. For $R > 12$ μm from the crack tip, the values of D are very small and there is no obvious difference between the two grains.

The crack growth distance at each control point is determined by setting a critical damage indicator D_c, see Figure 5.7. Due to the fact that long computation time prevent us from simulating many cycles, the value of D_c is chosen to be small in order to propagate through a long distance at each step. However, it is also possible to simulate more precisely the crack growth direction with a series of small crack propagations by setting a larger value for D_c. Ultimately, this value can be determined experimentally by comparison with tomographic measurements. In this work, D_c is set to 0.1 MPa. The crack growth distance at the surface of grain 6 lies between $R = 8$ μm and $R = 5$ μm at surface of grain 221, which are equivalent to the crack growth distance at 10 000 cycles according to the *in-situ* experiment. This D_c value is applied to every control point along the crack front for each crack propagation step.

5.3   Results

A top view of the rectangular notch front and the corresponding cross section of the volume is shown in Figure 5.8 (a). The projected crack fronts after the first four crack propagation steps are shown in Figure 5.8 (b). It can be observed that the crack propagates from the notch at different rates. At the first step of crack growth (represented by the yellow line), the crack propagation at the notch
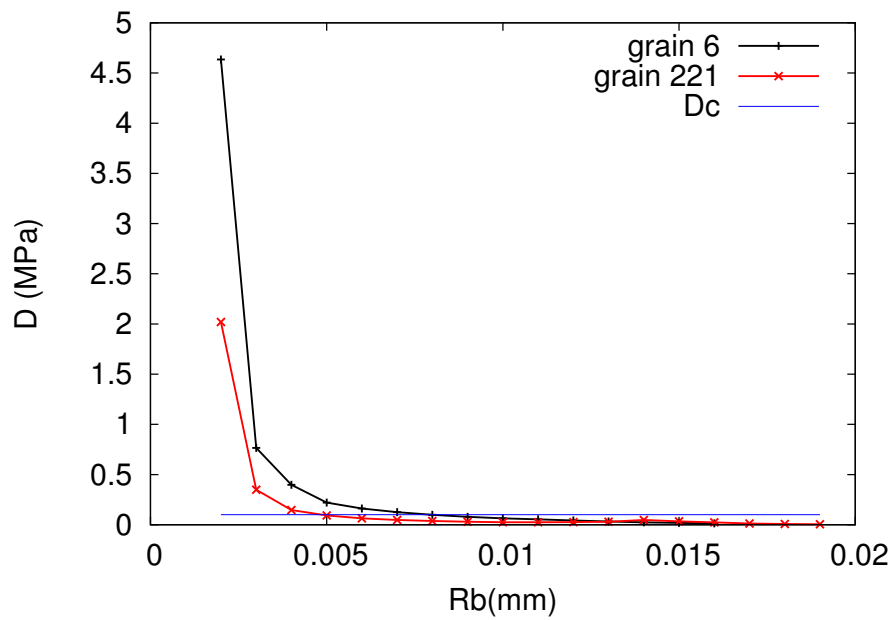
FIGURE 5.7: The damage indicator values just before the first crack propagation event along the direction of crack propagation in grain 6 (black line) and grain 221 (red line) as a function of the distance R_b from the crack tip.

corners appears more difficult with respect to that at the free surface. Because the corners of the rectangular notch represent protruding zones, a reduced driving force is expected at these particular locations. Then, from the second step of crack propagation, the crack grows all along the front. However, since everything is projected in the initial notch plane, the 3D crack shape and the grain boundary effects cannot be inferred from this figure.

Figure 5.9 shows the displacement field in the entire volume for the four propagation steps. The two crack tips at the sample surface are zoomed at the left and the right side of the Figure. In order to display the crack opening and the crack shape in the volume, the displacement has been magnified 50 times. It can be observed that the grain size at the left side of the pre-crack is larger than at the right size. The crack propagates upwards through grain 6 and crosses the boundary to enter grain 199.

Then, the crack surface and the corresponding grains are extracted from the volume mesh in Figure 5.10. The crack surface is colored with respect to the Standard Stereographic Triangle (SST) in order to describe the crystallographic planes with respect to different grain orientations. The black curves represent the grain boundaries. The crack propagates through about 20 µm from grain 6 to grain 199. At the
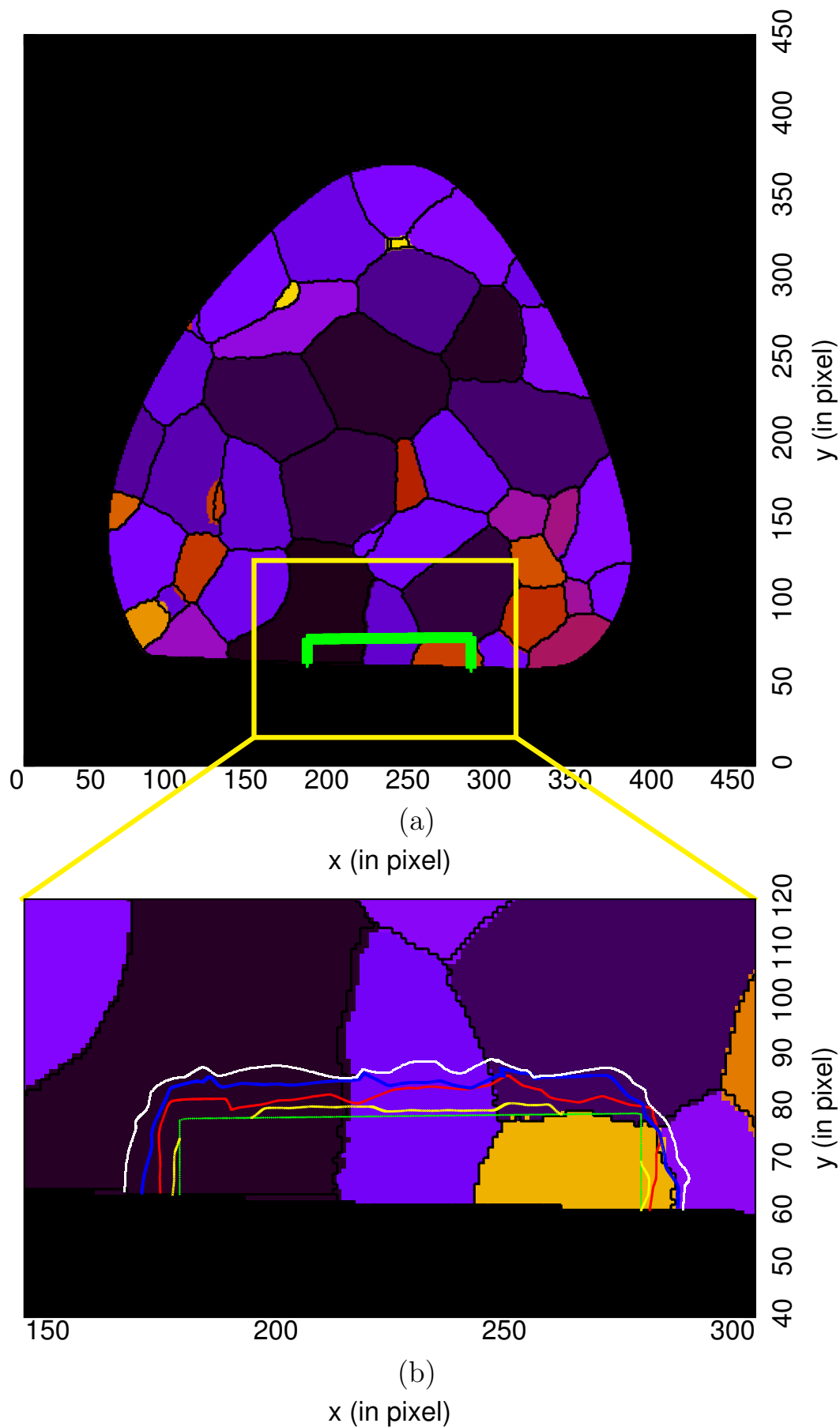
FIGURE 5.8: A top view of crack front at each step of crack propagation overlapping with the cross section of the volume.
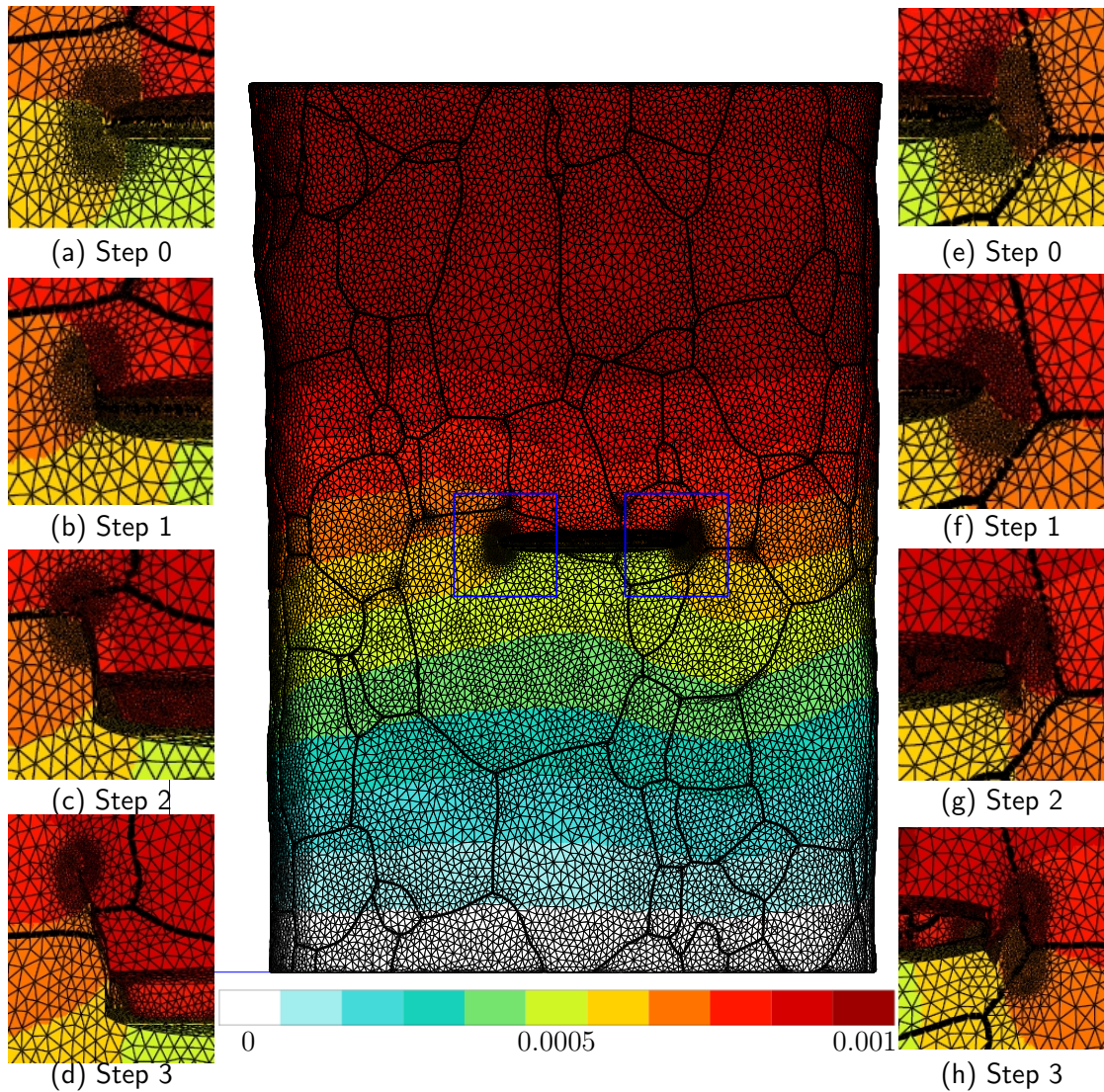
FIGURE 5.9: Displacement field magnified 50 times for the first three propagation steps.

sample surface, the direction of crack propagation changes progressively at each crack propagation event. At the end of the second crack growth step, the crack stops in front of the grain boundary. It propagates into grain 199 almost along the same direction which remains close to a (110) type crystallographic plane, see Figure 5.10 (a). A more detailed analysis of the crack plane in grain 6 will be given in Section 5.4. With increasing crack length, the crack growth direction at the sample surface changes progressively towards to 45° with respect to the globally applied load axis.

Inside grain 6, the direction of crack propagation varies from upwards to downwards at the two edges of the notch corner. Moreover, the values of the damage

indicator D inside grain 6 are smaller than at the surface. The results at different crack growth distances are shown in Figure 5.10 (a). Strong crack deflections take place at the grain boundaries between grain 6 and grain 52 and also between grain 52 and grain 221 because of the different grain orientations. The grain orientation effect is one of the characteristics of short crack propagation, as reviewed in Chapter 1.

In some cases, crack bifurcation also occurs within the grains from one step to the next propagation step. This can be observed in grain 221 that is at the right side of the pre-crack, in Figure 5.10 (b). The crack grows downwards for the first step, and goes upwards in the next step. This phenomenon is also observed inside grain 6 and grain 52, see arrows in Figure 5.10 (c). This crack bifurcation can be explained by several reasons: 1) The complex non symmetric grain orientation and the horizontal pre-crack induce the activation of several slip systems at the crack front. The competition of different activated slip systems at the crack front makes the selection of crack direction more difficult. This can be observed from the small difference of the damage indicator value at the crack front shown in Figure 5.6 (b) of grain 221. 2) The distance from the crack front to grain boundaries is small in grain 221. This small distance makes the influence of grain boundary and neighbor grains more significant. The effect of grain boundary will be discussed in the next section. 3) Only four cycles simulated and the small value of the selected damage indicator threshold D_c lead to a high sensitivity of the crack propagation direction.

5.4   Discussion

A quantitative analysis of the crack propagation parameters is carried out in this section. First, the average crack growth rates are calculated in two grains: grain 6 and grain 221. Then, the influence of the damage indicator and the role of normal stress on each system will be clarified. Next, the influence of grain boundaries on the crack growth rate and the crack deflections will be analysed. Finally, the simulated crack will be compared to the behaviour of the real crack imaged by X-ray tomography.
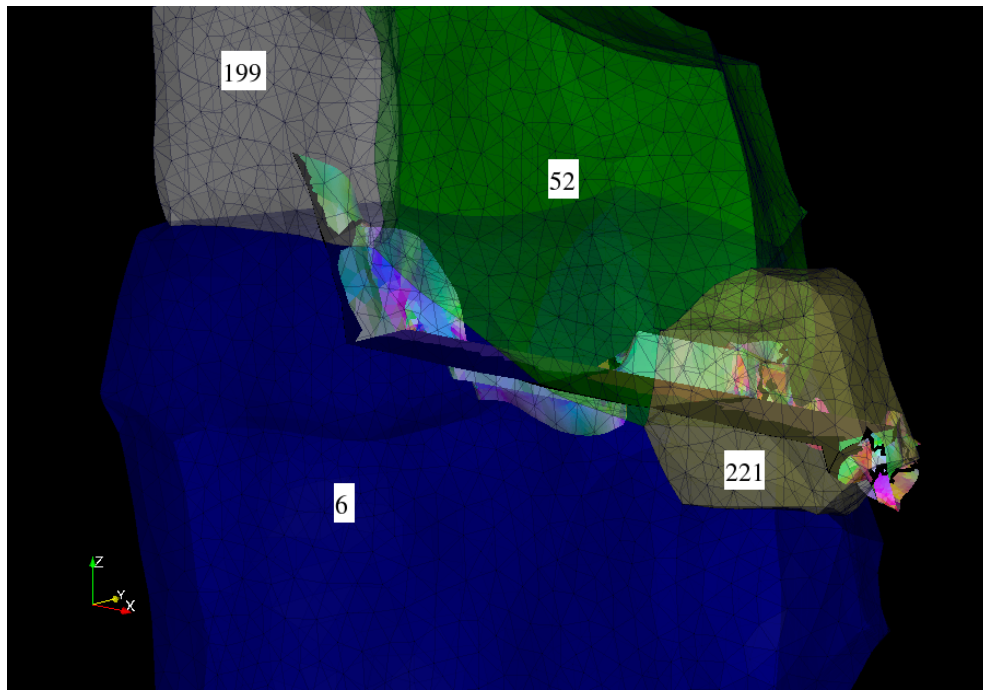
(a)
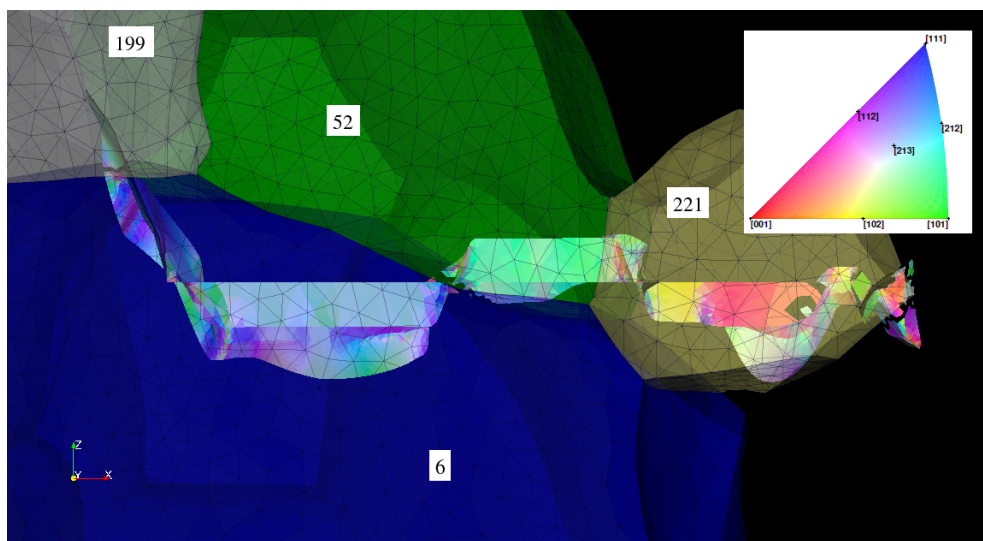
(b)
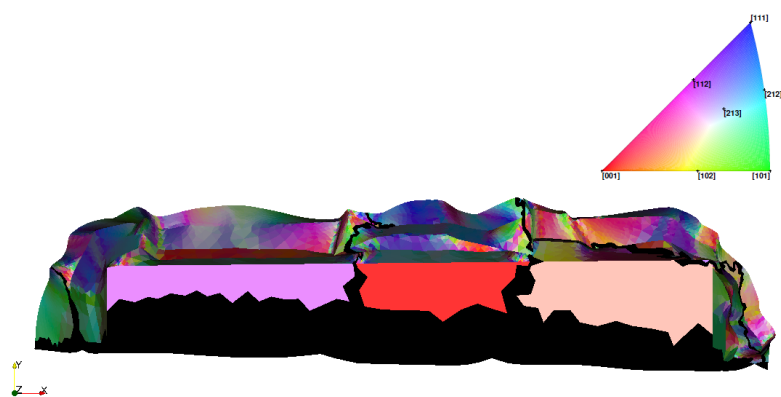
(c)

FIGURE 5.10: (a) Crack surface and the corresponding grains at the fourth step crack propagation, (b) front view, (c) top view. Black curves represent grain boundaries.

grain number	cycle 1	cycle 2	cycle 3	cycle 4
grain 6	8.8	9.3	10.3	8.5
grain 221	7.3	7.2	8.5	5.0

TABLE 5.3: Average growth rate (µm/cycle)

5.4.1 Crack growth rate

The average crack growth distance at each step, i.e. the crack growth rate da/dN, is calculated in grain 6 and 221, where the pre-crack is mainly located. There are seven control points at the crack front in grain 6 and in grain 221, respectively. The average crack growth distances in the two grains are determined by averaging the crack growth distance, as described in Chapter 4, at each of these control points in both grains. The results of the average crack growth rate da/dN and the crack growth distance of each control points as a function of the crack length are shown in Figure 5.11 with the values in Table 5.3. In the results, the crack length is assumed to be 0 for the pre-crack and is the sum of the average crack growth distances of each step N.

Figure 5.11 shows that da/dN in grain 6 is higher than in grain 221. This can also be observed in Figure 5.10 at the sample surface. The average crack growth rates are in the order of several microns per cycle. The difference of the crack growth rates can be due to the grain size, the pre-crack position with respect to the grain boundary and the grain orientation. From the top view of the crack surface in Figure 5.10 (c), it can be observed that the right side of the pre-crack front is close to the grain boundary of grain 221, that acts as a barrier against the crack propagation. The effects of grain boundary will be analysed in the next section.

As the crack becomes longer, da/dN increases slightly at the third step of crack propagation and then decreases. The variation of da/dN may be due to the complexity of the crack shape after the fourth crack growth event. However, the number of crack propagation steps is very limited to draw further conclusion on the crack growth rate.
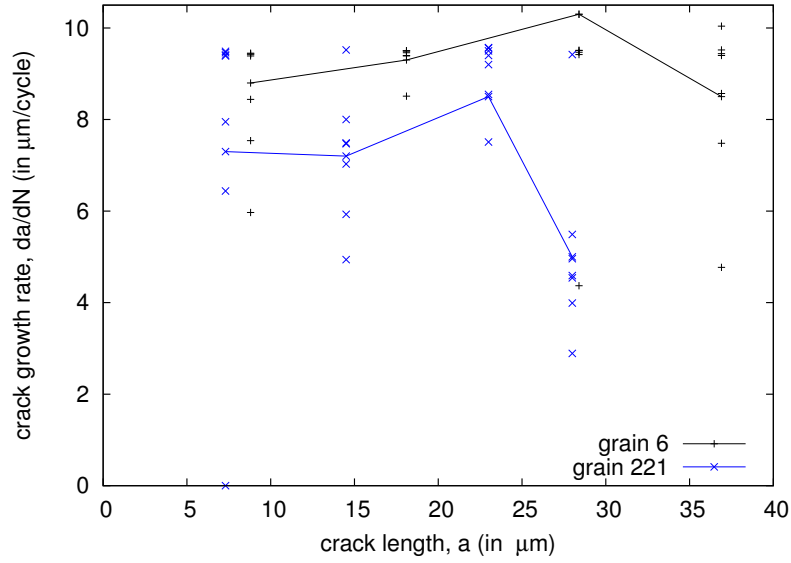
FIGURE 5.11: Average growth rate of grain 6 and grain 221.

5.4.2 Influence of grain boundaries

The effects of the grain boundary between grain 6 and grain 199 is analysed. The normal vector to this grain boundary is calculated as the average normal vectors to the grain boundary surface elements. The crack propagated along the (101) plane in grain 6 and the (101) plane in grain 199. The normal vectors of these planes are given in Table 5.4. The twist angle of crack plane deflection at the grain boundary is considered as the main factor to crack propagation through a grain boundary [Zhai *et al.*, 2005]. The detailed explanation and calculation of the twist angle calculation can be found in [Proudhon, 2005]. As a reminder, the twist angle α is

$$\cos\alpha = \frac{bb' + \eta^2 cc' + \xi^2 aa' - \eta\xi(a'c + ac')}{[b^2 + \eta^2 c^2 + \xi^2 a^2 - 2\eta\xi ac]^{0.5}[b'^2 + \eta^2 c'^2 + \xi^2 a'^2 - 2\eta\xi a'c']^{0.5}}, \qquad (5.2)$$

with a, b, c the components of the normal vector of grain 6 $\underline{N1}$, a', b', c' the components of the normal vector of grain 199 $\underline{N2}$ and η, ξ the first and the third components of the normal vector of the grain boundary $\underline{E}$. In Table 5.4, the second component of the normal vector of the grain boundary $\underline{E}$ is very small. In order to facilitate the calculation of twist angle of the two planes to their grain boundary, it is assumed to be zero.

$\underline{\textbf{E}}$	$\underline{\textbf{N1}}$ (grain 6)	$\underline{\textbf{N2}}$ (grain 199)
(-0.1043,-0.0449,0.9935)	(0.4578,-0.3282,0.8261)	(0.5542,-0.3249,0.7661)

TABLE 5.4: Normal vectors of grain boundary $\underline{\textbf{E}}$, of the (101) plane in grain 6 $\underline{\textbf{N1}}$ and of the (101) plane in grain 199 $\underline{\textbf{N2}}$, in the sample coordinate system.

$\underline{\textbf{N2}}_c$	$\underline{\textbf{N2}}_s$	α
(1,0,1)	(0.5542,-0.3249,0.7661)	3.98°
($\bar{1}$,0,1)	(-0.8297,-0.2869,0.4785)	128.49°
(0,1,1)	(-0.1831,0.3312,0.9254)	135.79°
(0,$\bar{1}$,1)	(-0.0923,-0.9230,0.3192)	62.33°
(1,1,0)	(0.6465,0.6181,0.4469)	73.18°
($\bar{1}$,1,0)	(-0.7374,0.6561,0.1593)	168.83°

TABLE 5.5: The plane normal in the crystal reference, $\underline{\textbf{N2}}_c$, in the sample reference, $\underline{\textbf{N2}}_s$, and the grain boundary twist angle α between grain 6 and the slip planes corresponding grain 199.

The crack plane twist angle at the grain boundary between the (101) plane of grain 6 and the (101) plane of grain 199 is calculated to be 3.98°. The twist angles of the other planes of grain 199 are also calculated in Table 5.5. It can be seen that the crack propagates along the plane that has a minimum twist angle.

After the first step of crack propagation, Figure 5.12 shows the damage indicator D at the sample surface of grain 6. First, a discontinuity of D is observed at the crack surfaces. It displays a high value, due to the complex slip activations at the crack tip. In order to facilitate the numerical resolution, D is evaluated through 270° around the crack tip, i.e. $\theta \in [45° : 315°]$, the 45° before and after the crack surfaces are not considered. The value of 45° is chosen after evaluation of the values of D at all sections perpendicular to the crack front. Second, Figure 5.12 shows that D is also high along the grain boundary because the plastic slip is affected by grain boundaries.

In order to study the role of grain boundary on the crack growth rate, crack propagations with different crack growth distances are simulated for the second step of crack propagation. Figure 5.13 shows the damage indicator of a 5 µm crack growth distance. When the crack gets close the grain boundary, the value of D increases significantly. This considerable D value can be explained by the incompatibility of the two neighbouring grains. As the crack propagates, D is transmitted to grain 199. Figure 5.14 (b) shows the damage indicator of a 10 µm crack growth distance. The direction of crack propagation changes from 81° to
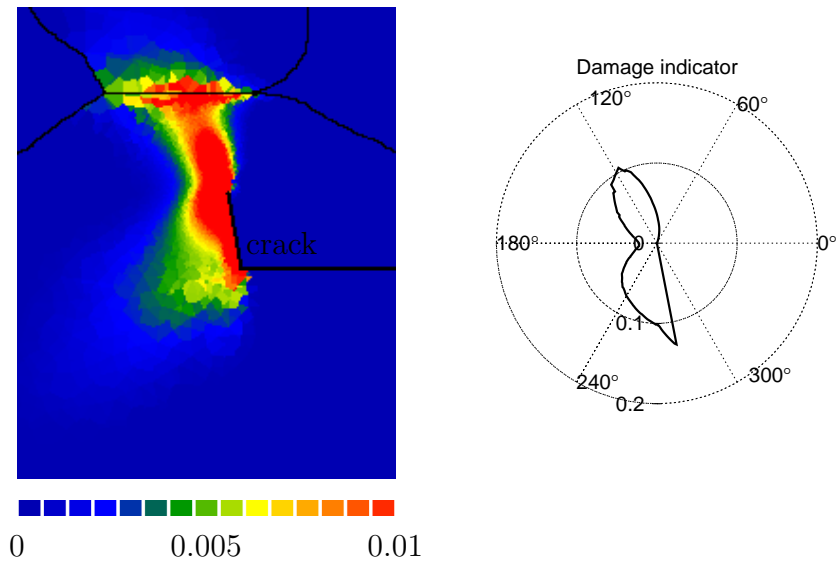
FIGURE 5.12: The damage indicator after the first step of crack propagation.
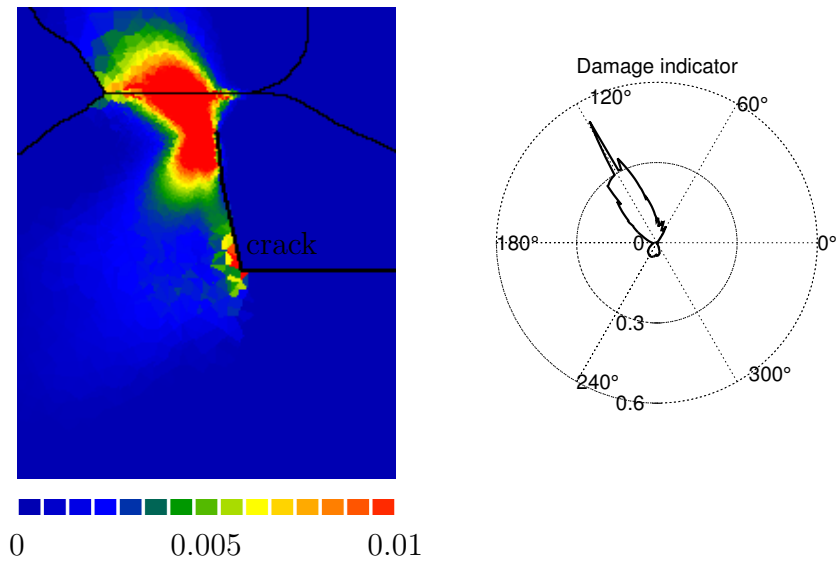
FIGURE 5.13: The damage indicator D (MPa) at the sample surface after the second step of 5 μm of crack propagation.

60° with respect to the pre-crack surface, at the next step in grain 199, as shown in Figure 5.14 (b), due to different slip system activation.

5.4.3 Influence of damage indicator on the direction of crack propagation

In the previous simulation, the damage indicator D, with $k = 0.4$, is used to compute the crack propagations. In this section, two different damage indicators
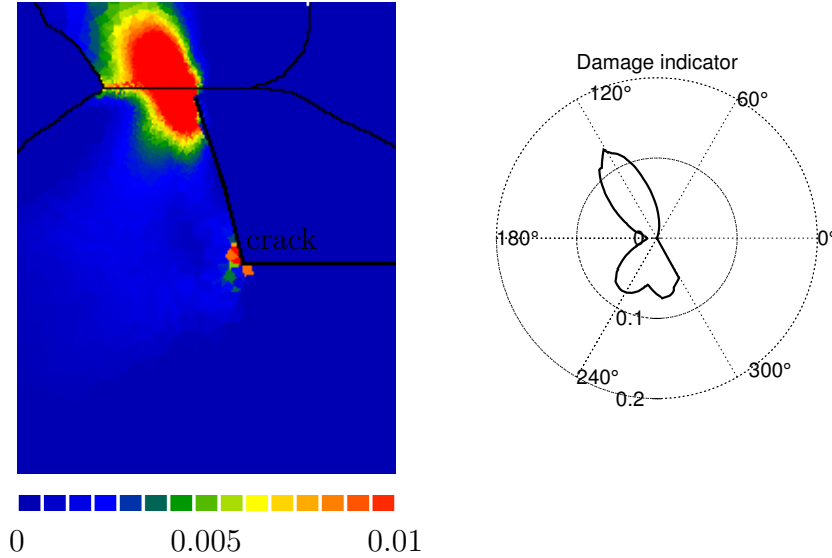
FIGURE 5.14: The damage indicator D (MPa) at the sample surface after the second step of 10 μm of crack propagation.

D_1 and D_2 are proposed in order to evaluate the influence of the normal stress and the accumulated slip on the direction of crack propagation. In D_1, the parameter of k in Equation 4.1 is set to $k = 10$, that gives a significant effect of the normal stress on the direction of crack propagation. In D_2, the accumulated slip is considered as the damage indicator. The equations of D_1 and D_2 are given as follows:

$$D_1(t) = \max_s \int_0^t |\dot{\gamma}^s|(|\tau^s| + 10 \times \langle \sigma_n^s \rangle) \mathrm{d}t, \tag{5.3}$$

$$D_2(t) = \max_s \int_0^t |\dot{\gamma}^s| \mathrm{dt} \tag{5.4}$$

Figure 5.15 shows the damage indicators D, D_1 and D_2 fields before the first step of crack propagation. In section 5.3, the crack propagates with D, along the direction of 81° with respect to the horizontal pre-crack plane. Due to the small value $k = 0.4$ in the damage indicator D, the normal stress of system s, σ_n^s, and the resolved shear stress of system s, τ^s, have about the same effect on the direction of the crack propagation. However, the fact that $\dot{\gamma}^s$ is a factor in Equation 4.1 makes the crack propagate only to where slip is activated. When increasing the effect of the normal stress of system s in D_1, whose direction is perpendicular to the slip direction, the crack will propagate along the direction of 72°. However, the accumulated slip D_2 shows that the crack will propagate along 82° with respect
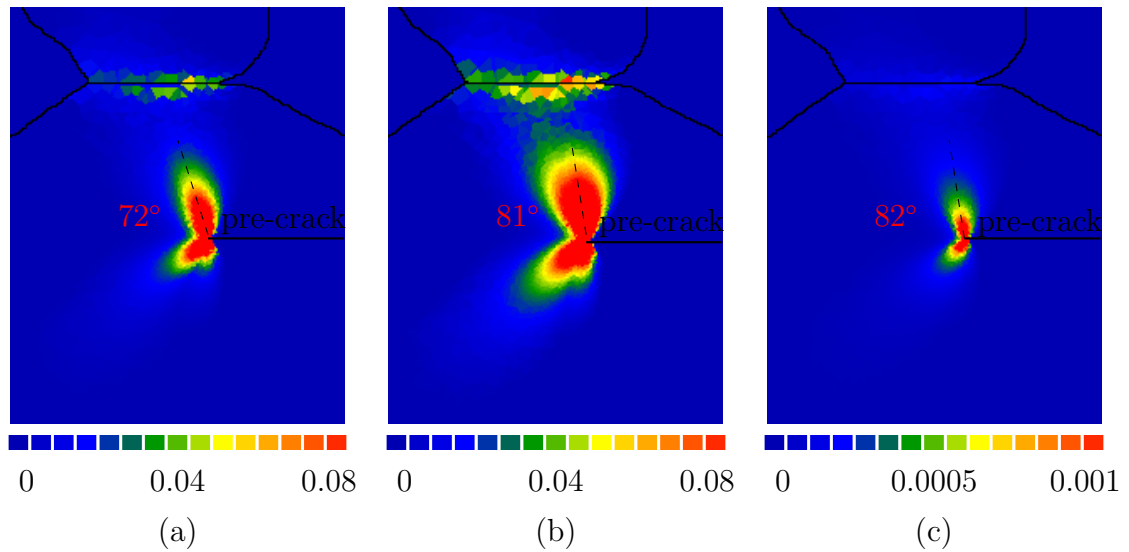
FIGURE 5.15: The damage indicators D (MPa) at the sample surface at the first step of crack propagation (a) D_1, in which $k = 10$, (b) D, in which $k = 0.4$, (c) D_2: the accumulated slip.
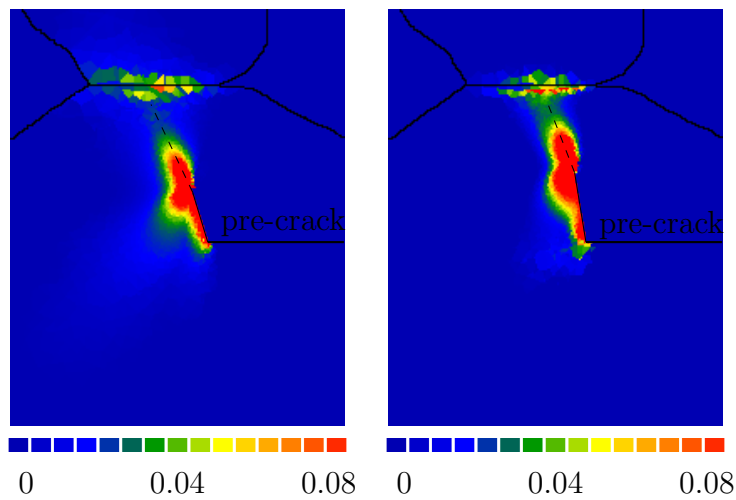
FIGURE 5.16: The damage indicators and the crack growth direction of the second step of crack propagation (a) D_1, in which $k = 10$, (b) D with $k = 0.4$.

to the pre-crack plane, at only 1° difference with the direction of D. Therefore, the contribution of the normal stress of system s may change a few degrees of the crack growth direction only.

Figure 5.16 shows the damage indicator fields and the crack growth direction after the first step of crack propagation according to D_1 and D, respectively. The simulation of crack propagation with D_1 was performed only one event. From the comparaison of the first step crack growth simulations with D and D_1, it can be highlighted that the damage indicator plays an important role in the direction of

the first step of crack propagation. For the further steps of crack propagation, it remains almost the same direction with that of the first step.

5.4.4 Comparison with X-ray tomographic experiments

The *in-situ* fatigue experiments were presented in Chapter 1. The final state of the experimental crack at 129500 cycles is recalled in Figure 5.17 (a). The crack surface colors represent the different grains through which the crack propagates and the grain boundaries are represented in black. In Figure 5.17 (b), the simulated crack after the fourth step propagation is also colored by grain number. Both cracks propagate more easily in grain 6, at left hand side of the pre-crack. However, the experimental crack in grain 6 grows along a direction of 225° with respect to the pre-crack while the simulated crack grows along a direction of 72°. Moreover, the experimental crack in grain 6 presents a significant deflection of crack surface from (101) slip plane type to (112) slip plane type, see Figure 1.4 (b). This crack deflection does not appear in the simulation.

Figure 5.18 (a) shows the 3D experimental crack at 38000 cycles. In grain 6, the crack propagation distance is not the same along the crack front. The crack along the (112) plane type and near the sample surface propagates more easily and then arrest ahead of the grain boundary in Figure 5.18 (b). In the simulation crack in Figure 5.17 (b), the different crack growth distance at the sample surface and in the sample are also simulated. However, the concave crack surface will be difficult to simulate, because the normal vectors of control points may intersect and then induce a hole at the crack surface.

The difference of crack propagation direction between simulation and experiment may be due to many reasons. The main reasons are: i) The dimensions of the fatigue sample are very small, which makes the alignment of the fatigue machine difficult. The misalignment of the fatigue experiment can influence directly the direction of fatigue crack propagation. This could be verified by measuring the elastic strain tensors during the experiment or by applying a digital volume correlation on the tomographic images. The crack deflection in grain 6 of the experimental crack may be simulated by using a polycrystal mesh by inserting an intermediate step of experimental crack, or by using the real boundary conditions determined by the strain tensor analysis. ii) The damage indicator D is a plastic slip dominated

damage indicator. The formulation of D induces that crack grows only to directions with high plastic slip. The distance of the crack tip to the grain boundary and the misorientation of grain boundaries are not directly incorporated in the damage indicator. The barrier effects of grain boundary change the damage indicator only through the plastic slip field. In the current simulation, the crack tip in grain 6 has two potential directions of propagation. The direction of 72° is closer to the grain boundary between grain 6 and grain 199. The slip accumulated along this direction and the the plastic slip activated by the barrier effect of the grain boundary help the crack propagates to the direction of 72° with respect to the pre-crack plane. iii) The displacement amplitude in the simulation is more severe than the experimental displacement, due to the time consuming nature of fatigue simulations. The fact that crack propagates with the larger monotonic amplitude loading could lead to more slip systems activated at the crack tip. Moreover, the crack closure, i.e. contact conditions between the crack tips, have not been taken into account by this method. iv) The state variables field transfer was not carried out in the present simulation due to the local D_c value chosen. The field transfert can influence the crack bifurcation from one step to the next, as shown in the red grain of Figure 5.17.

Conclusions

The present simulation method of crack propagation is applied to a real polycristal with an initial pre-crack. The plasticity of the grains around the pre-crack is analysed before the simulation of crack propagation. Then, a critical damage indicator is chosen and the local crack growth rate is defined. Four steps of crack propagation are simulated. The results showed different crack growth directions in the different grains around of the crack. The average crack growth rate in each grain is also analysed showing that the crack grows faster on well oriented (110) planes and crosses grain boundary more easily when the twist angle α is low, reproducing some experimental trends. The influence of grain boundary and of the damage indicator on crack growth direction is discussed. Finally, a comparison between the experimental crack propagation and the simulated crack propagation was carried out. The differences between experiment and simulation crack were analysed.
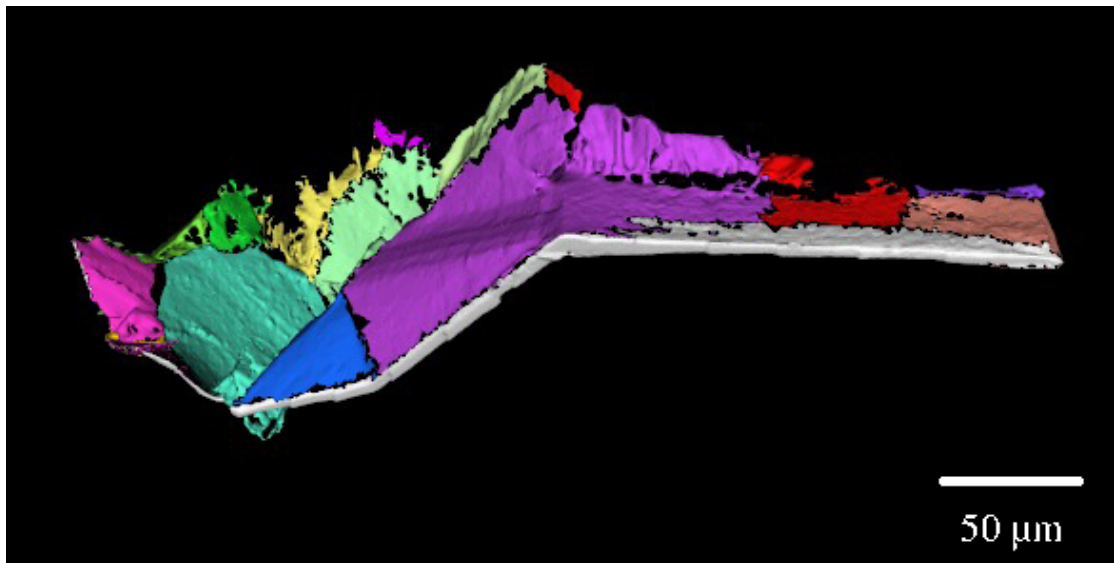
(a)
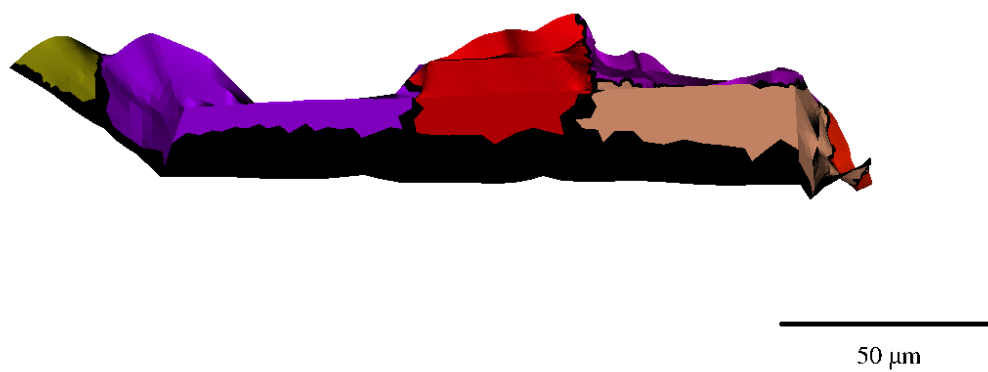
(b)

FIGURE 5.17: (a) The fatigue crack at 129500 cycles characterised by X-ray tomography. (b) The simulated crack at fourth step of crack propagation.
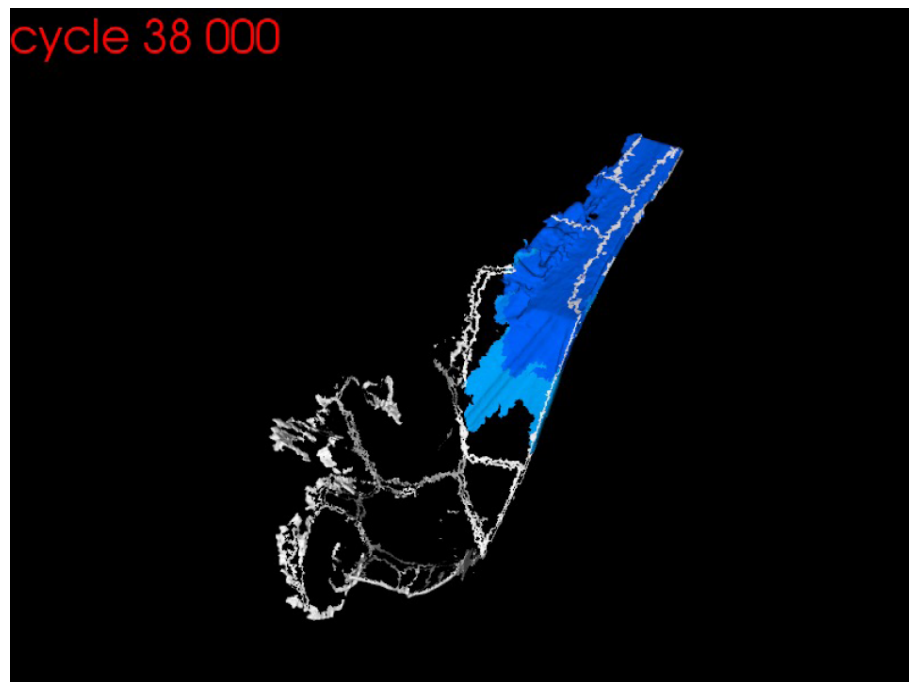
(a)
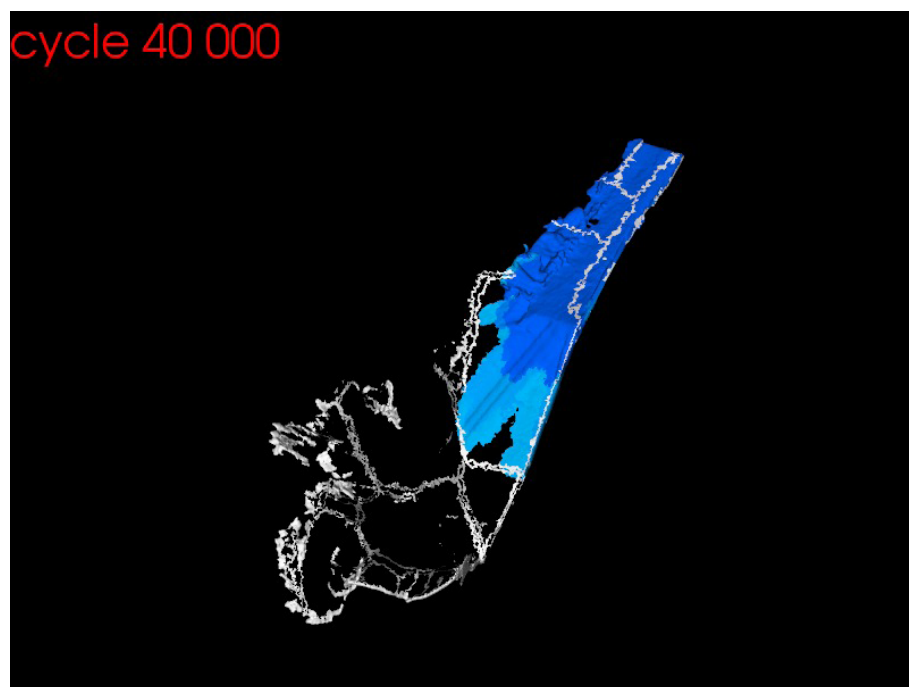
(b)

FIGURE 5.18: The fatigue crack at (a) 38000 cycles, (b) 40000 cycles.

Conclusions

L'approche de simulation de la propagation de fissure est appliquée à un polycristal réel pré-fissuré. Les activités plastiques dans les grains autour de front de fissure ont été analysées. Ensuite, une valeur critique de l'indicateur d'endommagement et la vitesse locale de propagation ont été définies. La fissure est propagée en quatre étapes. Les résultats montrent que les directions de propagation sont différentes dans les grains autour du front fissure. L'analyse de la vitesse moyenne de propagation à chaque grain montre que la fissure propage plus vite sur les plans bien orientés (110). Elle traverse le joint de grain plus facilement quand l'angle twist α est petit, ce qui correspondent à la tendance expérimentale. L'influence de joint de grains et l'indicateur d'endommagement sur la direction de propagation est discutée. Enfin, la comparaison entre simulation et expérimental fissure est effectuée. Les différences entre ces fissures sont analysées.

Chapter 6

Conclusions and outlook

The objective of this thesis was to understand numerically the main driving force of short fatigue crack propagation in a real polycrystal using the Crystal Plasticity Finite Element method. The Ph.D. work was developed in two parts:

- simulation of a real uncracked pure titanium polycrystal behaviour reconstructed from a stack of X-ray tomographic images

- simulation of short fatigue crack propagation in a real Ti55531 polycrystal through remeshing and comparison with the experimental crack propagation

X-ray tomographic characterisation was carried out at the ESRF before the Ph.D. work started. Two methods were used successively in order to characterise the crack propagation in the polycrystal. Diffraction Contrast Tomography (DCT) was performed in the pure titanium and the titanium alloy polycrystal samples to obtain grain shape, grain orientation and average elastic strain tensor in each grain. The pure titanium polycrystal is a cylindrical sample of 648 µm in diameter and 423 µm in height. The titanium alloy polycrystal is a prismatic cross section sample with a rectangular pre-crack. Then, the Phase Contrast Tomography (PCT) was used to characterise the short fatigue crack propagation in the pre-cracked titanium alloy polycrystal sample.

Two real microstructural meshes were reconstructed from the X-ray tomographic images, using Avizo and Ghs3d software. The mesh of the cylindrical sample in pure titanium was generated to analyse the anisotropic elastic behaviour. This

mesh contains 1392 grains, 3.85 million tetrahedral elements and 1.98 million degrees of freedom, with an average element size of 10 μm. An elastic compression test was simulated for this mesh with the grain orientation measured by DCT. Different boundary conditions were studied. The grain by grain comparison between the simulated mean elastic strain tensors and the exprimental ones measured by DCT was sucessfully performed. The comparison showed that the computational $\Delta\varepsilon_{33}$ component of strain tensors with the real boundary conditions was consistent with the experimental strain measurements.

The mesh of the prismatic titanium alloy sample was reconstructed in order to simulate the short fatigue crack propagation. A rectangular pre-crack was inserted thereafter. The position of the pre-crack was measured from the absorption images. This mesh contains 5 million elements, 6.1 million degrees of freedom and the minimum element size at the crack tip is about 1 μm. Only the elements in the region around the crack tip are quadratic element in order to reach a compromise between the computation time and the accuracy of simulation.

The constitutive equations are the classical crystal plasticity law with isotropic hardening and kinematic hardening. The elasto-visco-plastic material parameters of the titanium alloy Ti55531 were identified by a set of mechanical tests: a tensile test and strain-controlled and stress-controlled cyclic tests. Parallel computations were adapted to the quadratic elements around the crack tip and linear elements in other regions of the mesh. This approach was used both for parameter identification and crack propagation simulations.

A new method for simulation of 3D crack propagation in single crystals and polycrystals was proposed, based on CPFE computations. A damage indicator that is a combination of the accumulated slip, the resolved shear stress and the normal stress on each slip system was calculated for every time increment of CPFE simulation. This damage indicator was analysed at a distance around the crack tip in order to determine the local crack growth direction. According to a preset critical damage indicator value, the crack growth distance was also calculated. The crack was extended via remeshing at each crack propagation step. The state variables transfer was carried out in the single crystals. The crack in the realistic polycrystal was propagated in four steps. The field transfer was not taken into account in the polycrystal simulation. The simulated crack was compared to the experimental crack characterised by the X-ray tomography. The influence of grain boundary, crack growth rate, damage indicator has been discussed.

The main advantages of this crack growth simulation method are:

- the effects of microstructure in terms of grain shape, grain orientation and grain boundary are considered,

- crystal plasticity constitutive law can be applied,

- crack propagates across grain boundaries,

- local crack growth direction and crack growth rate are determined,

- the computing time is essentially the CPFE simulation time,

- the damage indicator can easily be changed to study effects of other parameters.

However, there are also some drawbacks. First, the simulation of crack propagation is time consuming, although with parallel computing it takes about 12 hours for one step crack growth. One axis for improvement would be model reduction [Ryckelynck *et al.*, 2011]. Also, the propagation of multiple cracks may be difficult numerically when they cross paths. Because the crack propagates to where the damage indicator is maximum. However, when this field of one crack intersects other crack, this method will not distinguish which field belongs to which crack. Moreover, crack branching is not possible with the current algorighm. It is limited by the maximation damage indicator process in which only one maximum damage indicator is determined for crack propagation. The intergranular crack propagation is also difficult to be simulated since there is no grain boundary mesh and grain boundary properties in the model.

Outlook

The three years of the PhD project are extremely short to study short fatigue crack propagation, such a complicated and interesting subject. It would be interesting to continue in the following directions. i) For the crack growth simulation of the single crystals, a confrontation with single crystal crack propagation experiments [Liu *et al.*, 2008] would be directly carried out. This would help identify the local crack growth driving force through the damage indicator. The crack shape in single crystals is less complex than in a polycrystal, because there is neither

grain boundary nor neighboring grain effect. The crack growth path and the local crack growth rate will be simulated and compared to the experimental ones. ii) The model of crack propagation can be run automatically for multithreading computations until the whole structure is broken. It remains to be automated for parallel computation. iii) The simulation method of crack growth can be used to a realistic 3D polycrystal with a properly identified constitutive law. Comparisons between numerical and experimental crack may help to establish a more sophisticated criterion for fatigue crack propagation than the one proposed in the present work.

Conclusions et perspectives

L'objectif de cette thèse consiste à étudier numériquement les éléments moteurs pour la propagation des fissures courtes dans un polycristallin en utilisant la simulation par éléments finis en plasticité cristalline. Le travail s'est développé selon deux axes:

- La simulation sans fissure d'un polycristal réel de titane pur reconstruit à partir des images tomographiques

- La simulation de la propagation d'une fissure courte de fatigue dans un polycristal de Ti55531 par le biais de remaillage et comparaison avec la fissure expérimentale

La caractérisation par tomographie aux rayons X a été réalisée à l'ESRF au sein du projet CRYSTAL en parallèle de ce travail. Deux méthodes ont été utilisées successivement pour caractériser la propagation de fissure dans le polycristal. Tomographie par Contraste de Diffraction (DCT) a été effectuée dans les deux éprouvettes (en titane pur et en alliage Ti55531) afin d'obtenir la forme et l'orientation de grains. Avec l'éprouvette en titane pur de la section cylindrique, de 648 μm en diamètre, le tenseur de déformation élastique moyenné dans chacun des grains a été mesurés. Avec l'éprouvette en alliage de titane 55531, la propagation de fissure a été caractérisée *in-situ* par Tomographie en Contraste de Phase (PCT).

Deux maillages réels avec des grains ont été reconstruits à partir des images tomographiques, grâce à une procédure mise en place dans ce travail. Le maillage de titane pur est utilisé pour étudier l'anisotropie de déformation élastique. Il contient 1392 de grains, 3.85 million d'éléments tetraèdres et 1.98 million de degrées de liberté, avec une taille d'éléments moyenne de 10 μm. Un essai de compression a été simulté pour ce maillage avec l'orientation de grains mesurée par DCT. Les

différentes conditions aux limites ont également été étudiées. La comparaison grain par grain des tenseurs de déformations élastiques entre simulation et expérience a montrée une très bonne cohérence.

Le maillage de l'éprouvette pré-fissurée en alliage Ti55531 est utilisé pour simuler la propagation de fissure courte en fatigue. La position de la pré-fissure est obtenue d'après les images d'absorption. Ce maillage contient 5 million d'éléments, 6.1 million de degrées de liberté, avec une taille d'éléments minimale au voisinage de front de fissure de 1 μm. Afin de parvenir à un compromis entre le temps et la précision de calcul, seul les éléments autour de front de fissure sont quadratiques.

Les lois de comportement sont les lois classiques de plasticité cristalline avec écrouissage isotrope et cinématique. Les paramètres élasto-visco-plastique du matériau Ti55531 ont été identifiés par des essais de traction et des essais cycliques avec déformation imposée et contrainte imposée. Les calculs en parallèle ont été adaptés pour ce maillage ayant à la fois les éléments linéaires et quadratiques. Cette approche a été appliquée à la simulation de la propagation de fissure et l'identification des paramètres du matériau.

Pour simuler la propagation de fissure en 3D dans les monocristaux et les polycristaux, une nouvelle méthode de simulation par éléments finis en plasticité cristalline a été proposée. Un indicateur d'endommagement combinant le glissement cumulé, la cission résolue et la contrainte normale sur chaque système de glissement a été calculé à tous les incréments de calcul. L'analyse de cet indicateur d'endommagement autour du front de fissure permet de calculer la direction et la distance de propagation en chaque point de control. La fissure se propage par remaillage à chaque étape de propagation. Lors de cette étape il est possible de tranférer les champs de plasticité sur le nouveau maillage pour simuler le sillage plastique de la fissure. La fissure simulée est ensuite comparée avec la fissure expérimentale obtenue par tomographie aux rayons X. L'effet de joint de grains, la vitesse locale de propagation de la fissure, l'indicateur d'endommagement ont été discuté.

Les principaux avantages de cette approche de simulation de propagation de fissure sont:

- les effets de la microstructure en termes de forme, d'orientation et de caractères des joints de grains rencontrés par la fissure sont pris en compte,

- les lois de comportement de plasticité cristalline peuvent être appliquées,

- la fissure peut se propager sur des distances de l'ordre de quelques tailles de grains et donc franchit des joints de grains,

- la direction locale et la vitesse de propagation de fissure sont déterminées par le calcul,

- la forme de l'indicateur d'endommagement peut être modifié facilement pour étudier d'autres mécanismes.

Néanmoins, cette approche présente également des limites. Premièrement, le calcul de propagation de fissure est coûteux en temps, bien que le temps soit réduit à 12 heures pour une étape avec le calcul en parallèle. Un axe d'amélioration pour diminuer le temps de calcul pourrait être la réduction de modèle [Ryckelynck *et al.*, 2011]. La propagation de multi-fissures semble difficile numériquement quand les chemins se croisent, puisque la méthode ne distingue pas à quelle fissure se repère le champ de l'indicateur d'endommagement. Par ailleurs, le branchement de fissure ne peut pas être simulé par cette méthode, car la maximation de l'indicateur d'endommagement limite la propagation de fissure à une seule direction. De plus, la fissuration intergranulaire reste encore difficile puisque des joints de grains n'ont pas de comportement particulier dans ce modèle.

Perspectives

Ce travail de thèse est consacré au développement d'une nouvelle approche pour simuler la propagation de fissure couplée avec le calcul en CPFE. Il serait intéressant d'appliquer ou améliorer dans les directions suivantes. i) Une expérience de propagation de fissure dans un monocristal a été réalisée par [Liu *et al.*, 2008]. Une confrontation avec la simulation serait possible pour identifier l'élément moteur de propagation de fissure dans l'indicateur d'endommagement. La forme de fissure dans les monocristaux est moins complexe que dans les polycristaux car l'influence de joint de grains et de grains au voisinage de la fissure n'interviennent pas. ii) Le modèle de propagation a été automatisé pour le calcul en multithreads, avec lequel la simulation de la propagation dans le monocristal (Chapitre 4) peut être lancée jusqu'à la structure rompue. Il sera utile d'automatiser également pour le calcul en parallèle (Chapitre 5) car certaines tâches restent encore manuelles aujourd'hui.

Appendix A

Parallel computing adaptation

A.1 Mesh partitioning

The Z-set inputfile for mesh partitioning contains the following commands:

```
****    mesher
 ***    mesh
  **    metis_split
   *    domains number
   *    weight_by_nodes
   *    check_domains
   *    check_domains_iter number
   *    parallel_cut_files
****    return
```

**metis_split: indicates the METIS mesh partitioning.

*domains: specifies the number of sub-domains to be used. $number = 32$ in the example.

*weight_by_nodes: assigns a weight factor to quadratic elements for the combined linear and quadratic mesh.

*check_domains: indicates that the domains should be checked to see whether there are elements attached by less than one edge or a face.

*check_domains_iter: indicates the number of iterations for the check_domains procedure. *number* = 50 in the example.

*parallel_cut_files: write a parallel cut file.

A.2 Parallel computations

The Z-set inputfile contains (among others) the following commands related to the parallelism:

```
****    calcul
 ***    linear_solver mumps
  **    sequential
 ***    feti
  **    keep_direction 1000
  **    precision 1.e-9
  **    max_iteration 1000
  **    reprojection
  **    precond lumped
  **    projector direct
```

***linear_solvers mump: specifies that the solver to be used is MUMPS.

**sequential: modification for the present project in order to use MUMPS as a sequential local solver within the FETI solver in parallel mode.

**feti: specifies FETI as the iterative parallel solver.

**keep_direction: gives the number of orthogonal descent directions retained during the (Conjugate Gradient) CG iterations.

**precision: defines the relative precision required for convergence when solving the interface problem with the CG method. This number is a measure of the maximum norm of the displacement jump across the domain interfaces which can be accepted in a converged solution. This number depends on the number of DOF at the domain interfaces.

**max_iteration: is the maximum iterations when solving the interface problem.

**reprojection: can significantly reduce the number of FETI iterations, when used in conjunction with quasi-Newton schemes of tangent matrix update (such as eeeeee or p1p1p1, see the **algorithm command in the Z-set documentation).

**precond lumped: specifies that the type of pre-conditioning used to accelerate CG convergence is lumped here.

**projector direct: uses the direct Gauss solver to solve the sub-domain problem.

A.2.1 Example of parallel job for cluster

The following script is used to run the parallel computation on the computing cluster (through the batch system):

```bash
#!/bin/bash

####################################################################
# Job Name                                                         #
####################################################################
#$ -N "calcul_quad"

####################################################################
# Send mail when jobs starts and finishes:                        #
# 'b' : Mail is sent at the beginning of the job.                 #
# 'e' : Mail is sent at the end of the job.                       #
# 'a' : Mail is sent when the job is aborted or rescheduled.      #
# 's' : Mail is sent when the job is suspended.                   #
####################################################################
#$ -M jia.li@mat.ensmp.fr

####################################################################
# Use current working directory                                   #
####################################################################
#$ -cwd

####################################################################
# Join stdout and stderr                                          #
####################################################################
#$ -j y

####################################################################
# Declare job re-runnable                                         #
####################################################################
#$ -r y

####################################################################
# Run job through bash shell                                      #
####################################################################
#$ -S /bin/bash

####################################################################
# Queue definition                                                #
####################################################################
#$ -q 256G.q

####################################################################
# Resource reservation                                            #
# -R = reservation : yes                                          #
# -l mem_free : we need at minimum 60G per node                   #
# -l h_fsize=400G : files can not be greeter than 400 GB          #
####################################################################
#$ -R y
#$ -l mem_free=60G
#$ -l h_fsize=400G

####################################################################
# Parallel jobs with Open MPI                                     #
# -pe mpi_rr : round robin parallel environment : 100 SLOTS       #
####################################################################
#$ -pe  mpi_rr 100

####################################################################
# Loading modules (zebulon, sge, openmpi, gcc, parallel_tools)    #
####################################################################
. /etc/profile.d/modules.sh
module load zebulon/Z8.5-acml sge  openmpi gcc open64 parallel_tools

####################################################################
# Parameters of the calculation                                   #
####################################################################
export NP=100
export INP="calcul_quad"
export TMPCALCUL=/home/scratch/${LOGNAME}/${JOB_ID}
export RESULTS=${SGE_O_WORKDIR}/${JOB_ID}
export HOSTFILE=${RESULTS}/pe_hostfile
```

```
export ACML_FAST_MALLOC=1
export OMP_NUM_THREADS=1
export NTHREAD=1

export OPAL_PREFIX=${Z7EXTRALIBS}/${Z7MACHINE}/mpi
export PATH=${OPAL_PREFIX}/bin:${PATH}
export LD_LIBRARY_PATH=${OPAL_PREFIX}/lib:${LD_LIBRARY_PATH}
export ZEBU_PATH=~/MUMPS2

# Creating the temporary and result directories
mkdir -p $TMPCALCUL
mkdir -p $RESULTS

# Copying the files we need (if this is needed) otherwise using
# current directory
cp    ${INP}.inp ${RESULTS}/
cp -r ${INP}-pcu*  ${RESULTS}/
cp -r ${INP}.cu* ${RESULTS}/
cp -r ${INP}-pmeshes ${RESULTS}/
cp    ${INP}.geo* ${RESULTS}/

echo
echo "Files in the directory ${RESULTS}:"
echo ls ${RESULTS}/
echo

####################################################################
# Creating the file zebulon needs to run with mpi                  #
####################################################################
echo "****z_server"              >  ${RESULTS}/server_calcul.inp
echo " ***parallel      mpmd"    >> ${RESULTS}/server_calcul.inp
echo "  **compute_nodes $NP"     >> ${RESULTS}/server_calcul.inp
echo "  **compute_hosts 1"       >> ${RESULTS}/server_calcul.inp
echo "    $NP any $TMPCALCUL"    >> ${RESULTS}/server_calcul.inp
echo "  **launch"                >> ${RESULTS}/server_calcul.inp
echo "    -default $INP"         >> ${RESULTS}/server_calcul.inp
echo "****return"                >> ${RESULTS}/server_calcul.inp

####################################################################
# Creating a hostfile with the right hostnames in it               #
####################################################################
make_hostfile.py < ${SGE_JOB_SPOOL_DIR}/pe_hostfile > $HOSTFILE
# sed -e "s/=32/=8/g" $HOSTFILETMP > $HOSTFILE

cd $RESULTS

# Running the mesher
# Zrun -m $INP > ${JOB_NAME}.${JOB_ID}.mesher.txt 2>&1

# Running Zebulon in //
mpirun -hostfile $HOSTFILE -np 1 -host localhost
${Z7PATH}/calcul/Zebulon_cpp_${Z7MACHINE} -s MPI mpi2 -PP
server_calcul.inp > ${JOB_NAME}.${JOB_ID}.calcul.txt 2>&1

# Glueing the calcul
sed s/-default/-glue/ server_calcul.inp > server_glue.inp
mpirun -hostfile $HOSTFILE -np 1 -host localhost
${Z7PATH}/calcul/Zebulon_cpp_${Z7MACHINE} -s MPI mpi2 -PP
server_glue.inp > ${JOB_NAME}.${JOB_ID}.glue.txt 2>&1

# Running post-process
Zrun -pp $INP > ${JOB_NAME}.${JOB_ID}.post.txt 2>&1

# Cleaning the temporary directory
rm -rf $TMPCALCUL
```

Bibliography

Ackermann, F., Kubin, L., Lepinoux, J. and Mubhrabi, H. [1984], 'The dependence of dislocation microstructure on plastic strain amplitude in cyclically strained copper single crystals', *Acta Metallurgica* **32**, 715–725.

Amestoy, P., Duff, L., L'Excellent, J.-Y. and Koster, J. [2001], 'Mumps: A general purpose distributed memory sparse solver', *Applied Parallel Computing. New Paradigms for HPC in Industry and Academia, Lecture Notes in Computer Science* **1947**, 121–130.

Asaro, R. [1975], 'Elastic–plastic memory and kinematic–type hardening', *Acta Metallurgica* **23**, 1255–1265.

Asaro, R. [1983], 'Crystal plasticity', *Journal of Applied Mechanics* **50**, 921–934.

Asaro, R. and Rice, J. [1977], 'Strain localization in ductile single crystals', *Journal of the Mechanics and Physics of Solids* **25**, 309–338.

Aslan, O. and Forest, S. [2009], 'Crack growth modelling in single crystals based on higher order continua', *Computational Materials Science* **45**, 756–761.

Avizo [version 7], http://www.vsg3d.com/avizo.

Barbe, F., Forest, S. and Cailletaud, G. [2001], 'Intergranular and intragranular behavior of polycrystalline aggregates. part 2: Results', *International Journal of Plasticity* **17**, 537–563.

Barenblatt, G. [1962], 'The mathematical theory of equilibrium cracks in brittle fracture', *Advances in ammplied mechanics* pp. 55–129.

Basquin, H. [1910], 'The exponential law of endurance tests', *Proc. ASTM* **10**, 625–630.

Becker, R. and Panchanadeeswaran, S. [1989], 'Crystal rotations represented as Rodrigues vectors', *Textures and Microstructures* **10**, 167–194.

Belytschko, T. and Black, T. [1999], 'Elastic crack growth in finite elements with minimal remeshing', *International Journal for Numerical Methods in Engineering* **45**, 601–620.

Belytschko, T., Gracie, R. and Ventura, G. [2009], 'A review of extended/generalized finite element methods for material modeling', *Modelling and Simulation in Materials Science and Engineering* **17**, 1–24.

Bennett, V. and McDowell, D. [2003], 'Polycrystal orientation distribution effects on microslip in high cycle fatigue', *International Journal of Fatigue* **23**, 27–39.

Besson, J. and Foerch, R. [1997], 'Large scale object oriented finite element code design', *Computer Methods in Applied Mechanics and Engineering* **142**, 165–187.

Bilby, B., Cottrell, A. and Swinden, K. [1963], 'The spread of plastic yield from a notch', *Proceedings of the Royal Society A* **272**, 304–314.

Buffière, J.-Y., Ferrie, E., Proudhon, H. and Ludwig, W. [2006], 'Three-dimensional visualisation of fatigue cracks in metals using high resolution synchrotron x-ray micro-tomography', *Materials Science and Technology* **22**, 1019–1024.

Castelluccio, G. M., Musinski, W. D. and McDowell, D. L. [2014], 'Recent developments in assessing microstructure-sensitive early stage fatigue of polycrystals', *Current Opinion in Solid State and Materials Science* **18**, 180–187.

Cazzani, A. and Rovati, M. [2003], 'Extrema of young's modulus for cubic and transversely isotropic solids', *International journal of solids and structures* **40**, 1713–1744.

Chandra, N., Li, H., Shet, C. and Ghonem, H. [2002], 'Some issues in the application of cohesive zone models for metal–ceramic interfaces', *International Journal of Solids and Structures* **39**, 2827–2855.

Cheng, A. and Laird, C. [1983], 'The transition from stage i to stage ii fatigue crack propagation in copper single crystals cycled at constant strain amplitudes', *Materials Science and Engineering* **60**, 177–183.

Chiaruttini, V., Feyel, F. and Chaboche, J.-L. [2010], 'A robust meshing algorithm for complex 3d crack growth simulations', *IV European Conference on Computational Mechanics, Paris, France* .

Chiaruttini, V., Geoffroy, D., Riolo, V. and Bonnet, M. [2012], 'An adaptive algorithm for cohesive zone model and arbitrary crack propagation', *European Journal of Computational Mechanics* **21**, 208–218.

Chiaruttini, V., Riolo, V. and Feyel, F. [2013], 'Advanced remeshing techniques for complex 3d crack propagation', *13th International Conference on Fracture, Beijing, China* .

Cignoni, P., Montani, C. and Scopigno, R. [1998], 'A comparison of mesh simplification algorithms', *Computation and Graphics* **22**, 37–54.

Cloetens, P., Pateyron-Salome, M., Buffière, J., Peix, G., Baruchel, J., Peyrin, F. and Schlenker, M. [1997], 'Observation of microstructure and damage in materials by phase sensitive radiography and tomography', *Journal of Applied Physics* **81**, 5878–1886.

Coffin, L. [1954], 'A study of the effects of cyclic thermal stresses on a ductile metal', *Transactions ASME* **76**, 931–950.

Dang Van, K., Cailletaud, G., Flavenot, J., Douaron, A. L. and Lieurade, H. [1989], 'Criterion for high cycle fatigue failure under multiaxial loading', *Biaxial and Multiaxial Fatigue, Edited by M.W. Brown and K.J. Miller* pp. 459–478.

Destuynder, P., Djaoua, M. and Lescure, S. [1983], 'Quelques remarques sur la mécanique de la rupture élastique', *Journal de mecanique théorique et appliquée* **2**, 113–135.

Dingley, D. and Pond, R. [1979], 'On the interaction of crystal dislocations with grain boundaries', *Acta Metallurgica* **27**, 667–682.

Doquet, V. [1999], 'Micromechanical simulations of microstructure-sensitive stage i fatigue crack growth', *Fatigue & Fracture of Engineering Materials & Structures* **22**, 215–223.

Dugdale, D. [1960], 'Yielding of steel sheets containing slits', *Journal of the Mechanics and Physics of Solids* **8**, 100–104.

Edwards, L. and Zhang, Y. [1994], 'Investigation of small fatigue cracks–ii. a plasticity based model of small fatigue crack growth', *Acta Metallurgica et Materialia* **42**, 1423–1431.

Elices, M., Guinea, G., Gómez, J. and Planas, J. [2002], 'The cohesive zone model: advantages, limitations and challenges', *Engineering Fracture Mechanics* **69**, 137–163.

Farhat, C. and Roux, F. [1991], 'A method of finite element tearing and interconnecting and its parallel solution algorithm', *International Journal for Numerical Methods in Engineering* **32**, 1205–1227.

Fatemi, A. and Socie, D. [1988], 'A critical plane approach to multiaxial fatigue damage including out-of-phase loading', *Fatigue & Fracture of Engineering Materials & Structures* **11**, 149–165.

Flouriot, S., Forest, S. and Rémy, L. [2003], 'Strain localization phenomena under cyclic loading: application to fatigue of single crystals', *Computational Materials Science* **26**, 61–70.

Forsyth, P. [1963], 'Fatigue damage and crack growth in aluminium alloys', *Acta Metallurgica* **11**, 703–715.

Fréour, S., Lacoste, E., Francois, M. and Guillen, R. [2011], 'Determining ti-17 beta-phase single crystal elasticity constans through X-ray diffraction and inverse scale transition model', *Materials Science Forum* **681**, 97–102.

George, P. and Borouchaki, H. [1997], *Triangulation de Delaunay et maillage: application aux éléments finis*, Editions HERMES, Paris.

George, P., Borouchaki, H., Frey, P., Laug, P. and Saltel, E. [2004], *Mesh Generation and Mesh Adaptivity: Theory and Techniques, Encyclopedia of Computational Mechanics*, Vol. 1: Fundamentals, Chap. 17, Wiley InterScience.

Ghs3d [version 3.2-3], https://www.rocq.inria.fr/gamma/gamma/ghs3d.

Gordon, R., Bender, R. and Herman, G. [1970], 'Algebraic reconstruction techniques (art) for three-dimensional electron microscopy and X-ray photography', *Journal of Theoretical Biology* **29**, 477–481.

Groeber, A. and Jackson, A. [2014], 'DREAM.3D: A digital representation environment for the analysis of microstructure in 3D', *Integrating Materials and Manufacturing Innovation* **3:5**.

Guèye, I., Arem, S. E., Feyel, F., Roux, F.-X. and Cailletaud, G. [2011], 'A new parallel sparse direct solver: Presentation and numerical experiments in large-scale structural mechanics parallel computing', *International Journal for Numerical Methods in Engineering* **88**, 370–384.

Guéziec, A. [1997], 'Surface simplification inside a tolerance volume', *Research report, RC 20440, I.B.M. T.J.Watson Research Center* .

Hasegawa, T., Yakou, T. and Kocks, U. [1986], 'Forward and reverse rearrangements of dislocations in tangled walls', *Materials Science and Engineering* **81**, 189–199.

Herbig, M. [2011], 3D Short Fatigue Crack Investigation in Beta Titanium Alloys using Phase and Diffraction Contrast Tomography, PhD thesis, INSA Lyon.

Herbig, M., King, A., Reischig, P., Proudhon, H., Lauridsen, E., Marrow, J., Buffière, J.-Y. and Ludwig, W. [2011], '3-d growth of a short fatigue crack within a polycrystalline microstructure studied suing combined diffraction and phase-contrast x-ray tomography', *Acta Materialia* **59**, 590–601.

Héripré, E., Dexet, M., Crépin, J., Gélébart, L., Roos, A., Bornert, M. and Caldemaison, D. [2007], 'Coupling between experimental measurements and polycrystal finite element calculations for micromechanical study of metallic materials', *International Journal of Plasticity* **23**, 1512–1539.

Hill, R. [1965], 'Continuum micro-mechanics of elastoplastic polycrystals', *Journal of the Mechanics and Physics of Solids* **13**, 89–101.

Hounsfield, G. [1973], 'Computerized transverse axial scanning (tomography): Part i. description of system', *British Journal of Radiology* **46**, 1016–1022.

Karypis, G. and Kumar, V. [1998], 'Multilevel algorithms for multi-constraint graph partitioning', *Technical Report 98-019, University of Minnesota, Department of Computer Science* .

Korsunsky, A., Dini, D., Dunne, F. and Walsh, M. [2007], 'Comparative assessment of dissipated energy and other fatigue criteria', *International Journal of Fatigue* **29**, 1990–1995.

Krupp, U. [2007], *Fatigue crack propagation in metals and alloys. Microstructural aspects and modelling concepts*, WILEY-VCH.

Labiche, J.-C., Mathon, O., Pascarelli, S., Newton, M., Ferre, G., Curfs, C., Vaughan, G., Homs, A. and Carreiras, D. [2007], 'The fast readout low noise camera as a versatile x-ray detector for time resolved dispersive extended x-ray absorption fine structure and diffraction studies of dynamic problems in materials science, chemistry, and catalysis', *Review of Scientific Instruments* **78**, 091301.

Laird, C. and Smith, G. [1962], 'Crack propagation in high stress fatigue', *Philosophical Magazine* **7**, 847–857.

Lemaitre, J., Chaboche, J.-L., Benallal, A. and Desmorat, R. [2009], *Mécanique des Matériaux Solides*, third edn, Dunod.

Li, J., Proudhon, H., Roos, A., Chiaruttini, V. and Forest, S. [2014], 'Crystal plasticity finite element simulation of crack growth in single crystals', *Computational Materials Science* **94**, 191–197.

Liu, L., Husseini, N., Torbet, C., Kumah, D., Clarke, R., Pollock, T. and Jones, J. [2008], 'In situ imaging of high cycle fatigue crack growth in single crystal nickel-base superalloys by synchrotron x-radiation', *Journal of Engineering Materials and Technology* **130**.

Llanes, L., Rollett, A., Laird, C. and Bassani, J. [1993], 'Effect of grain size and annealing texture on the cyclic response and the substructure evolution of polycrystalline copper', *Acta Metallurgica et Materialia* **41**, 2667–2679.

Ludwig, W., King, A., Herbig, M., Reischig, P., Marrow, J., Babout, L., Lauridsen, E., Proudhon, H. and Buffière, J.-Y. [2010], 'Characterization of polycrystalline materials using synchrotron x-ray imaging and diffraction techniques', *JOM* **62**, 22–28.

Ludwig, W., King, A., Reischig, P., Herbig, M., Lauridsen, E., Schmidt, S., Proudhon, H., Forest, S., Cloetens, P., du Roscoat, S. R., Buffière, J., Marrow, T. and Poulsen, H. [2009], 'New opportunities for 3d materials science of polycrystalline materials at the micrometre lengthscale by combined use of x-ray diffraction and x-ray imaging', *Materials Science and Engineering A* **524**, 69–76.

Luther, T. and Konke, C. [2009], 'Polycrystal models for the analysis of intergranular crack growth in metallic materials', *Engineering Frature Mechanics* **76**, 2332–2343.

Lutjering, G. and Williams, J. [2007], *Engineering Materials and Processes, Titanium, Second Edition*, Springer.

Mandel, J. [1972], *Plasticité classique et viscoplasticité*, CISM Courses and Lectures No. 97, Udine, Springer Verlag, Berlin.

Manson, S. [1953], 'Behavior of materials under conditions of thermal stress', *Technical Note 2933, NACA* .

Marchal, N. [2006], *Propagation de fissure en fatigue-fluage à haute température de superalliages monocristallins à base de nickel*, Ph.D. thesis, ENSMP.

Martin, G. [2012], *Numerical multiscale simulation of the mechanical behavior of beta–metastable titanium alloys Ti5553 and Ti17*, Ph.D. thesis, ENSMP.

Martin, T. and Koch, A. [2006], 'Recent developments in x-ray imaging with micromieter spatial resolution', *Journal of Synchrotron Radiation* **13**, 180–194.

McDowell, D. and Dunne, F. [2010], 'Microstructure-sensitive computational modeling of fatigue crack formation', *International Journal of Fatigue* **32**, 1521–1542.

Méric, L., Poubanne, P. and Cailletaud, G. [1991], 'Single crystal modeling for structural calculations: Part 1 – model presentation', *Journal of Engineering Materials and Technology* **113**, 162–170.

Moës, N. and Belytschko, T. [2002], 'Extended finite element method for cohesive crack growth', *Engineering Fracture Mechanics* **69**, 813–833.

Morrow, J. [1968], *Fatigue design handbook, Advances in Engineering*, Society of Automotive Engineers.

Mughrabi, H., Herz, K. and Stark, X. [1981], 'Cyclic deformation and fatigue behaviour of α-iron mono- and polycrystals', *International Journal of Fracture* **17**, 193–220.

Mughrabi, M. [1978], 'The cyclic hardening and saturation behaviour of copper single crystals', *Materials Science and Engineering* **33**, 207–223.

Navarro, A. and de Los Rios, E. [1988], 'Short and long fatigue crack growth: A unified model', *Philosophical Magazine A* **57**, 15–36.

Neumann, P. [1969], 'Coarse slip model of fatigue', *Acta Metallurgica* **17**, 1219–1225.

Newman, J. [1998], 'The merging of fatigue and fracture mechanics concepts: a historical perspective', *Progress in Aerospace Sciences* **34**, 347–390.

Petry, W., Heiming, A., Trampenau, J., Alba, M., Herzig, C., Schober, H. and Vogl, G. [1991], 'Phonon dispersion of the bcc phase of group-iv metals. i. bcc titanium', *Physical Review B* **43**.

Proudhon, H. [2005], *Identification des mécanismes de fissuration dans un alliage d'aluminium sollicité en fretting et en fatigue*, Ph.D. thesis, INSA-Lyon.

Proudhon, H., LI, J., Reischig, P., Guéninchault, N., Forest, S. and Ludwig, W. [2015], 'Coupling diffraction contrast tomography with the finite element method', *Advanced Engineering Materials* . accepted.

Raabe, D., Sachtleber, M., Zhao, Z., Roters, F. and Zaefferer, S. [2001], 'Micromechanical and macromechanical effects in grain scale polycrystal plasticity experimentation and simulation', *Acta Materialia* **49**, 3433–3441.

Rannou, J., Gravouil, A. and Baïetto-Dubourg, M. C. [2009], 'A local multigrid x-fem strategy for 3-d crack propagation', *International Journal for Numerical Methods in Engineering* **77**, 581–600.

Rice, J. [1987], 'Tensile crack tip fields in elastic-ideally plastic crystals', *Mechanics of Materials* **6**, 317–335.

Ryckelynck, D., Benziane, D. M., Cartel, S. and Besson, J. [2011], 'A robust adaptive model reduction method for damage simulations', *Computational Materials Science* **50**, 1597–1605.

Schaef, W. and Marx, M. [2012], 'A numerical description of short fatigue cracks interacting with grain boundaries', *Acta Materialia* **60**, 2425–2436.

Schaef, W., Marx, M., Vehoff, H., Heckl, A. and Randelzhofer, P. [2011], 'A 3-d view on the mechanisms of short fatigue cracks interacting with grain boundaries', *Acta Metallurgica* **59**, 1849–1861.

Scheider, I. and Brocks, W. [2003], 'Simulation of cup–cone fracture using the cohesive model', *Engineering Fracture Mechanics* **70**, 1943–1961.

Simmons, G. and Wang, H. [1971], 'Single crystal elastic constants and calculated aggregate properties', *MIT Press* .

Simonovski, I. and Cizelj, L. [2011], 'Automatic parallel generation of finite element meshes for complex spatial structures', *Computational Meterials Science* **50**, 1606–1618.

Simpleware [n.d.], http://www.simpleware.com.

Sukumar, N., Moes, N., Moran, B. and Belytschko, T. [2000], 'Extended finite element method for three-dimensional crack modelling', *International Journal for Numerical Methods in Engineering* **48**, 1549–1570.

Suresh, S. [1998], *Fatigue of materials*, second edn, Cambridge University Press.

Tanaka, K., Akiniwa, Y., Nakai, Y. and Wei, R. [1986], 'Modelling of small fatigue crack growth interacting with grain boundary', *Engineering Fracture Mechanics* **24**, 803–819.

Thompson, N., Wadsworth, N. and Louat, N. [1956], 'The origin of fatigue fracture in copper', *Philosophical Magazine* **1**, 113–126.

Winter, A. [1974], 'A model for the fatigue of copper at low plastic strain amplitudes', *Philosphical Magazine* **30**, 719–738.

Wu, Z. and Sullivan, J. [2003], 'Multiple material marching cubes algorithm', *International Journal for Numerical Methods in Engineering* **58**, 189–207.

Z-set [version 8.5], http://www.zset-software.com.

Zhai, T., Jiang, X., Li, J., Garratt, M. and Bray, G. [2005], 'The grain boundary geometry for optimum resistance to growth of short fatigue cracks in high strength al-alloys', *International Journal of Fatigue* **27**, 1202–1209.

Zhai, T., Wilkinson, A. and Martin, J. [2000], 'A crystallographic mechanism for fatigue crack propagation through grain boundaries', *Acta Metallurgica* **48**, 4917–4927.

SIMULATION DE LA PROPAGATION DE FISSURE DE FATIGUE EN UTILISANT UNE MICROSTRUCTURE REELLE OBTENUE PAR TOMOGRAPHIE AUX RAYONS X

RESUME : La propagation de fissure courte en fatigue dans un matériau polycristallin dépend fortement de la microstructure. Bien que des nombreuses études de caractérisation et de modélisation aient été réalisées, la prédiction du chemin et de la vitesse de propagation de ce type de fissure n'est pas encore possible aujourd'hui.

Afin de bien comprendre les mécanismes de la propagation de fissure courte, une caractérisation in-situ d'un échantillon par la tomographie aux rayons X a été réalisée à l'ESRF. Deux techniques de caractérisation ont été utilisées. La tomographie par Contraste de Diffraction (DCT) qui est une méthode non destructive permettant de caractériser en 3D la morphologie et l'orientation des grains constitutifs de la microstructure, à l'état non-déformé. La tomographie par Contraste de Phase (PCT) permet d'obtenir la forme de fissure à divers étapes de la vie de l'éprouvette. Grâce à ces informations, il est possible de simuler la propagation de fissure en utilisant un maillage réaliste reconstruit à partir des images tomographiques.

Dans ce travail, une étude de l'anisotropie de comportement élastique est effectuée dans un 3D réel maillage microstructural. Cette étude permet de comparer les tenseurs de déformation élastique moyennés à chaque grain avec les mesures expérimentale. Ensuite, une nouvelle méthodologie est proposée pour simuler la propagation de fissure. Issue d'une simulation en plasticité cristalline, la direction de la propagation de fissure est déterminée par un post-traitement. Puis, la fissure est propagée par remaillage à une distance imposée. Cette méthode est appliquée d'abord aux monocristaux et bicristaux. La vitesse de propagation est également analysée. L'ensemble de la démarche est enfin appliqué au polycristal imagé par tomographie. En comparant les résultats de simulation avec les mesures expérimentales, le critère de la propagation de fissure est discuté.

Mots clés : plasticité cristalline, simulation par éléments finis, microstructures réelles et synthétiques en 3D, propagation numérique de fissure, tomographie, polycristal

NUMERICAL SIMULATION OF FATIGUE CRACK PROPAGATION IN REAL POLYCRYSTALS IMAGED BY X RAY TOMOGRAPHY

ABSTRACT : The short fatigue crack propagation in polycrystal materials depends strongly on microstructure. Although numerous studies of characterisation and of simulation, the prediction of the short fatigue crack propagation remains a challenge.

In order to understand the mechanisms of short fatigue crack propagation, an in-situ characterisation by X-ray tomography was carried out at ESRF, using two techniques of tomography. Diffraction Contrast Tomography (DCT) that is a non-destructive method can be used to obtain 3D morphology and grain orientations in an undeformed state of polycrystal materials. Couple with Phase Contrast Tomography (PCT), it allows to characterise the short fatigue crack propagation at different loading stages. Access to this information, it is possible to simulate the short fatigue crack propagation using a 3D reel microstructural mesh reconstructed from the tomographic images.

In this work, the elastic anisotropic behaviour in a 3D microstructural mesh is performed. The elastic strain tensors averaged in grains are also compared to the experimental measurements. Then, a new numerical approach is proposed to simulate crack propagation. From a crystal plasticity FE simulation, the crack growth direction is determined by a post processing. Next, the crack is propagated through remeshing to a selected distance. This approach is firstly applied to the single crystals and bi-crystals. The crack growth rate is also analysed. Finally, this approach is applied to the polycrystal mesh reconstructed from the tomographic images. By comparing between simulation and experimental crack, the damage indicator is discussed at the end.

Keywords : crystal plasticity, finit elements simulation, 3D real and synthetic microstructure, numerical crack propagation, tomography, polycrystal

MINES
ParisTech

ParisTech
INSTITUT DES SCIENCES ET TECHNOLOGIES
PARIS INSTITUTE OF TECHNOLOGY